Durham E-Theses

Quantum mechanics of Van der Waals complexes: rare gas-hydrocarbon systems

Thornley, Alice E.

Quantum Mechanics of Van der Waals Complexes: Rare Gas–Hydrocarbon Systems

Alice E. Thornley

Ph.D Thesis

Chemistry Department

University of Durham

October 1994

Abstract of Ph.D Thesis
" Quantum Mechanics of Van der Waals Complexes: Rare Gas-Hydrocarbon Systems"
Alice E. Thornley, Durham University, October 1994

The coupled channel approach has been used to study the Van der Waals complexes $Ar-C_2H_2$, $Ar-CH_4$ and $Ar-C_2H_4$. The $Ar-C_2H_2$ study employs a pairwise additive, atom-atom potential energy surface first without, and then with, angular anisotropy in some of the carbon atom parameters. The complex is found to be a nearly free internal rotor and the correlation between the complex and the acetylene monomer energy levels is clear.

The $Ar-CH_4$ study uses two potentials. The first includes the isotropic V_0 dependence and the first angularly anisotropic V_3 term. This is then modified to give a second potential which includes a V_4 term as well. The role of these anisotropic terms in splitting the triply degenerate bending states of the complex, when the methane monomer is in the ground vibrational state, is discussed. The energy level pattern is found to be best described in terms of a hindered rotor model.

For $Ar-C_2H_4$ a pairwise additive, atom-atom potential including angular anisotropy in the carbon atom parameters is again used. The ethylene monomer in the complex is nearly free to rotate about the C-C axis but steric considerations make end-over-end rotation restricted.

A method has been implemented to extract wavefunctions from coupled channel calculations. The utility of this technique has been illustrated by providing insights into the $Ar-HF$, $He-CO_2$ and $Ar-C_2H_4$ systems via calculated spectra and direct visualisation of the wavefunctions.

Acknowledgements

To my supervisor Dr. Jeremy Hutson, for the guidance and tolerance he has offered for the past three years.

To SERC for funding, and to the Association of British Spectroscopists for a Kirkbright Bursary which part funded a trip to the States to watch some experimentalists in their natural habitat!

To the Durham theoretical chemistry group, particularly Richard, Mark and Keith for proof reading duties. More thanks to Keith for putting a roof over my head during the final weeks of anguish and for wielding a pritt stick with skill and dexterity.

Most of all to Simon, without whose support I might never have made it.

Statement

No part of this thesis has been previously submitted by me for a degree to any university. Every effort has been made to ensure that all work which is not original to the author has been properly credited. I place no restriction upon access to, or copying of, this thesis.

Contents

Chapter 1: INTRODUCTION

1.1 HISTORY

In the 1960's when Van der Waals complexes were first observed they were recognised as valuable systems on which to test our comprehension of weak intermolecular interactions. Their non-rigid structures have much in common with reactive transition states and understanding them can help explain the dynamics of non-rigid systems. A thorough grasp of weak forces is critical for biological systems where small effects may radically alter the way molecules interact. Study of increasingly large clusters of molecules bound by Van der Waals forces will hopefully provide information on the transition from gaseous to denser phases.

In this field the limits of both theoretical and experimental knowledge are constantly being stretched and a close interaction between the two has evolved. The goal is to understand weak intermolecular interactions so well that theoretical prediction to within experimental uncertainty is possible. This goal is far from being attained, but this thesis contains another contribution towards that end.

1.2 EXPERIMENT

There are many excellent review articles and books covering the experimental field. In particular reviews by Nesbitt[2] and Hutson[3] and books edited by Bernstein[4] and Scoles[5] have been invaluable in the preparation of this overview.

The earliest experimental studies were those of bulk gas properties such as second virial coefficients and transport properties. These yield some information on one-dimensional intermolecular potential functions but no detail of the angular anisotropy of the potential is forthcoming. Since then the majority of information has come from scattering and spectroscopic studies using both bulk and molecular beam experiments.

1.2.1 Bulk Techniques

Bulk gas methods for Van der Waals complexes are currently most useful in spectroscopic studies. Experiments are performed in an equilibrium gas cell, often using direct absorption spectroscopic techniques. The populations of Van der Waals complexes are low, but can be increased by decreasing the temperature down to a lower limiting temperature, below which the monomers freeze out.

Increasing the pressure also increases the population though at the expense of spectral resolution through pressure broadening. In comparison to molecular beam conditions the temperature in a equilibrium gas cell is high and many ro-vibrational levels of the complex are populated leading to a congested spectrum. However, because the gas is at equilibrium, statistical thermodynamics can be used to relate micro- and macroscopic properties, and multiply excited states can be observed that may be unpopulated in molecular beam experiments.

1.2.2 Molecular Beams

A supersonic molecular beam is formed when a gas is expanded into a vacuum through a hole that is large compared to the mean free path of the gas. The expansion is adiabatic and all the random thermal energy of the molecules is converted into translation in a single direction. This leads to an essentially collision free environment downstream from the nozzle with a correspondingly low effective temperature.

Molecular beams allow extremely efficient complex formation and the spectra are simplified by low rotational and vibrational temperatures. Relatively few states are accessible and each will thus be more populated, increasing the signal. The reduced number of collisions minimises pressure broadening and the small spread of velocities of the molecules in the beam reduces Doppler broadening.

1.2.3 Scattering

Scattering experiments in bulk gas systems can only provide information on anisotropic potentials from properties that are dependent on the rates of inelastic collisions such as sound absorption and rotational line broadening. State-to-state relaxation rates can sometimes be measured directly, primarily between different vibrational states.

Elastic scattering experiments involving molecular beams measure either differential cross sections (DCS) or integral cross sections (ICS) as functions of scattering angle and velocity of scattered molecule respectively. A DCS is defined as the number of molecules, per interval time, scattered into an element of solid angle, divided by the incident beam flux. The ICS is the integral of the DCS over the complete solid angle. Details on the long range attractive part of the intermolecular potential may be obtained from average ICS and small angle DCS data. In the potential well information may be drawn from the rainbow

oscillations observed in the DCS and the glory effect in the ICS. Large angle DCS or high velocity ICS provide information on the repulsive wall.

Anisotropy in the potential energy surface may be observed as damping of interference structure, that is, of rainbow, glory and diffraction oscillations. The simplest experiments are beam/gas measurements where one beam is directed into a gas cell and on leaving the cell any unscattered molecules are detected giving ICS data. Experiments to determine DCS must be much more technologically advanced as the detector must be rotated through the different possible scattering angles.

Crossed molecular beam experiments can potentially provide much more information, particularly from inelastic and oriented molecule scattering which can give a detailed picture of the anisotropy of an atom-molecule potential energy surface especially in the repulsive region. The most informative, albeit difficult to perform, experiments use state-to-state techniques where the initial and final states of the system are entirely characterised. The initial state is prepared by, for example, laser excitation and the final state is characterised with a technique such as laser induced fluorescence. However, molecular beam scattering experiments are at their best for collisions involving at least one very light partner and heavier systems are harder to work with.

1.2.4 Spectroscopy

In the last 15 years, high resolution spectroscopy has emerged as a very powerful tool in studying Van der Waals systems, helped principally by technological advances such as the advent of tunable lasers. Nesbitt[2] has neatly divided the available techniques into those that measure the influence of light on molecules and those that measure the influence of molecules on the light. Methods that fall into the former category include laser induced fluorescence (LIF), photoacoustic methods, molecular beam electric resonance (MBER) spectroscopy and optothermal techniques. The second category, methods that measure the influence of molecules on the light, covers direct absorption, intracavity laser resonance and fourier transform spectroscopy.

Spectroscopic techniques are at their best studying heavier systems which are more strongly bound, but the signal intensity that can be achieved is low because the number density of complexes is small. In molecular beam experiments the number density of complexes decreases downstream from the orifice and the small beam size means short path lengths requiring very sensitive detection methods.

Chapter 1: Introduction

The short path length is also problematical to the direct absorption approach and use of a "slit" nozzle rather than a pinhole expansion source greatly improves sensitivity.

The infrared (IR) region has been widely studied as there are many suitable laser sources and monomer vibration-Van der Waals vibration combination bands appear as structure around the monomer transition frequency. Study of such combination bands yields information on the potential energy surface away from the equilibrium geometry. Bulk gas spectra tend to be very congested, lower resolution than molecular beam spectra and consequently difficult to assign. However low-temperature equilibrium gas cells do allow long absorption path lengths and the use of Fourier transform interferometers. Bulk gas techniques are thus particularly useful in inaccessible regions of the spectrum, with weakly absorbing species and when looking at the effects of increasing temperature.

Beam techniques in the IR region fall into two major categories. The "optothermal" technique originally developed by Scoles and co-workers[6] uses a bolometer to detect changes in the thermal energy content of the beam when irradiated. This method works best when used with relatively high power lasers. The other category is direct absorption laser spectroscopy where it is the power of the laser crossing the molecular beam which is monitored. For this method it is fluctuations in laser amplitude rather than the power of the laser that limits resolution, so a wide range of lasers are suitable.

Raman techniques are not as well developed as the intensities involved tend to be weak and are difficult to detect in such a low concentration system.

Microwave techniques are also extensively used, to study rotational transitions, and, as well as rotational constants, can provide dipole moments and nuclear quadrupole coupling constants, giving average values for angles in the ground state. Two techniques dominate microwave spectroscopy of Van der Waals complexes. MBER spectroscopy, pioneered by Klemperer and co-workers,[7] utilises the Stark effect to focus molecules in a given rotational state onto a detector. When the beam is irradiated, molecules excited into a new rotational state will no longer be focussed, and the flux of molecules detected will change. Fourier transform (FT) microwave spectroscopy uses a pulsed molecular beam in a Fabry-Perot cavity where the molecules are irradiated by pulses of microwave radiation and the subsequent microwave emission from excited complexes is detected. The reader is referred to a review by Legon[8] for further details of the FT microwave approach.

Chapter 1: Introduction

Frequencies in the far IR region are of the correct magnitude to excite Van der Waals vibrational modes in the ground vibrational states of the monomers, but, the far IR region is a difficult part of the spectrum for experimental study because of the lack of tunable high-resolution sources. Early attempts using a fixed frequency laser utilised the Stark effect to tune the transitions of a complex into resonance. More recently tunable sources have been developed by combining (for example) a CO_2 far-infrared laser and a microwave source allowing direct absorption studies.

LIF is used in the UV/visible region to excite frequencies around an allowed electronic transition of the monomer. If the molecules absorb they will spontaneously fluoresce provided the fluorescence lifetime is shorter than the lifetimes associated with radiationless decay. Both excitation and fluorescence frequencies may be monitored yielding information on the rovibrational state of the complex before and after excitation.

1.2.5 Systems

As experimental equipment develops the spectroscopist is increasingly restricted not by what can be measured, but by what it is possible to assign afterwards. Early work on clusters concentrated on systems such as rare gas(Rg)-H_2, Rg-Hydrogen Halide (HX) or H_2 dimer. Since then dimers and polymers of many more systems have been probed, e.g. $(N_2O)_n$ and $(C_2H_2)_n$, and rare gas atoms have been complexed with a wide variety of small molecules e.g. Ar-CH_4, Ar-C_2H_2. Larger systems have been studied but most work has concentrated on the dynamics of such complexes and minimum energy structure information as developing detailed potential energy surfaces is currently impractical with such large clusters.

1.3 THEORY

Particularly useful references for the theory of Van der Waals systems described in this section are reviews by Buckingham et al.[9] and Hobza and Zahradnik[10] and the book by Rigby et al.[11]

The crux of understanding Van der Waals systems is developing potential energy surfaces that describe them completely. From a potential energy surface for a given complex properties may be calculated that characterise the internal motions, how the complex will interact with external influences, such as electromagnetic radiation, and when and how it is likely to dissociate. The problem is

Chapter 1: Introduction

approachable from many points between two extremes. Ab Initio theory starts from the fundamental view of the system as a collection of nuclei and electrons. Solution of the electronic Schrödinger equation for such a system provides the potential energy at a particular geometry. The results of such calculations at many geometries are usually fitted to a functional form to provide a potential energy surface (PES). Empirical methods, by contrast, take some mathematical form for a potential with adjustable parameters and fit those parameters using experimental data until a satisfactory agreement with experiment is achieved. Intermediate methods involve either adjusting parameters obtained from approximate ab initio calculations or assuming the transferability of empirically derived parameters between systems.

When trying to understand the origin of intermolecular forces it is useful to divide the intermolecular PES into the contributing short-range, electrostatic, induction and dispersion terms,

$$V^{int} = V^{short} + V^{elec} + V^{ind} + V^{disp}. \tag{1.1}$$

As the distance between the monomers of the Van der Waals complex decreases, the electron clouds will overlap and repel one another giving rise to the short-range term. Charges or multipole moments arising from non-spherical charge distribution on the monomers will interact and give rise to an electrostatic force. Multipole moments on one monomer may induce moments on the other monomer leading to an induction term. The motions of electrons in one monomer will be affected by motions of electrons in the other monomer leading to a dispersion contribution.

1.3.1 Ab Initio

An Initio theory for Van der Waals molecules commonly employs a supermolecule approach, where calculations are performed for individual monomers and for the complex in different geometries. The difference between the results gives the interaction energy. The floppy nature of Van der Waals systems requires the investigation of a large number of geometries, increasing the complexity of the calculation compared to a strongly bound system. Calculations at the SCF level alone are inadequate for most purposes because they contain no electron correlation effects. The dispersion energy, which is often very important in Van der Waals complexes, especially those with no charge and small multipole moments, is purely a correlation effect.

It is possible to include correlation effects using coupled cluster methods such as the correlated electron pair approach (CEPA), or by many body perturbation theory. However, a major problem with supermolecule calculations is basis set superposition error (BSSE) which arises because the basis set for the complex is the combination of both monomer bases. The larger basis set allows greater stabilisation in the complex than in the monomers, giving an inconsistency. The effect is a mathematical, rather than a physical, phenomenon. BSSE can be corrected by the counterpoise method of Boys and Bernardi where the full dimer basis is used for all calculations, but the validity of the results is dubious and is still under active debate in ab initio circles. In the future, increasing computer power will enable basis set sizes to expand and the effects of BSSE will correspondingly decrease.

The alternative to the supermolecule approach is a perturbation theory method where the perturbation is the effect of the intermolecular interaction on the monomers. Such methods avoid the quagmire of BSSE and recent developments such as symmetry adapted perturbation theory (SAPT)[12] look promising. A recent review[13] makes a detailed comparison of state of the art supermolecule and perturbative methods.

1.3.2 Semi-Empirical Methods

For interactions of larger molecules full ab initio calculations are not possible and often the potential is broken down into parts. A first level of approximation is the SCF + damped dispersion approach where an ab initio calculation provides the majority of the potential and a dispersion function is added in once the ab initio results have been fit to a functional form. Other approaches break the potential down further and have short range terms with some sort of exponential wall form, electrostatics modelled using a central multipole expansion from experimental data and usually neglect induction. Dispersion terms are modelled using damped dispersion models, coefficients for which must be obtained from experiment, perturbation theory or combination rules. Improvements in how the V^{elec} and V^{ind} terms are described come from the distributed multipole model of Stone where the charge distribution in each molecule is described not by central multipoles but by several sets of multipoles distributed over the molecule, commonly at nuclei. Distributed polarizability analysis has also been developed to calculate the response to those multipoles, although this is particularly tricky as the induction effect is non-local, with charge flow throughout the molecule being important.

1.3.3 Empirical

Empirical methods usually choose a parametrised functional form for the potential, partitioned as before to reflect the physical nature of the system. A non-linear least squares fit is then carried out to the experimental data to determine the potential parameters. Accurate theoretical methods are required to calculate spectroscopic constants from the trial potential, and such methods are discussed in detail later in this introduction. It is important to have the right degree of flexibility in the functional form so all the experimental data can be fit but the potential is uniquely defined. Theoretical constraints are useful to keep values for fitted parameters physically reasonable and extreme range behaviour correct. Spectroscopic calculations are computationally cheap compared to scattering calculations and so a least squares fit is possible for small systems, e.g. atom-linear molecule complexes. Least squares fitting also provides estimates of parameter uncertainty and correlation between parameters. By contrast scattering calculations are expensive and a manual "best guess" adjustment is required to fit scattering data. An alternative method developed by Nesbitt *et al.*[14] for atom-diatom systems is based on Rydberg-Klein-Rees (RKR) analysis of rotational levels to give 1D curves for each bending vibrational state. These curves are then inverted to give a 2D potential.

1.4 CO-ORDINATE SYSTEMS

Many co-ordinate systems may be used to describe a Van der Waals complex formed between an atom and a molecule. This thesis uses an extension of the conventional Jacobi atom-diatom co-ordinates. The vector from the centre of mass of the molecule to the atom is denoted $\mathbf{R}$ with length R and corresponding unit vector $\hat{\mathbf{R}}$. The Euler angles $(\alpha_R, \beta_R, 0)$ are used to describe the orientation of $\hat{\mathbf{R}}$ with respect to the space-fixed axis system. These then define the body-fixed axis system of the complex, X_R, Y_R, Z_R. Monomer body-fixed axes x, y, z are chosen, usually with reference to the symmetry of the system, and three more Euler angles (θ, ϕ, χ) describe the relationship of x, y, z to X_R, Y_R, Z_R.

This is illustrated below for the argon-ethene complex.

1.5 THE COUPLED EQUATIONS

The form of the coupled equations for atom-molecule systems has been developed by extension from atom-diatom systems. There are numerous sources for

Chapter 1: Introduction
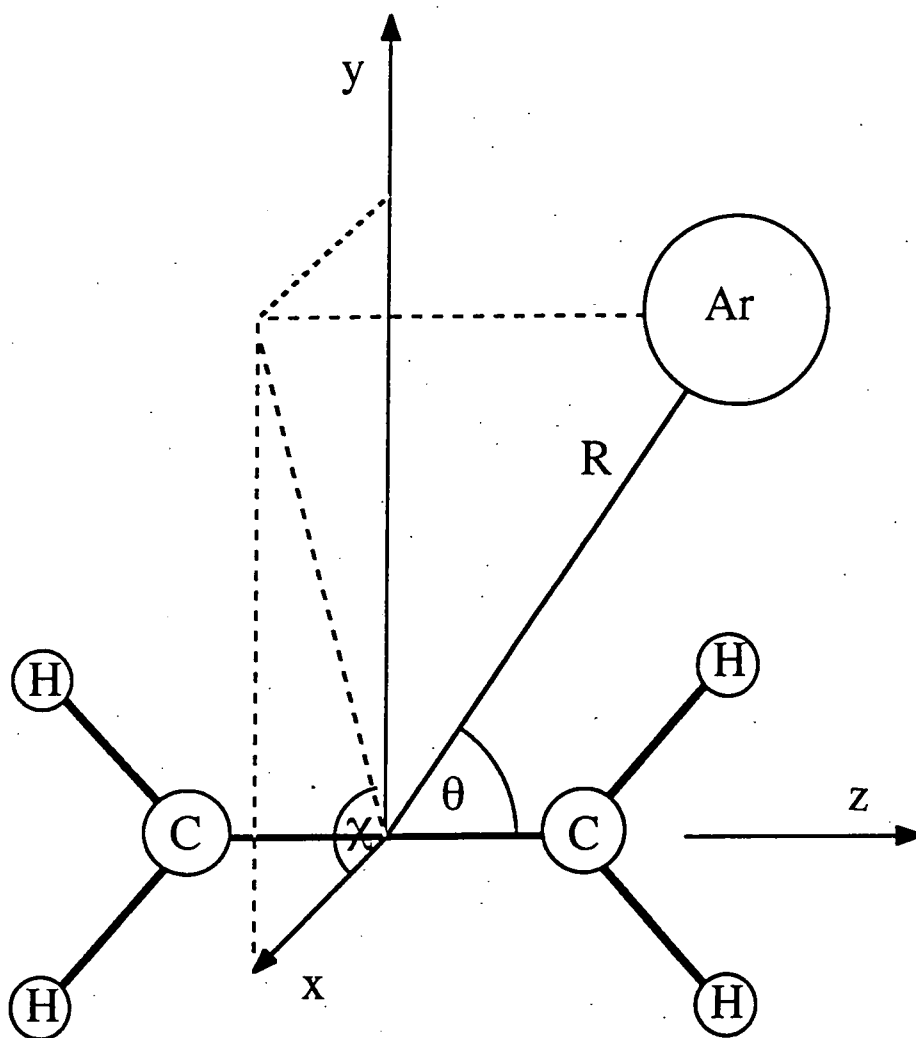
Fig. 1.i Co-ordinate System for Argon-Ethene.

the following section but papers by Hutson and co-workers,[15–18] Kroto's book [19] and a paper by Green[20] were found to be particularly useful.

Within the Born-Oppenheimer approximation the Hamiltonian for an atom–molecule complex is

$$H = -\frac{\hbar^2}{2\mu}R^{-1}\left(\frac{\partial^2}{\partial R^2}\right)R + \frac{\hbar^2 \hat{L}^2}{2\mu R^2} + V(R,\theta,\chi) + H_{\mathrm{mon}}, \qquad (1.2)$$

where the reduced mass μ is $m_A m_{\mathrm{mon}}/(m_A + m_{\mathrm{mon}})$,

$$\hat{L}^2 = -\frac{1}{\sin^2\beta}\left\{\sin\beta\frac{\partial}{\partial\beta}\left(\sin\beta\frac{\partial}{\partial\beta}\right) + \frac{\partial^2}{\partial\alpha^2}\right\}, \qquad (1.3)$$

Chapter 1: Introduction

is the (dimensionless) angular momentum operator for end-over-end rotation of the complex as a whole, and H_{mon} is the Hamiltonian for the isolated monomer. For all the systems studied in this thesis the molecule is taken to be a rigid rotor in a given vibrational state, usually the ground state. H_{mon} will thus be the rotational Hamiltonian for the system in question. For monomers in non-degenerate vibrational states, the explicit dependence of the potential and the wavefunctions on the monomer vibrational coordinates may usually be neglected except in calculations of vibrational predissociation or vibrationally inelastic collisions (though it is straightforward to include if necessary). The situation for degenerate vibrational states is a little more complicated, as in chapter 3, and will be dealt with where it arises.

Due to the weak nature of the Van der Waals interaction the atom can be regarded as perturbation on the state of the molecule. The use of the monomer vibration-rotation functions as a basis set for describing the system is thus a logical choice and such an expansion leads to a set of differential equations coupled in **R** which are known as the coupled equations.

Calculations of the energy levels may be carried out in either space-fixed or body-fixed basis sets. The two formulations give exactly the same results if all channels arising from each monomer level are included. For close-coupling calculations, that is, with no approximation to the coupled equations, including all channels, the space-fixed representation is usually more convenient, because the coupling matrices are simpler to construct. However, space-fixed and body-fixed calculations offer different possibilities for approximations based on perturbation theory. For most Van der Waals complexes, the anisotropy is strong enough for the monomer angular momentum to be quantised along the **R** vector, and a body-fixed quantisation scheme is most appropriate. For complexes with very small anisotropies and small reduced masses, such as those containing He or H_2, a space-fixed quantisation scheme is appropriate. This may also be true for complexes with a heavy monomer in high angular momentum states. Both representations will therefore be described in the following sections.

The vibrationally averaged intermolecular potential $V(R, \theta, \chi)$ for an atom non-linear molecule system is conventionally expanded in renormalised spherical harmonics $C_{\lambda\mu}(\theta, \chi)$[21]

$$V(R, \theta, \chi) = \sum_{\lambda, \mu} V_{\lambda, \mu}(R) C_{\lambda\mu}(\theta, \chi).$$

(1.4)

Chapter 1: Introduction

This expansion is completely general provided enough terms are included in the potential expansion, the major advantage being the simplification in evaluation of potential matrix elements between angular momentum eigenfunctions.

1.5.1 Space-fixed Representation

In the space-fixed representation, the total wavefunction of a state α is expanded in space-fixed functions which are eigenfunctions of the total angular momentum $\hat{J}^2$, the end-over-end angular momentum operator $\hat{L}^2$ and the monomer Hamiltonian H_{mon},

$$\chi_\alpha^{JM} = R^{-1} \sum_{j\tau L} \Phi_{j\tau L}^{JM}(\alpha_R, \beta_R, \alpha_r, \beta_r, \gamma_r) \psi_{j\tau L}^{J\alpha}(R). \tag{1.5}$$

Where the functions $\Phi_{j\tau L}^{JM}(\alpha_R, \beta_R, \alpha_r, \beta_r, \gamma_r)$ are

$$\Phi_{j\tau L}^{JM}(\alpha_R, \beta_R, \alpha_r, \beta_r, \gamma_r) = \sum_{m_j m_L} \langle jLm_j m_L | JM \rangle Y_{Lm_L}(\beta_R, \alpha_R) \phi_{m_j\tau}^j(\alpha_r, \beta_r, \gamma_r). \tag{1.6}$$

These functions form a complete orthonormal set spanning the space of the angular coordinates. The Euler angles α_r, β_r and γ_r specify the orientation of the monomer in the *space-fixed* coordinate system, and $\langle jLm_j m_L | JM \rangle$ is a Clebsch-Gordan coefficient. $\phi_{m_j\tau}^j$ is a monomer rotational function with angular momentum j and projection m_j along the *space-fixed* Z axis. The precise form of the $\phi_{m_j\tau}^j$ varies from problem to problem:

- For an atom-diatom complex, the τ label is not needed and $\phi_{m_j k}^j = Y_{jm_j}(\alpha_r, \beta_r)$, a spherical harmonic in the space-fixed axis system.

- For an atom–symmetric top complex, τ is k, the projection of the monomer angular momentum onto its own principal axis, and $\phi_{m_j k}^j$ a normalised rotation matrix, $\phi_{m_j k}^j = [(2j+1)/8\pi^2]^{\frac{1}{2}} D_{m_j k}^{j*}(\alpha_r, \beta_r, \gamma_r)$.

- For an atom–asymmetric top complex, τ is an index that labels the monomer levels for each j in order of increasing energy, and $\phi_{m_j\tau}^j$ is a linear combination of normalised rotation matrices that is an eigenfunction of the monomer rotational Hamiltonian.

Chapter 1: Introduction

- For an atom–spherical top complex, $\phi^j_{m_j\tau}$ is again a linear combination of normalised rotation matrices that is an eigenfunction of the monomer rotational Hamiltonian. In this case, τ includes information about the symmetry of the monomer rotational state (A, E or F).

When the atom–asymmetric top representation of the wavefunction is substituted into the total Schrödinger equation of the complex, using the Hamiltonian of Eq. (1.2), the equation obtained is,

$$\left[-\frac{\hbar^2}{2\mu}\frac{d^2}{dR^2} + (j\tau LJ|V(R,\theta,\chi)|j\tau LJ) + \frac{\hbar^2 L(L+1)}{2\mu R^2} + E^{\mathrm{mon}}_{j\tau} - E\right]\psi^{J\alpha}_{j\tau L}(R)$$

$$= -\sideset{}{'}\sum_{j'\tau'L'}(j\tau LJ|V(R,\theta,\chi)|j'\tau'L'J)\psi^{J\alpha}_{j'\tau'L'}(R),$$

$$\tag{1.7}$$

where $E^{\mathrm{mon}}_{j\tau}$ are the monomer energy levels, the prime on the sum indicates summation over all $j'\tau'L' \neq j\tau L$, and the round brackets indicate integration over all coordinates except $\mathbf{R}$. The matrix elements of the potential may be expanded in terms of matrix elements between individual rotation matrices,

$$(jkLJ|V(R,\theta,\chi)|j'k'L'J) = \sum_{\lambda\mu}V_{\lambda\mu}(R)f_{\lambda\mu}(jkL;j'k'L';J), \tag{1.8}$$

where from the Wigner-Eckart theorem

$$f_{\lambda\mu}(jkL;j'k'L';J) \equiv (jkLJ|C_{\lambda\mu}(\theta,\chi)|j'k'L'J)$$

$$= (-)^{L+L'+J-k}\left[(2j+1)(2j'+1)(2L+1)(2L'+1)\right]^{\frac{1}{2}} \tag{1.9}$$

$$\times\begin{pmatrix} L & \lambda & L' \\ 0 & 0 & 0 \end{pmatrix}\begin{pmatrix} j & \lambda & j' \\ k & \mu & -k' \end{pmatrix}\begin{Bmatrix} L & \lambda & L' \\ j' & J & j \end{Bmatrix}$$

and $\begin{Bmatrix} \cdot & \cdot & \cdot \\ \cdot & \cdot & \cdot \end{Bmatrix}$ is a Wigner 6-j symbol.[21]

In this representation J and parity $p' = (-)^{j+L}$ are rigorously good quantum numbers and the intermolecular potential cannot mix states of different J or p'. The prime here is used to distinguish a slightly different definition of parity from that commonly used in spectroscopy, $p = (-)^{j+L+J}$, thus $p' = p(-1)^J$.

Chapter 1: Introduction

1.5.2 Body-fixed Representation

In the body-fixed coupling scheme, the total wavefunction of a state α is expanded in body-fixed functions,

$$\chi_\alpha^{JM} = R^{-1} \sum_{j\tau K} \Phi_{j\tau K}^{JM}(\alpha_R, \beta_R, \phi, \theta, \chi) \psi_{j\tau K}^{J\alpha}(R), \qquad (1.10)$$

where the functions $\Phi_{j\tau K}^{JM}(\alpha_R, \beta_R, \phi, \theta, \chi)$ are eigenfunctions of the body-fixed angular momentum operator $\hat{J}_{Z_R}$ with eigenvalue K,

$$\Phi_{j\tau K}^{JM}(\alpha_R, \beta_R, \phi, \theta, \chi) = \left(\frac{2J+1}{4\pi}\right)^{\frac{1}{2}} \mathcal{D}_{MK}^{J*}(\alpha_R, \beta_R, 0)\phi_{K\tau}^{j}(\phi, \theta, \chi). \qquad (1.11)$$

The function $\mathcal{D}_{MK}^{J}(\alpha, \beta, \gamma)$ is a rotation matrix element with the phase convention of Brink and Satchler[22] and $\phi_{K\tau}^{j}(\phi, \theta, \chi)$ is a monomer rotational function with angular momentum j and projection K along the intermolecular axis. The precise form of the $\phi_{K\tau}^{j}$ parallels the space-fixed $\phi_{m_j\tau}^{j}$. Substitution of the functions (1.11) into the total Schrödinger equation yields a set of coupled equations of the form

$$\begin{aligned}
\Bigg[-\frac{\hbar^2}{2\mu}\frac{d^2}{dR^2} &+ (j\tau K J|V|j\tau K J) + \frac{\hbar^2}{2\mu R^2}(j\tau K J|(\hat{J}-\hat{\jmath})^2|j\tau K J) \\
&+ E_{j\tau}^{\mathrm{mon}} - E \Bigg]\psi_{j\tau K}^{J\alpha}(R) \\
&= -{\sum_{j'\tau'}}'(j\tau K J|V|j'\tau'K J)\psi_{j'\tau'K}^{J\alpha}(R) \\
&\quad - {\sum_{K'=K\pm 1}}' \frac{\hbar^2}{2\mu R^2}(j\tau K J|(\hat{J}-\hat{\jmath})^2|j\tau K'J)\psi_{j\tau K'}^{J\alpha}(R),
\end{aligned} \qquad (1.12)$$

where $E_{j\tau}^{\mathrm{mon}}$ is the energy of a monomer in state $j\tau$, and the operator $\hat{L}^2$ has been replaced by its body-fixed equivalent, which may be written loosely as $(\hat{J}-\hat{\jmath})^2$. The round bracket notation $(\ |\ |\ )$ indicates integration over all variables except R, and the symbol $\sum'$ indicates a summation that excludes the diagonal term $(j'\tau'K' = j\tau K)$. Eqs. (1.12) are a set of differential equations, one for each *channel* $j\tau K$ included in the basis set. All terms off-diagonal in $j\tau K$, which couple the different equations, have been taken to the right hand side.

For complexes of symmetric tops, the potential matrix elements in the body-fixed representation are[20]

$$(jkKJ|V|j'k'KJ) = \sum_\lambda g_{\lambda\mu}(jkj'k'K)V_{\lambda\mu}(R), \qquad (1.13)$$

Chapter 1: Introduction

where

$$g_{\lambda\mu}(jkj'k'K) = (-)^{K-k}[(2j+1)(2j'+1)]^{\frac{1}{2}} \begin{pmatrix} j & \lambda & j' \\ -k & \mu & k' \end{pmatrix} \begin{pmatrix} j & \lambda & j' \\ -K & 0 & K \end{pmatrix}$$

(1.14)

and $\begin{pmatrix} \cdot & \cdot & \cdot \\ \cdot & \cdot & \cdot \end{pmatrix}$ is a Wigner 3-j symbol.[22] For complexes of asymmetric or spherical tops, where the monomer functions are linear combinations of normalised rotation matrices, the potential matrix elements may be expanded in terms of these integrals, with sums over k and k'. In any case, the potential matrix elements in the body-fixed representation are diagonal in J and K and independent of J.

The matrix elements of the operator $\hat{L}^2 = (\hat{J} - \hat{j})^2$ are

$$\langle j\tau KJ|(\hat{J} - \hat{j})^2|j\tau KJ\rangle = J(J+1) + j(j+1) - 2K^2,$$

(1.15)

$$\langle j\tau KJ|(\hat{J}-\hat{j})^2|j\tau K\pm1J\rangle = -[J(J+1)-K(K\pm1)]^{\frac{1}{2}}[j(j+1)-K(K\pm1)]^{\frac{1}{2}},$$

(1.16)

with all other matrix elements zero.

The basis functions of equation (1.11) do not have definite parity except for $K = 0$. However, since parity is known to be a rigorous quantum number it is customary to define linear combinations of these functions that do have definite parity. These combinations are known as the parity adapted basis set. J is also a rigorously good quantum number in the body-fixed representation and K is nearly so.

The coupled equations (1.12) provide the exact formulation of the body-fixed problem. However, the body-fixed formulation is most useful because of the possibilities it offers for approximation. In particular, the *helicity decoupling* approximation is obtained when the off-diagonal Coriolis matrix elements of Eq. (1.16) are neglected, so that the coupled equations become diagonal in K. For high J, the helicity decoupling approximation drastically reduces the number of basis functions N that are coupled to one another. Since the time taken to solve the coupled equations is proportional to N^3, this results in a very considerable saving in computer time. Helicity decoupling is a good approximation provided the Coriolis matrix elements, which are of magnitude BjJ, are small compared to the separation between states of different K, which is determined by the potential anisotropy. The approximation is thus useful for low angular momentum states of most Van der Waals complexes (with the exception of the He and H_2 systems mentioned above).

Chapter 1: Introduction

1.5.3 Angular Momentum Coupling Cases.

Depending on the anisotropy of the potential surface and the nature of the monomers it can be envisaged that an atom-molecule complex may vary in nature between a free internal rotor with the atom causing negligible perturbation to the molecule energy levels, to a rigid complex with a completely different set of energy levels to the monomer. This can be rationalised by considering the several ways in which the angular momenta may coupled together and was pointed out by Bratoz and Martin.[22]

The relative magnitudes of B, the rotational constant of the complex, b, that of the molecule, and V_{aniso} the dominant anisotropic term of the potential, lead to three major coupling schemes. These have been denoted cases 1, 2 and 3 [15] in order of increasing anisotropy.

1.5.4 Case 1

In this case, where $V_{\text{aniso}} \ll B, b$, the space-fixed representation is appropriate. Both j and L are nearly good quantum numbers and couple to form J. Pure case 1 coupling requires zero anisotropy. Case 1 coupling complexes show groups of energy levels with the same j and L split into components of different J from $| j - L |$ to $j + L$.

1.5.5 Case 2

This case occurs when the anisotropic potential terms are large compared to the L splitting for a particular j,J, but small compared to the splitting for levels of different j. It is found that j is nearly a good quantum number and has a well defined projection onto the intermolecular axis $\mathbf{R}$, K. The end-over end rotation of the complex couples with K to give J. In this case a body-fixed representation is appropriate. The complexes show groups of levels with $K = 0, \pm1, \pm2, \cdots \pm j$. Within each (j, K) group J can take any value $J \geq | K |$. For real Van der Waals molecules it is necessary to consider Coriolis terms which connect states of the same J,j and parity, with $| K |$ differing by ±1.

Case 2 coupling will break down either as the Coriolis matrix elements increase with increasing J and j or if the anisotropy is high enough to cause significant mixing of states of different j.

Chapter 1: Introduction

1.5.6 Case 3

In this case the potential anisotropy is large compared to the rotational constant of the molecule b and thus the complex is a nearly rigid molecule bending about its equilibrium geometry. Neither j nor L is a good quantum number but K nearly is. A body-fixed basis set can often be used but a basis set of harmonic oscillator functions may be more appropriate. The limit of case 3 is the "rigid rotor" picture with the energy levels corresponding to those of an asymmetric top (or a linear rotor if the equilibrium structure is linear).

The coupling case observed will also depend on the internal state of the van der Waals molecule. The transition between cases is discussed in some detail by Hutson.[15] The importance of choosing the correct set of quantum numbers is illustrated well by the argon-acetylene van der Waals molecule, a case 2 complex showing some case 3 character, which is discussed in chapter 2.

1.6 SOLUTION OF THE COUPLED EQUATIONS

The coupled equations (1.7) and (1.12) take the general form

$$\frac{d^2\psi}{dR^2} = [\mathbf{W}(R) - \epsilon\mathbf{I}]\psi(R), \qquad (1.17)$$

where, for N coupled channels, $\mathbf{W}(R)$ is an $N \times N$ matrix, $\epsilon = 2\mu E/\hbar^2$, $\mathbf{I}$ is an $N \times N$ unit matrix, and $\psi(R)$ is a column vector with N components. These equations are exactly the same as the coupled equations of molecular scattering theory, except that the boundary conditions are different for the bound state case. For bound states, $\psi(R)$ must approach zero as $R \to 0$ and $R \to \infty$. The coupled equations may be solved by a variety of methods, including direct propagation of the differential equations[23,15] or a basis set expansion in products of angular and radial functions.[24] They can also be transformed to a pointwise representation,[25] and solved either variationally[25] or by the collocation method.[26] When the only approximation to the coupled equations is truncation of the monomer basis set used the calculation is exact, provided enough terms are carried. Such calculations are referred to as close-coupling calculations. Historically many methods were developed to approximate the coupled equations before solution. The simplest approximation is where only the diagonal matrix elements are allowed and variations on this theme are collectively labelled "distortion" methods. Other methods involve separation of angular and radial motions, the most widespread being the Born Oppenheimer Angular Radial Separation (BOARS). The helicity

decoupling method discussed earlier is another approximation. Modern computational methods remove the need for the use of these methods for small systems, for which accurate solution of the complete coupled equations is perfectly possible. However they remain useful for larger systems, for example, molecule-molecule complexes.

The following discussion is not intended to be a comprehensive guide to all the methods in use but rather an outline of the most common approaches. In this thesis, the coupled differential equations were propagated directly, using methods implemented in the general-purpose BOUND program.[27] Consequently more attention will be paid to this method in the following description than to the possible alternatives. Reviews by Hutson,[15] LeRoy and Carley[24] and Bačić and Light[25] were very helpful in the preparation of this section.

1.6.1 The Coupled Channel Approach

The coupled channel approach handles the radial co-ordinate R by direct numerical propagation on a grid, thus dispensing with the need for a basis set in this co-ordinate. For a bound-state calculation the objective is to locate energies E_n for which there exist solutions of the coupled equations (1.17) that satisfy bound-state boundary conditions. These are usually taken to be $\psi(R) \to 0$ as $R \to 0$ or ∞. The usual strategy is to take boundary conditions at some arbitrary starting points R_{min} and R_{max}, well into the short- and long-range classically forbidden regions for a trial energy E_{trial}, and to propagate to a matching point R_{mid} in the classically allowed region. If E_{trial} corresponds to an eigenvalue both the wavefunction and the derivative of the wavefunction will match up at R_{mid}. After two such energies have been tried, a root-finding algorithm such as the secant method is used to converge upon the eigenvalue.

Many algorithms have been proposed to handle the propagation. Some, such as that of Gordon[28,29] propagate the actual wavefunctions, while others propagate a function of the wavefunction.[30-32] Propagating a wavefunction in a classically forbidden region is numerically unstable, particularly if closed channels (that is those with $W_{jj}(R) > E$) are included in the calculation. In order to get converged results closed channels are indispensable and a stabilising transformation is required with methods that propagate the wavefunction directly. A more desirable route is to use a propagator that is stable in the presence of closed channels. One such commonly used propagator is the log-derivative algorithm where the

Chapter 1: Introduction

log-derivative matrix $\mathbf{Y}(R)$ defined by [30]

$$\mathbf{Y}(R) = \Psi'(R)[\Psi(R)]^{-1}, \qquad (1.18)$$

is propagated over the whole range. In equation (1.18) Ψ is a $N \times N$ wavefunction matrix which is required to describe all the possible solutions under one boundary condition (see chapter 4 for more detail), and Ψ' is the radial derivative of Ψ. The matching condition reduces to the determinant of the difference matrix between incoming and outgoing log-derivative matrices being zero.

The coupled channel method is very stable and efficient for calculating eigenvalues of the bound-state Schrödinger equation. By integrating directly in R it avoids use of a basis set in this difficult to converge co-ordinate. As a result it is the method of choice when very high precision is required.

It is possible to count the number of nodes in the wavefunction during propagation[33] thus determining the number of eigenvalues lying below E_{trial}. This node count is very valuable when trying to find all the eigenvalues in a given energy range. Expectation values may be calculated without wavefunctions using the finite difference method of Hutson[34] but until recently wavefunctions were not available from the log-derivative and similar propagators. Implementation of a method to extract wavefunctions from the log-derivative propagator is described in chapter 4 of this thesis.

The main disadvantage of the coupled channel approach is that it is necessary to converge on each eigenvalue separately. If many eigenvalues are required this may make a complete basis set method more attractive, especially if relatively low precision is acceptable.

1.6.2 Full Basis Set Expansion

In the full basis set expansion method each radial channel is expanded in terms of some complete set of basis functions $\varphi_\alpha(R)$

$$\psi_{j\tau L}^{J\alpha}(R) = \sum_n A_{\alpha\alpha'}^J \varphi_\alpha(R), \qquad (1.19)$$

which are chosed to be orthonormal for $0 \le R \le \infty$ and to satisfy the boundary conditions. Substituting (1.19) into the coupled equations, multiplying by their complex conjugate and integrating over R generates a matrix diagonalisation problem. Basis functions are chosen to have radial matrix elements that are easy

to evaluate, to minimise the number of functions required in the basis and hopefully to allow some physical interpretation of the results. Discrete eigenfunctions of a radial Schrödinger equation for a chosen isotropic potential are one example of such a basis set.[24] Whilst conceptually the simplest technique such calculations tend to be poorly convergent in the radial basis set and an often intractably large number of functions must be included to achieve high precision results.

1.6.3 Pointwise Techniques

Rather than use a basis set expansion one may instead use a pointwise representation for all or part of the Schrödinger equation. The most established method in this category is the discrete variable representation (DVR) of Light and co-workers, where the potential is replaced by a pointwise representation but a basis set is retained to define the kinetic energy term. The N-point quadrature approximation for the potential matrix leads to a set of N algebraic equations which may be solved variationally. Related techniques such as the collocation method include the kinetic term in the pointwise representation as well.

Most applications of pointwise methods use contracted radial basis sets and thus require less calculation time compared to a full basis set calculation.

1.7 WORK IN THIS THESIS

The behaviour of atom-diatom Van der Waals complexes is generally well understood and has been characterised for many different systems. Detailed theoretical study of Van der Waals systems is currently progressing in three distinct directions.

1.Atom-Molecule Systems

Study of atom-molecule systems should yield information on how the size and shape as well as the chemical nature of the molecule affects the potential anisotropy. A rare gas atom can effectively be used as a structureless probe of the molecule's potential energy surface.

2.Diatom-Diatom and Larger Systems

An increased number of degrees of freedom and the need for two monomers Hamiltonians increases the complexity of the theory required rapidly. Study of such systems is critical if the knowledge gained from Van der Waals complexes is ever to be applied in "real" situations.

Chapter 1: Introduction

3. Three Body Systems

Currently systems such as Ar_2HCl are being studied, the aim being to identify and quantify three-body interactions.

The first of these three directions was chosen at the start of the period of study with rare gas-small hydrocarbon systems chosen as the subject material as significant experimental data was available for several systems.

Chapters 2 and 3 thus present results on the Ar-acetylene and Ar-methane Van der Waals complexes. Historically, work was then started on the $Ar-C_2H_4$ complex but the energy level pattern obtained proved difficult to rationalise and wavefunctions were required to provide a physical interpretation of these levels. Consequently extraction of wavefunctions from the log-derivative propagator in the coupled channel method was investigated using Ar-HF as a test case. These results are presented in chapter 4. $He-CO_2$ is a system of interest to other members of the Durham theoretical chemistry group and provided a second test case for the calculation of wavefunctions. This work is therefore in chapter 5. In chapter 6 the two threads are drawn together in the work on $Ar-C_2H_4$.

Chapter 1: Introduction

Chapter 2: THE ARGON–ACETYLENE COMPLEX

2.1 BACKGROUND

The argon–acetylene system was first studied by radio frequency spectroscopy in 1980 by DeLeon and Muenter.[35] The complex's small electric dipole moment and experimental limitations meant that relatively few transitions were observed. A T-shaped equilibrium geometry was deduced and by assuming the inertial defect to be zero the Ar–acetylene centre-of-mass distance, R, was found to be 3.25 Å. However large-amplitude zero-point vibrations are expected leading to a large inertial defect so this value of R is questionable. DCCD–Ar data were analysed to give a quadrupole coupling constant and a value of $\cos^{-1}(\sqrt{\langle\cos^2\theta\rangle}) = 72°$, being the angle between R and the acetylene axis.

More recently Ohshima *et al.*[36] have observed microwave spectra of the complex and Hu *et al.*[37] have observed high-resolution infrared spectra associated with the monomer ν_3 (asymmetric C-H stretch) band. Takami *et al.*[38] have observed spectra associated with the monomer ν_5 bending vibration. Hu *et al.*[36] have combined both the microwave and infrared data and fitted to Watson's S-reduced asymmetric rotor Hamiltonian.[39] This allowed determination of all three rotational constants and some centrifugal distortion constants for the ground van der Waals state. The inertial defect was found to be 17.964 uÅ² and the value of R determined as 4.02 Å. This is a vibrational average and is expected to be greater than at the T-shaped configuration. The potential is found to be surprisingly isotropic with large bending amplitudes. A flat-bottomed and steep-walled angular potential is needed to agree with observations. The results presented in this chapter were published in 1992.[40] Since then significant new experimental data has become available from both spectroscopic[41,42] and scattering[43] studies and ab initio calculations have been performed to help interpret some of these results.[41,44] The work presented here will be discussed in the light of these new results at the end of the chapter.

Some work has also been done on the He–HCCH system. Danielson *et al.*[45,46] investigated total differential cross sections for various He–hydrocarbon systems in molecular beam scattering experiments. The damping of the differential cross section directly reflects the anisotropy of the hydrocarbon partner on the repulsive wall. An anisotropy trend, measured by the difference in the position of

the minimum parallel and perpendicular to the principal molecular axis, was observed; $C_2H_6 > C_2H_4 \sim C_2H_2 > CHF_3$. Van der Waals radii and bond lengths would suggest the reverse of this situation, however, the trend may be explained by considering the effect of the triple bond in acetylene which will decrease the anisotropy by raising the electron density in the centre of the molecule. An anisotropic intermolecular potential was developed for He–HCCH fit to both the differential cross section and dilute gas data.[46] Slee *et al.*[47] made predictions of the spectrum of He–HCCH based both on this empirical potential[46] and on a scaled ab initio potential that they calculated. Buck *et al.*[48] have also performed differential scattering experiments on He–HCCH, and find that their experimental results are much better produced by a spindle-shaped contour in the repulsive potential than a hard ellipsoidal shape. He–HCCH is dynamically very different to Ar–HCCH and so these calculations can be used qualitatively only to note the isotropic nature of the potential.

Since the first characterisation of the Ar–HCCH complex[35] many other Van der Waals complexes involving acetylene have been studied and a few trends are interesting to note. The structures of Van der Waals molecules involving acetylene, apart from Ar–HCCH, are mostly determined by electrostatic interactions and can be divided into two categories. In Ar–HCCH[36], HF–HCCH[49] and HCl–HCCH[50] the structure is T-shaped with the hydrogen of the hydrogen halides closest to the acetylene triple bond electron density. In NH_3–HCCH[51], CH_3CN–HCCH[52] and H_2O–HCCH[53] the adduct lies along the acetylene axis with the N or O atom approaching one of the acetylenic hydrogen atoms. Rings with dual van der Waals bonding, involving both categories, include CO_2–HCCH[54] and H_2CO–HCCH[55] . The acetylene dimer has a T-shaped planar structure, C_{2v}, thus exhibiting both of these interactions. The barrier to interconversion is low and the tunnelling motion has been studied[56,57] . Some theoretical work on such complexes has been done by Dykstra[58] as a test for the molecular mechanics of clusters method (MMC), but only basic properties, such as equilibrium structures, were determined.

Clearly complexes involving acetylene are a good starting point for systems containing simple hydrocarbons and as a first step Ar–HCCH is taken as the simplest system with a substantial amount of experimental data available.

2.2 THEORY

The standard Jacobi axis system as described in the introduction is illustrated in figure 2.i for the argon–acetylene system.
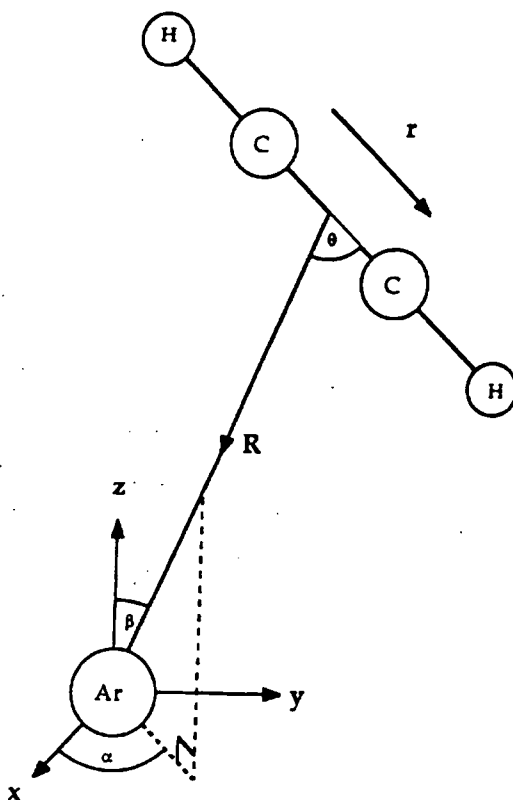
Fig. 2.i Coordinate System for Argon–Acetylene.

The atom-molecule Hamiltonian simplifies somewhat for an atom-linear molecule complex as the potential term becomes a function of 2 variables only and the monomer Hamiltonian simplifies giving:

$$H = -\frac{\hbar^2}{2\mu}R^{-1}\left(\frac{\partial^2}{\partial R^2}\right)R + \frac{\hbar^2 \hat{L}^2}{2\mu R^2} + V(R,r,\theta) + H_{\text{mon}}, \qquad (2.1)$$

where μ is the reduced mass of the system, $\hat{L}^2$ is the angular momentum operator for the end over end rotation of the system. H_{mon} is the Hamiltonian for the isolated linear molecule.

2.3 AN ATOM-ATOM POTENTIAL.

The experimental data on Ar–HCCH are limited at present and so sophisticated many-parameter models for the potential energy surface are not appropriate. As a first attempt a simple model based on atom-atom pairwise additivity was taken for the potential,

$$V = \sum_{i=1}^{2} A_C \exp(-\beta_C R_i) - \frac{C_C}{R_i^6} + \sum_{j=1}^{2} A_H \exp(-\beta_H R_j) - \frac{C_H}{R_j^6}, \qquad (2.2)$$

Chapter 2: The Argon–Acetylene Complex

where R_i denotes distance from the Ar atom to the ith atom in acetylene. The values of the parameters listed in table 2.I were taken from work done on Ar-ethylene,[59] neglecting atomic anisotropy as a first approximation.

A_C	1012	E_h
β_C	2.132	a_0^{-1}
C_C	67.1	$E_h a_0^6$
A_H	34.15	E_h
β_H	1.959	a_0^{-1}
C_H	18.6	$E_h a_0^6$

Table 2.I Parameters used for the Ar–HCCH Atom-Atom Potential

This was found to give a potential which, at the T-shaped equilibrium geometry, has a maximum well depth of -197.9 cm^{-1} at a separation $R_m = 3.63$ Å.

A plot of the variation of intermolecular separation at the potential minimum R_m with A_C, the carbon repulsive coefficient, at the T-shaped structure, is shown in figure 2.ii The triple bond in acetylene will lead to greater electron density about the carbon atoms than in ethylene, allowing an increase of the carbon repulsive coefficients to be physically plausible. With this in mind the A_C value was taken as $1200E_h$ leading to an R distance of 3.85Å, a reasonable estimate from the various experimental data. Figure 2.iii is a contour plot of this potential, which will be referred to as $A(1200)$.

The BOUND computer program[60] was used to calculate the vibration-rotation energy levels of the complex using this potential. Full close-coupling calculations were performed with angular functions expanded in a space-fixed basis set including all the monomer functions up to $j_{max} = 20$. Acetylene was treated as a rigid rotor with rotational constant $b = 1.17692$ cm^{-1}.[61] The potential was expanded in Legendre polynomials $P_\lambda(\cos\theta)$ including all terms to $\lambda_{max} = 18$. The reduced mass was taken to be 15.7574775 u . The starting points for the numerical propagation were taken as $R_{min} = 2.8$ Å and $R_{max} = 7.0$ Å using Johnson's log-derivative propagator.[30] These parameters are the same for all following calculations. Convergence with respect to $\lambda, J_{max}, R_{min}, R_{max}$ and the interval size has been checked for all potentials and was found to be better than 10^{-4} cm^{-1}.
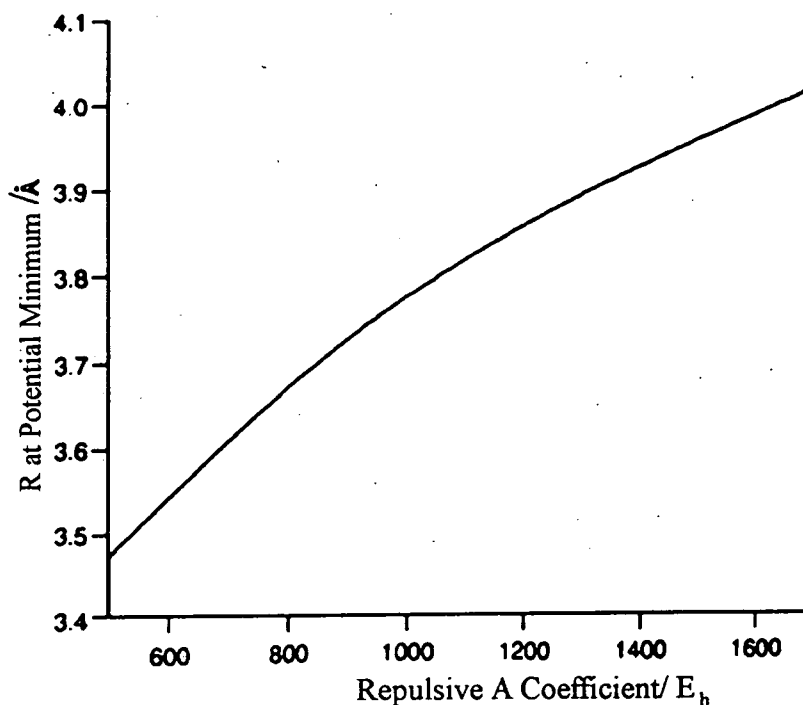
Fig. 2.ii Variation of Intermolecular Separation at the potential minimum R_m with Carbon Repulsive Coefficient.

Figures 2.iv and 2.v show the energy level pattern found. The levels in which the Van der Waals stretch is excited ($n = 1$) are shown dashed and they echo the pattern of the $n = 0$ levels, although the bending frequency is higher than for the $n = 0$ levels.

Figure 2.iv shows the near-rigid rotor grouping of the levels assuming a case 3 assignment. For a given J there are $2J + 1$ rotational states for each vibrational level which have $|K|$ from 0 to J. Figure 2.v shows the levels described by free internal rotor grouping as used for case 1 or 2. The groups correspond to a particular monomer rotational quantum number J. For a total angular momentum J there are $2 \times \min(J, j) + 1$ levels which are labelled either by l (case 1) or K (case 2).

For this potential we see that a rigid rotor picture is more appropriate for lower states but for higher bending states a free internal rotor pattern is clear.

As the BOUND program performs a full dynamical calculation, the energy levels obtained include centrifugal distortion effects and any dynamical (non-inertial) contributions. For comparison with experiment we define energy differences that may be interpreted in terms of rigid-molecule rotational constants and prolate near-symmetric top centrifugal distortion constants.

Chapter 2: The Argon–Acetylene Complex
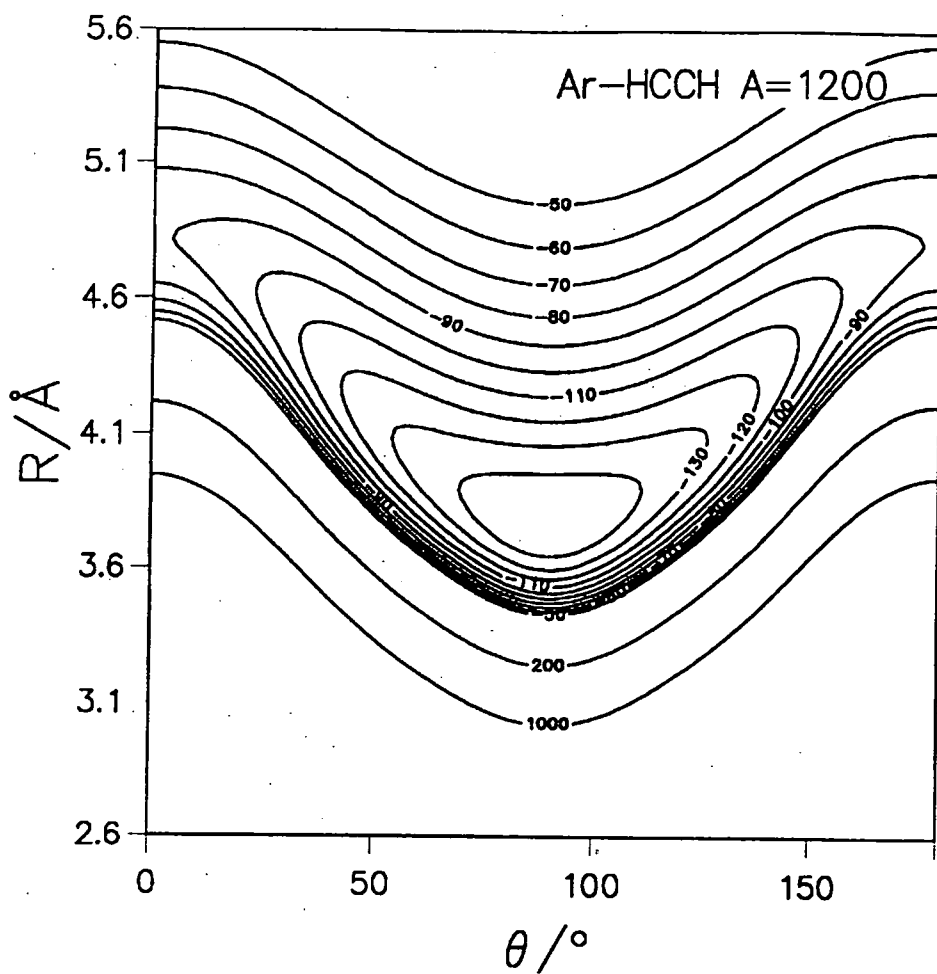
Fig. 2.iii Contour Plot of the $A(1200)$ Potential.

$$\Delta_0 = E(J = 1, K = 0) - E(J = 0) \approx B + C - 4D_J;$$

$$\Delta_f = E(J = 1, K = 1^f) - E(J = 0) \approx A + B - 4D_J - 2D_{JK} - D_K; \quad (2.3)$$

$$\Delta_e = E(J = 1, K = 1^e) - E(J = 0) \approx A + C - 4D_J - 2D_{JK} - D_K.$$

We define *effective* rotational constants $\tilde{A}$, $\tilde{B}$ and $\tilde{C}$ (which include some centrifugal distortion contributions) by

$$\tilde{A} = \tfrac{1}{2}(\Delta_e + \Delta_f - \Delta_0) \approx A - 4D_J - 4D_{JK} - 2D_K;$$

$$\tilde{B} + \tilde{C} = \Delta_0 \approx B + C - 4D_J; \quad (2.4)$$

$$\tilde{B} - \tilde{C} = \Delta_f - \Delta_e \approx B - C.$$

The rotational constant A corresponds to rotation about the R axis. If the

Chapter 2: The Argon–Acetylene Complex

Fig. 2.v Energy levels of Ar-HCCH, calculated for the A(1200) potential, showing the grouping of $J = 2$ levels arising from each monomer j state in a free-internal rotor picture. Energy levels involving excitation of the Van der Waals stretch are shown as dashed lines.

Fig. 2.iv Energy levels of Ar-HCCH, calculated for the A(1200) potential, showing the grouping of $J = 2$ levels arising from each bending state in a near-rigid molecule picture. Energy levels involving excitation of the Van der Waals stretch are shown as dashed lines.

Chapter 2: The Argon–Acetylene Complex

complex was rigid with a T-shaped equilibrium geometry A would be the same as b, the rotational constant of the acetylene monomer. The experimental value of A is 47556 MHz,[36] which may be compared with $b = 35268$ MHz. This deviation indicates the extent of bending in the complex[62] and will depend on the anisotropy of the potential. A measure of R, averaged over the bending and stretching motions is given by $(B+C)$. For completeness we examine $(B-C)$ also. These values are compared with experiment in table 2.II along with the inertial defect $\Delta = I_C - I_A - I_B$ obtained from the calculated rotational constants.

	A(1200)	Expt
$\tilde{A}/$MHz	39130	47556
$(\tilde{B} + \tilde{C})/$MHz	3929	3932
$(\tilde{B} - \tilde{C})/$MHz	143	218
$\Delta/u\text{Å}^2$	5.845	17.964

Table 2.II Comparison of effective rotational constants from the A(1200) potential with experiment.

Clearly these results are very far from the experimental results. The low values for A and Δ suggest two possibilities. Firstly, that the neglected centrifugal distortion has a large effect, or, secondly, that the potential is too rigid.

Hu *et al.*[36] give a value of D_{JK} of 21 MHz. They find D_J to be negligibly small but are unable to determine D_K. This value of D_{JK} will only make a difference of about 0.1 uÅ^2 in Δ, so, lacking further information, the form of the potential was considered.

2.4 INCLUSION OF ANISOTROPY IN THE ATOMIC PARAMETERS

The large discrepancy between the calculated and observed A value implies that the potential is too rigid to bending motions of the complex. Angular anisotropy was therefore introduced to decrease the repulsive wall towards the H-atoms, i.e. to reduce the barrier to distortion from the T-shaped structure. This was achieved by including angular anisotropy in the atomic parameters, in a similar fashion to that used for Ar–C_2H_4,[59] to allow a comparison of the two systems. In work on Ar–C_2H_4[59] anisotropy was introduced using terms $[A_C^0 + A_C^2 P_2(\cos \chi_i)]$ and $[C_C^0 + C_C^2 P_2(\cos \chi_i)]$ for the A_C and C_C coefficients respectively. Here χ_i is defined as the angle between R_i and the vector perpendicular to the plane of the ethylene molecule. This would lead to a potential containing eight adjustable parameters: $A_C^0, A_C^2, A_H, C_C^0, C_C^2, C_H, \beta_C$ and β_H. This is too many to determine from the

limited experimental results available. The basic difference between ethylene and acetylene is in the hybridisation of the carbon atoms, and the choice of parameters was made accordingly. The anisotropy of C_C was neglected and C_C was taken to be 67.1 $E_h a_0^6$ at all angles as before, corresponding to its value at $\chi = 0$ in Ar–C_2H_4. The values of C_H, β_C, β_H were left, as previously, to be the same as the Ar–C_2H_4 parameters.

This leaves A_C^0, A_C^2 and A_H to be determined. The value of $(\tilde{B} + \tilde{C})$ depends mainly on the radial potential around the equilibrium geometry which itself is almost entirely dependent on the value of A_C at $\chi = 90°$,

$$A_C(90°) = A_C^0 - \frac{1}{2}A_C^2. \tag{2.5}$$

It is thus helpful to re-express the repulsive coefficient in terms of $A_C(90°)$ and A_C^2,

$$A_C(\theta) = A_C(90) + A_C^2 \left(\frac{3\cos^2 \theta}{2}\right). \tag{2.6}$$

Thus A_C^2 is expected to be negative as repulsion is expected to be at a maximum at $\theta = 90°$.

Initially the A_H coefficient was fixed at the value of 34.15 E_h used in Ar–C_2H_4. However, attempts to determine A_C^2 and $A_C(90°)$ from $\tilde{A}, \tilde{B} + \tilde{C}$ and $\tilde{B} - \tilde{C}$ found A_C^2 to be so large and negative that the carbon atoms were hardly repulsive at $\chi = 90°$. This was felt to be unphysical, so the effect of changing A_H was investigated.

It was found that any potential with $A_C(90°) = 1150$ E_h reproduced $(\tilde{B} + \tilde{C})$ quite well, irrespective of A_H and A_C^2. This value of $A_C(90°)$ is larger than that for Ar–C_2H_4 (1012 E_h) which seems plausible as the electron density at the molecule centre will be higher for Ar–C_2H_2 than in Ar–C_2H_4.

The value of A_H used for Ar–C_2H_4 appears not to be satisfactory in this system. An sp-hybridised carbon atom is more electronegative than an sp^2 hybridised one. Thus electron density on the hydrogen atom in acetylene will be withdrawn more than in ethylene. This would lead to a smaller value of A_H in Ar–C_2H_2. It was decided to choose three physically plausible values of A_C^2 of −300, −500 and −700 E_h and then to adjust A_H to reproduce the $\tilde{A}$ rotational constant. The parameters of these three potentials, which will be referred to as A(300), A(500) and A(700), are summarised in table 2.III . Contour plots of the A(500) potential are shown in figure 2.vi and the angular dependence of the well depth for all three potentials is shown in figure 2.vii.

Chapter 2: The Argon–Acetylene Complex

	A(300)	A(500)	A(700)
$A_C(90°)/E_h$	1150	1150	1150
A_C^2/E_h	−300	−500	−700
A_H/E_h	24.45	27.67	31.10
β_C/a_0^{-1}	2.132	2.132	2.132
β_H/a_0^{-1}	1.959	1.959	1.959
$C_C/E_h a_0^6$	67.1	67.1	67.1
$C_H/E_h a_0^6$	18.6	18.6	18.6

Table 2.III Parameters of the three pairwise-additive Ar–HCCH potentials.

All the potentials have three minima, one at the T-shaped configuration, and the other two, symmetrically related, around $\theta = 40°$ and $140°$. They are all angularly very flat as would be expected from experimental indications.[36] The A(700) potential has the global minimum at the $40°/140°$ structure whilst the A(300) has its overall minimum at $\theta = 90°$.

These potentials reproduce the basic features of the rotational energy levels, but lack of experimental data means that they are only qualitatively correct. Hopefully predictions of Van der Waals bending and stretching levels from them will provide useful information.

Van der Waals bending and stretching levels were calculated up to 60 cm^{-1} above the ground state for $J = 0, 1$ and 2 for all three potentials. These energy levels are shown in figure 2.viii and 2.ix for the A(500) potential with the free-internal rotor and rigid-rotor groupings as before. Table 2.IV summarises the spectroscopic parameters for the lower vibrational levels for all three potentials. These were calculated from the $J = 0$ and 1 energy levels assuming a near-rigid asymmetric top pattern.

As would be expected, the introduction of atomic anisotropy giving an angularly flatter potential has reduced the rigid-rotor character of the energy levels in favour of the free-internal rotor picture. This now provides a notably better description of the energy levels than the rigid rotor model.

Even in the presence of wide-amplitude motion, experimentalists often interpret band structures in terms of effective rotational and centrifugal distortion constants for a near rigid model of the complex. Such wide-amplitude motion is then observed as highly state-dependent rotational constants and large centrifugal distortion constants. By fitting prolate near-symmetric top formulae to the

Chapter 2: The Argon–Acetylene Complex

Fig. 2.vi Contour Plots of the A(500) Potential.

Chapter 2: The Argon–Acetylene Complex
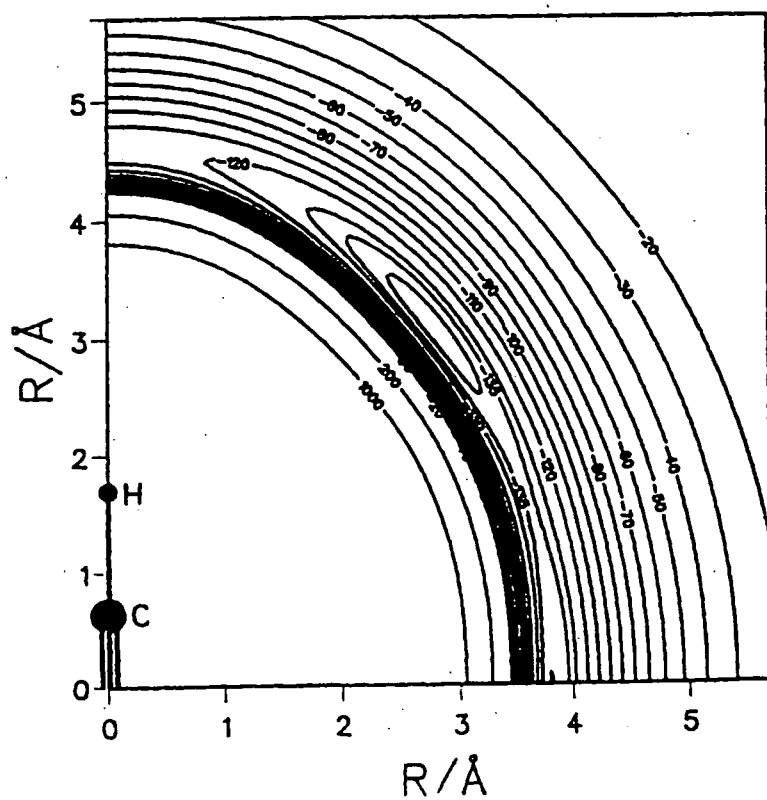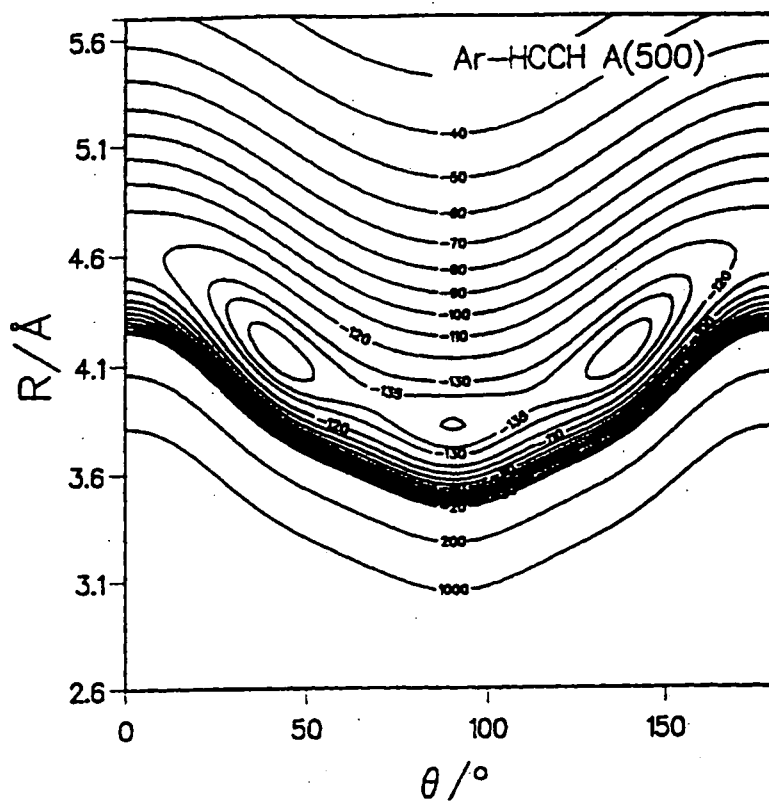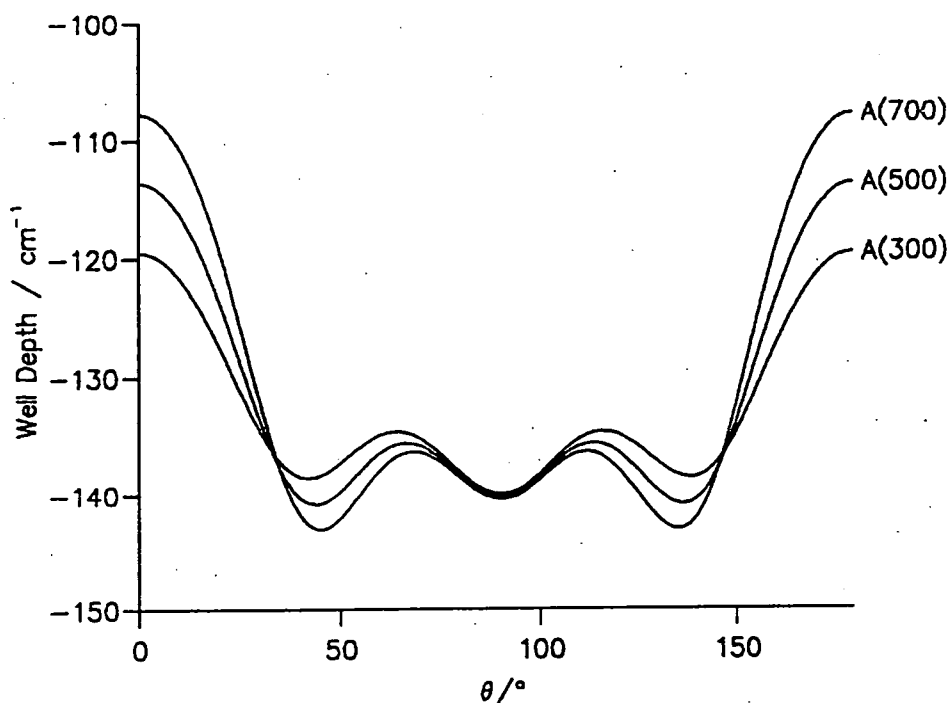
Fig. 2.vii Well depth of the three Ar–HCCH potentials as a function of
angle.

$J = 0, 1$ and 2 energy levels, rotational and centrifugal distortion constants were
determined for the lowest few levels for the A(500) potential. These are shown in
table 2.V The values of A thus determined are significantly different from those
of $\tilde{A}$ calculated previously from the $J = 0$ and 1 levels only.

	A/MHz	B/MHz	C/MHz	D_K/MHz	D_{JK}/MHz
Ground State	48441	2094	1842	942	26
First Bend	84866	2340	1683	4998	−255
Second Bend	116014	2561	1646	11251	−2356
Stretch	53297	1884	1769	2672	−25

Table 2.V Rotational and centrifugal distortion constants calculated
from $J = 0, 1$ and 2 levels of the A(500) potential.

The centrifugal distortion constants D_K are very large. Examination of the
infrared experimental results [36] shows that the A rotational constant is consid-
erably larger (47556 MHz) for the ground state than for the two vibrationally
excited states. However the centrifugal distortion constant D_K was neglected in
the determination of A as it was not possible to determine it from experimen-

Chapter 2: The Argon–Acetylene Complex
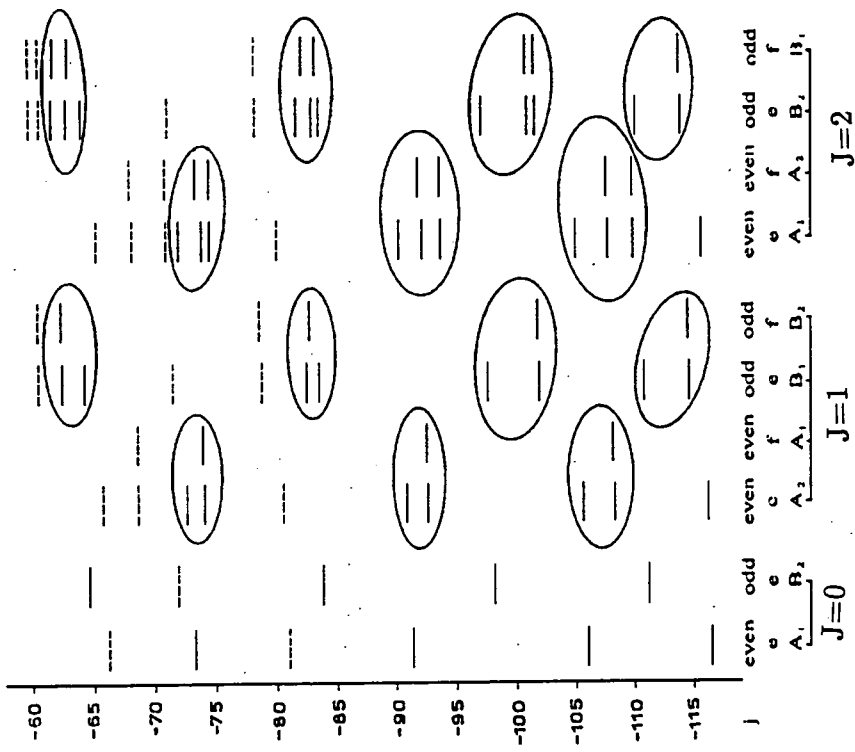
Fig. 2.ix Energy levels of Ar-HCCH, calculated for the A(500) potential, showing the grouping of $J = 2$ levels arising from each monomer j state in a free-internal rotor picture. Energy levels involving excitation of the Van der Waals stretch are shown as dashed lines.
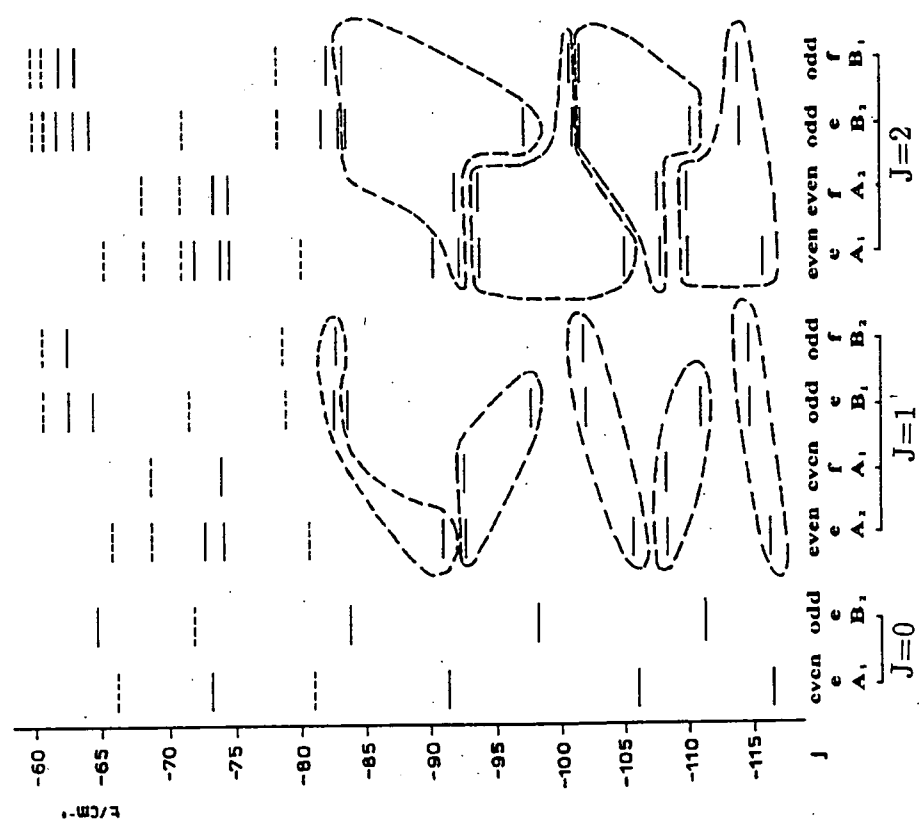
Fig. 2.viii Energy levels of Ar-HCCH, calculated for the A(500) potential, showing the grouping of $J = 2$ levels arising from each bending state in a near-rigid molecule picture. Energy levels involving excitation of the Van der Waals stretch are shown as dashed lines.

Chapter 2: The Argon–Acetylene Complex

		A(300)	A(500)	A(700)	Expt.
Ground State	E_0/cm^{-1}	−115.90	−116.68	−117.43	–
	$\tilde{A}/\text{MHz}$	47409	47446	47503	47471
	$(\tilde{B} + \tilde{C})/\text{MHz}$	3929	3933	3939	3932
	$(\tilde{B} - \tilde{C})/\text{MHz}$	249	252	256	218
	$\Delta/\text{u\AA}^2$	22.1	22.4	23.1	18.0
1st Excited Bend	$(E - E_0)/\text{cm}^{-1}$	5.331	5.301	5.193	
	$\tilde{A}/\text{MHz}$	91898	80284	72849	
	$(\tilde{B} + \tilde{C})/\text{MHz}$	3780	3838	3879	
	$(\tilde{B} - \tilde{C})/\text{MHz}$	1402	653	463	
2nd Excited Bend	$(E - E_0)/\text{cm}^{-1}$	9.506	10.582	11.525	
	$\tilde{A}/\text{MHz}$	132730	109465	92877	
	$(\tilde{B} + \tilde{C})/\text{MHz}$	4880	4077	4041	
	$(\tilde{B} - \tilde{C})/\text{MHz}$	1071	729	552	
Stretch	$(E - E_0)/\text{cm}^{-1}$	35.449	35.641	35.778	
	$\tilde{A}/\text{MHz}$	60111	50669	45638	
	$(\tilde{B} + \tilde{C})/\text{MHz}$	3585	3641	3670	
	$(\tilde{B} - \tilde{C})/\text{MHz}$	88	114	149	

Table 2.IV Comparison of experimental and calculated rotational properties for the Van der Waals ground state, and predictions of properties of Van der Waals Excited states. All rotational constants are calculated from $J = 0$ and 1 levels only.

tal data. All the observed infrared transitions in the work by Hu *et al.*[36] have $\Delta K = \pm 1$ and $K'' = 0$ or 1. The relative frequencies of transitions from $K'' = 1$ to $K' = 0$ and 2 give the splitting between $K' = 0$ and 2 states, which essentially is $4A' - 16D'_K$. If D'_K is neglected then A'_{exp} is actually $A' - 4D'_K$. The transition frequencies for $K'' = 0$ to $K' = 1$ relative to $K'' = 1$ to $K' = 0$ effectively determine $A' - D'_K + A'' - D''_K$. Consequently we propose that neglecting D_K has lead to a falsely high value for A_{exp} for the ground state. The observed splittings can be reproduced with $A'' = A' \sim 46070$ MHz and $D''_K = D'_K \sim 750$ MHz this is a reasonable value of D_K when compared with calculated values of 942 and 818 MHz for the A(500) and A(700) potentials respectively.

Thus with hindsight these three potentials seem to be a little too isotropic, with greater anisotropy needed to reproduce the lower A value suggested above.

Chapter 2: The Argon–Acetylene Complex

An interesting point to note is that, for many Van der Waals states, including the ground state, the even parity level $J = 2, K = 2$ lies below the corresponding odd parity level. This is the reverse of what would be expected from the rigid-rotor levels, where the even parity $K = 2$ level is raised by an interaction with the $K = 0$ level. This effect has been seen experimentally in the lowest vibrational state of Ar–HCCH [36] and its appearance naturally in calculations on a simple potential energy surface is worthy of comment.

2.5 CONCLUSIONS

A preliminary investigation of the intermolecular potential of Ar–HCCH has been carried out using microwave and near infrared spectroscopic data. A basic atom-atom pairwise-additive function has been used and a family of potentials capable of reproducing the ground Van der Waals state has been developed. The potentials are angularly very isotropic between $\theta = 30°$ and $150°$ and the equilibrium geometry could be T-shaped or bent. The barriers to internal rotation vary between 25 cm^{-1} and 40 cm^{-1}, and it is found that free-internal rotor quantum numbers describe the calculated energy level pattern better than near-rigid asymmetric top quantum numbers. Energy levels for excited Van der Waals vibrational modes have been predicted from the three potentials.

2.6 SUBSEQUENT DEVELOPMENTS

Since this work was completed there have been four new significant contributions to the understanding of the Ar–HCCH system. Yang and Watts[43] have performed total differential scattering experiments and have fitted their results to a spherical potential and two anisotropic potentials all based on the Barker potential model. Although their spherical potential could fit their scattering data well, anisotropy was required for agreement with spectroscopic data. They found our A(500) potential could not reproduce their new data and appeared to be overestimating the isotropic well depth by about 10% .

One anisotropic potential developed by Yang and Watts [43] used the angular dependent minimum distance from our A(500) potential and included anisotropy terms in the well depth, C_6 and C_8. These three parameters were then scaled to match our angular anisotropy. Essentially this model assumes we had the correct angular dependence of the potential but overestimated the well depth. The other potential took the spectroscopic T-shaped equilibrium distance of 4.04 Å and introduced the anisotropy in this co-ordinate and in the well depth. Both potentials reproduce scattering and spectroscopic data very well. By comparison

Chapter 2: The Argon–Acetylene Complex

calculations claimed to be on our potential seem to be a factor of up to three in error on vibrational frequencies and force constants. An error is apparent, as the figures quoted by Yang and Watts[43] bear no relationship to those given in table 2.IV and published in 1992.[40] A rough calculation on our A(500) surface, assuming it is quadratic in form, verifies this as it reveals no more than a 20% error from our published figures. Overall, the work of Yang and Watts[43] leads us to conclude that our A(500) potential overestimates the well depth by about 10% and a potential formulated using a combination of this new detail and our angular anisotropy reproduces all the experimental data very well.

Ohshima *et al.*[42] have measured infrared absorption spectroscopy of Ar-HCCH in the doubly degenerate monomer C-H bending region. The Ar atom defines a plane and splits the in and out of plane bends although they remain strongly coupled through Coriolis effects. A semi-rigid fit can be made to the data but the resulting spectroscopic constants have little physical meaning and it is clear a semi-rigid analysis is inappropriate for such a floppy molecule. An analysis which treats the Van der Waals bend as an internal rotation of the HCCH monomer is successful in explaining many observed features by their correlation with the free rotor limit. The C-H bending excitation does not appear to affect the intermolecular potential appreciably and the splitting caused between the degenerate C-H bends can be described by a difference potential of the order of -0.1cm^{-1}.

Bemish *et al.*[41] have studied the region of the $\nu_3/\nu_2 + \nu_4 + \nu_5$ Fermi diad in the acetylene monomer situated at 3294.8424/3281.9048 cm^{-1}. This Fermi resonance is modified upon complex formation and the modification appears to be dependent on intermolecular vibrational excitation. They deduced a bending frequency of 6.222 cm^{-1}, which is a little larger than our prediction, as expected, because our potential is believed to be a little too isotropic. Their data was fit to an ab initio potential calculated using the Hartree-Fock plus damped dispersion method. It was found that to obtain a sufficiently flexible form the dispersion had to be distributed over the four atoms of the acetylene molecule. This potential was then fit to 35 excited state combination differences from the upper diad and gave a good fit for all of the spectroscopic data. This potential corresponded to the vibrationally excited state of HCCH but it was hoped that the small spectral shift from the monomer to complex indicated that the ground state would be very similar. The potential has 2 minima at $\theta = 66°$ and $114°$ with well depths of about -180 cm^{-1}. The $90°$ saddle is about 25 cm^{-1} above the minimum, but this is still below the ground state energy level so the vibrationally averaged structure

is T-shaped. Wavefunction plots reflect the double-well nature. The collocation method was used to calculate energy levels and wavefunctions for this potential and calculated spectra reproduced experimental data very well, any imperfections were attributed to the use of upper state vibrational energy levels for both upper and lower states.

Bone[44] has undertaken ab initio calculations on Ar–HCCH at the MP2 level with several different bases, the best being found to be TZ2P+df/p for the acetylene and [7s6p3d2f] for the argon. The results were consistent with the empirical potentials developed so far for this system but the calculations were plagued with problems from basis set superposition error and little new information on the potential in the well region could be drawn from the outcome.

2.7 SUMMARY

From subsequent work we see that, as commented upon, the potential we have developed is a little too isotropic, underestimating the experimental bending frequency of 6.222 cm^{-1} by about 15% . Until further experimental data, particularly including other Van der Waals vibrational modes, becomes available there is little scope for improving on the potentials now available for the Ar–HCCH system.

Chapter 2: The Argon–Acetylene Complex

Chapter 3: THE ARGON-METHANE COMPLEX

Methane containing systems have received considerable attention as a prototype for spherical top containing systems. In molecule-molecule systems a spherical top can be considered the next stage of complexity after an atom, though the theory of spherical tops is actually more complicated than that of asymmetric tops.[63]

Both theoretical and experimental scattering studies have been performed for methane with He,[64,65] Ne,[64,66–70] Ar,[67–69,71–76] Kr and Xe.[68] Whilst much of the scattering data for Ar–CH_4 may be explained by an isotropic potential[67,68] clear effects of the anisotropy are observed and various potentials that include an anisotropic term have been developed.[71–76,69] Some experimental quantities, such as inelastic cross section, are non-zero only when anisotropy is included.

Several bound state systems have been studied and some theoretical work has already been done on such complexes by Ohshima and Endo,[77] who have observed the microwave spectrum of CH_4–HCl. Microwave spectra of methane-containing complexes have also been measured by Legon et al.[78,79] In addition, Duval and Soep[80] and Fuke et al.[81] have measured electronic spectra of Hg–CH_4, and Wallace and Breckenridge[82] have obtained action spectra of Cd–CH_4 by observing the predissociation products resulting from excitation in the vicinity of atomic cadmium transitions. Also ab initio calculations have been performed on Cd–CH_4 by Ramirez-Solis and Castillo.[83] Recently Dore et al.[84] have measured infrared vibration-rotation tunnelling spectra for CH_4-H_2O.

Since this work was carried out McKellar,[85] Lovejoy and Nesbitt[86] and Block and Miller[87] have measured infrared spectra of Ar–CH_4 in the vicinity of the CH_4 ν_3 band, and Howard and coworkers[88,89] have measured infrared spectra in the analogous band of Ar–SiH_4. These developments will be discussed at the end of this chapter.

Spherical tops have some similarities to asymmetric tops, since their rotational wavefunctions may be expressed as linear combinations of rotation matrices, but there are additional degeneracies arising from the tetrahedral or octahedral symmetry. In this chapter the special features of complexes of spherical tops will be introduced, and the theory will be used to carry out exact (close-coupling) calculations of the bound states of Ar–CH_4.

3.1 SPHERICAL TOP ENERGY LEVELS AND WAVEFUNCTIONS

The theory of atom–spherical top scattering has been developed by Secrest and coworkers.[72,73,90] The coupled equations for the bound state are very similar to those that arise in the scattering theory, though their consequences are quite different in the bound-state case.

If centrifugal distortion and Coriolis coupling are neglected, the rotational energy levels of a spherical top such as CH_4 are simply $E_{j\tau} = bj(j+1)$, where b is the single rotational constant. In this approximation, all the states corresponding to a particular value of j are degenerate. However, centrifugal distortion and Coriolis coupling cause additional splittings, which are very important in spectroscopic work. The rovibrational levels of tetrahedral molecules may be classified under the molecular symmetry group $T_d(M)$[63,91] which is isomorphic to T_d. The notational conventions for CH_4 have been described in a review by Hougen.[63] The possible irreducible representations are A_1, A_2, E, F_1 and F_2. In the vibrational ground state, the $j = 0$ level is of A_1 symmetry, and the $j = 1$ level is of F_1 symmetry. The $j = 2$ states are split into components of E and F_2 symmetry by centrifugal distortion. Higher j states split into more complicated multiplets, as described by Hougen. Where there is more than one level of a given j and symmetry (which occurs for $j > 4$), the different levels are identified by numerical superscripts in order of increasing energy. A tabulation of the energy levels arising from the lowest few j values of the vibrational ground state of CH_4 is given in Table 3.I; a more extensive tabulation has been given by Tarrago *et al.*.[92] The parity of the monomer levels in the vibrational ground state neglecting possible nuclear spin-rotation interaction has been discussed by Oka[93] and is indicated by the label ϵ in the table.

The intermolecular potential is symmetric with respect to any permutation of H atoms, but does not have definite symmetry with respect to inversion of the CH_4 molecule by itself. The coupled equations thus factorise into separate sets of A, E and F symmetry (though the potential does have matrix elements between A_1 and A_2 states and between F_1 and F_2 states).

In order to construct the potential matrix elements in the coupled equations (1.12) or (1.7), the monomer wavefunctions as linear combinations of symmetric top functions (normalised rotation matrices) are required. The lowest few functions of A, E and F symmetry have been given by Heil and Secrest[72] and Smith and Secrest.[73] However, in order to find the monomer functions in the general case, a rotational Hamiltonian matrix is constructed and diagonalised for each

	$\epsilon = +1$	$\epsilon = -1$
j		
0	A_1	
1		F_1
2	F_2,E	E
3	F_2	A_2,F_1
4	A_1,F_2,E	F_1,E
5	F_2,E	$2F_1,E$
6	$A_1,2F_2,E$	A_2,F_1,E
7	$2F_2,E$	$A_2,2F_1,E$
8	$A_1,2F_2,2E$	$2F_1,2E$
9	$A_1,2F_2,E$	$A_2,3F_1,E$

Table 3.I Symmetries of rotational states for the ground vibrational state of a tetrahedral molecule. The states are labelled by the parity ϵ.

monomer angular momentum j, including the tetrahedral centrifugal distortion term d_t. The matrix elements needed are[94]

$$\langle jk|H_{\mathrm{mon}}|jk\rangle = bj(j+1) - d_j j^2(j+1)^2$$
$$+ \tfrac{1}{2}d_t[-3j(j+1)(j(j+1)-2) + 30(j(j+1)-2)k^2 - 35k^2(k^2-1)];$$

$$\langle jk|H_{\mathrm{mon}}|jk\pm 4\rangle = \tfrac{5}{4}d_t\{[j(j+1)-k(k\pm 1)][j(j+1)-(k\pm 1)(k\pm 2)]$$
$$\times [j(j+1)-(k\pm 2)(k\pm 3)][j(j+1)-(k\pm 3)(k\pm 4)]\}.$$

$$(3.1)$$

The functions resulting from the numerical diagonalisation span the A, E and F representations of $T_d(M)$. However, for the degenerate representations, the eigenvectors returned can be arbitrarily mixed with one another, and do not necessarily have convenient symmetries with respect to the coordinate axes. Linear combinations of the original degenerate eigenvectors were thus constructed that (i) have definite symmetry ($+1$ or -1) with respect to the symmetry operation σ_{xz}, which carries D^j_{mk} into $(-1)^{j-k}D^j_{m-k}$; and (ii) contain only even k or odd k functions. For the F representation, this produces three equivalent and independent sets of coupled equations, and it is only necessary to solve one of these.

The BOUND program[95] can perform properly symmetrised atom + spherical top calculations, within the framework of its atom + asymmetric top code. This automatically provides the capability to carry out both close-coupling and helicity decoupling calculations. The close-coupling calculations are carried out in the space-fixed representation.

Chapter 3: The Argon-Methane Complex

3.2 THE INTERMOLECULAR POTENTIAL

An atom-molecule potential may in general be expanded in terms of renormalised spherical harmonics as in Eq. (1.4). As discussed by Green,[20] it is generally convenient where possible to choose the monomer axis system (x, y, z) so that the xz plane is a monomer plane of symmetry, since then $V_{\lambda\mu}(R) = (-1)^{\mu} V_{\lambda-\mu}(R)$, and the potential expansion simplifies to

$$V(R, \theta, \chi) = \sum_{\lambda \geq \mu \geq 0} V_{\lambda\mu}(R)[C_{\lambda\mu}(\theta, \chi) + (-1)^{\mu} C_{\lambda-\mu}(\theta, \chi)]/(1 + \delta_{\mu 0}). \quad (3.2)$$

The BOUND program used to solve the coupled differential equations in the present work requires that this is true. Unfortunately, the coordinate system used by Secrest and coworkers[72,73] does not have this property. They used a coordinate system in which the H atoms of CH_4 are located at opposed vertices of a cube, with the edges of the cube along the x, y and z axes. A slightly different coordinate system was therefore chosen, with the same z axis but an x axis along the line joining two H atoms. This axis system is rotated by 45° about the z axis compared to that of Secrest and coworkers and is illustrated in figure 3.i.

The lowest-order non-zero potential terms for Ar–CH_4 are $V_{00}(R)$, $V_{32}(R)$, $V_{40}(R)$, $V_{44}(R)$, $V_{64}(R)$ and $V_{60}(R)$. However, these are not all independent, because of the symmetry of the monomer:

$$V_{44}(R) = -(5/14)^{\frac{1}{2}} V_{40}(R);$$

$$V_{64}(R) = (7/2)^{\frac{1}{2}} V_{60}(R). \quad (3.3)$$

Secrest and coworkers expanded the potential slightly differently,

$$V(R, \theta, \chi) = V_0(R) + V_3(R) T_3(\theta, \chi) + V_4(R) T_4(\theta, \chi) + V_6(R) T_6(\theta, \chi), \quad (3.4)$$

where the angular functions $T_\lambda(\theta, \chi)$ are combinations of spherical harmonics defined in ref. 72, and in our axis system are

$$T_3 = (7/4\pi)^{\frac{1}{2}} [C_{32}(\theta, \chi) + C_{3-2}(\theta, \chi)];$$

$$T_4 = -(45/4\pi)^{\frac{1}{2}} [C_{44}(\theta, \chi) + C_{4-4}(\theta, \chi)] + (126/4\pi)^{\frac{1}{2}} C_{40}(\theta, \chi); \quad (3.5)$$

$$T_6 = (91/4\pi)^{\frac{1}{2}} [C_{64}(\theta, \chi) + C_{6-4}(\theta, \chi)] + (26/4\pi)^{\frac{1}{2}} C_{60}(\theta, \chi).$$

Chapter 3: The Argon-Methane Complex
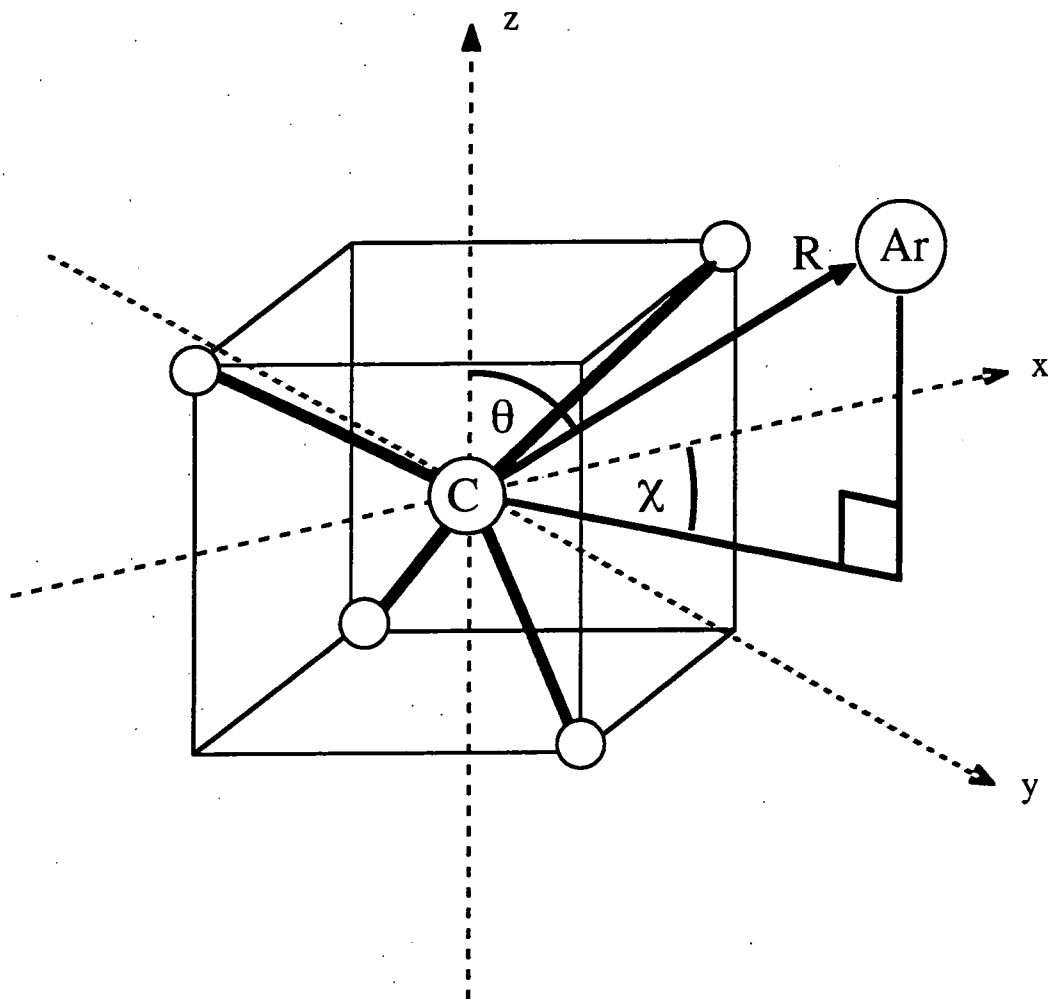
Fig. 3.i Monomer fixed coordinate system used for Ar–CH₄.

The relationships between the $V_\lambda(R)$ coefficients of Secrest and coworkers and our $V_{\lambda\mu}(R)$ are thus

$$V_{00}(R) = V_0(R);$$

$$V_{32}(R) = (7/4\pi)^{\frac{1}{2}} V_3(R);$$

$$V_{40}(R) = (126/4\pi)^{\frac{1}{2}} V_4(R);$$

$$V_{60}(R) = (26/4\pi)^{\frac{1}{2}} V_6(R).$$

(3.6)

There has been a considerable amount of work on the intermolecular potential of Ar–CH₄.[67−69,71−76] In the present work, the potential of Buck *et al.*[75] was used (BKPS potential); this was obtained from experimental total differential cross sections measured at a collision energy of 90.1 meV.[74] The isotropic part of this

Chapter 3: The Argon-Methane Complex

potential has a Morse-spline-Van der Waals (MSV) functional form,

$$V_0(R) = f(x) \cdot \epsilon$$

where $x = R/R_m$ and

$$
\begin{aligned}
f(x) &= \sum_{i=0}^{3} a_i(x - x_1)^i, & x &\leq x_1, \\
&= \exp[2\beta_2(1 - x)] - 2\exp[\beta_2(1 - x)], & x_1 &< x < x_2, \\
&= \sum_{i=0}^{3} b_i(x - x_3)^i, & x_2 &\leq x \leq x_3, \\
&= -c_6 x^{-6} - c_8 x^{-8}, & x &\geq x_3.
\end{aligned}
\tag{3.7}
$$

Here ϵ and R_m are the depth and position of the potential well respectively and

$$
\begin{aligned}
a_3 &= \frac{2}{(x_1)^3}(V_L - V_R) + \frac{1}{(x_1)^2}(V_L' + V_R'), \\
a_2 &= \frac{3}{(x_1)^2}(V_R - V_L) + \frac{1}{(x_1)}(2V_L' + V_R'), \\
a_1 &= V_L', \\
a_0 &= V_L,
\end{aligned}
\tag{3.8}
$$

where the L and R subscripts denote values of the potential on the left and right (x_1 and x_2 respectively), and V' denotes the derivative of the potential. Similar equations define the b_i. The parameters used are detailed in Table 3.II .

ϵ/meV	14.4
R_m/Å	3.88
c_6	1.23345
c_8	0.446167
β_1	7.0
β_2	7.0
x_1	0.1
x_2	1.10
x_3	1.40

Table 3.II Potential Parameters for Isotropic Part of BKPS Potential.

Chapter 3: The Argon-Methane Complex

The anisotropy is represented by a $V_3(R)$ potential given by

$$V_3(R) = \epsilon \alpha_r^{(3)} \exp[2\beta_1(1 - R'/R_m)] - \epsilon \alpha_a^{(3)} C_6 (R_m/R')^7, \qquad (3.9)$$

where ϵ, R_m, β_1, and C_6 were taken from the isotropic potential and anisotropic coefficients $\alpha_r^{(3)} = 0.78$ and $\alpha_a^{(3)} = 0.58$ (defined in ref. 75 as fractions of the repulsive and attractive parts of the isotropic potential), obtained from time-of-flight measurements of inelastic differential cross sections.[75] The coefficients $V_0(R)$ and $V_3(R)$ are shown in figure 3.iia. Cuts through the BKPS potential for face, edge and vertex geometries are shown in figure 3.iib.

3.3 BOUND-STATE CALCULATIONS

3.3.1 Close-coupling calculations

Close-coupling calculations were carried out for the lower bound states of Ar–CH_4 for $J = 0$, 1 and 2, using the BKPS potential; the results are summarised in Table 3.III and figure 3.iii . The close-coupling calculations were carried out in the space-fixed representation. The CH_4 energy levels were calculated from the rotational and centrifugal distortion constants of Tarrago et al.,[92] $b = 5.2410356$ cm^{-1}, $d_j = 1.10864 \times 10^{-4}$ cm^{-1} and $d_t = -4.425 \times 10^{-6}$ cm^{-1}. Note that the sign of d_t in the present work is different from that given by Tarrago et al., because of the different coordinate system used here.

The coupled equations were solved using the modified log-derivative propagator of Manolopoulos.[31] The log-derivative matrix was propagated from $0.71 R_m$ to $2.5 R_m$, with a step size of $0.002 R_m$. The reduced mass was taken to be 11.44145053 u. The basis set used included all CH_4 levels up to $j = 13$. The resulting calculations are converged to within 10^{-5} cm^{-1}.

For each J and symmetry block (A, E or F), the coupled equations factorise into two blocks, with even and odd total parity (symmetry under space-fixed inversion). In the space-fixed representation, the channel $j\tau LJ$ has total parity $p' = \varepsilon(-1)^L$, where ε is the parity of the monomer wavefunction.[93] As will be seen below, it is generally more convenient to work with the *parity label* $p = p'(-1)^J = \varepsilon(-1)^{L+J}$ rather than the parity itself.

The pattern of levels for A states is fairly straightforward. For $J = 0$, there is only one channel, $L = j$, arising from each $j\tau$ level of CH_4; this channel has

Chapter 3: The Argon-Methane Complex
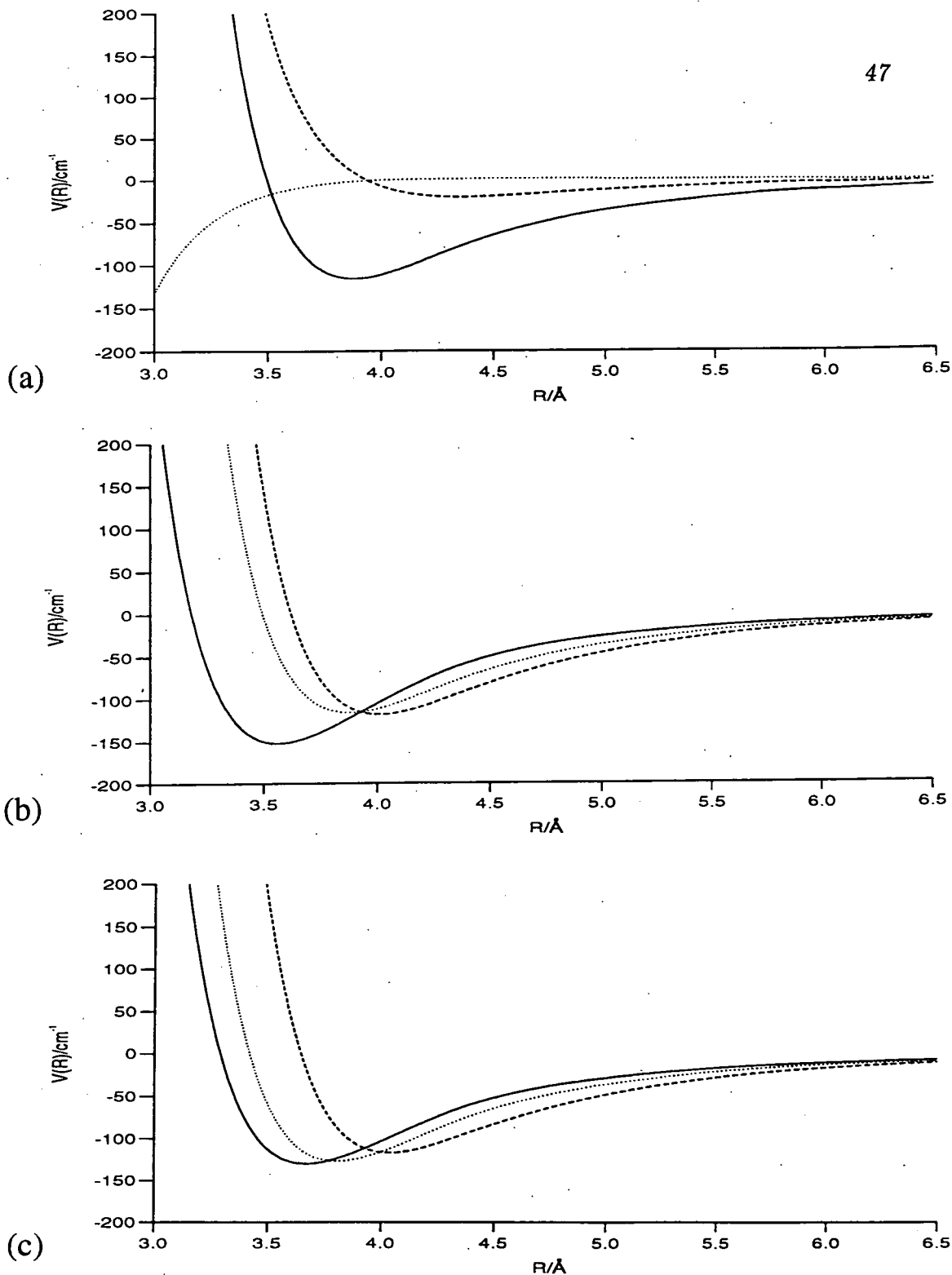
Fig. 3.ii (a) Potential coefficients for the BKPS and modified Ar–CH$_4$ potentials: solid line, $V_0(R)$; dashed line, $V_3(R)$; dotted line, $V_4(R)$ (included in modified potential only). (b) Radial cuts through the BKPS potential for various geometries of approach: solid line, Ar atom over face of tetrahedron; dashed line, vertex; dotted line, edge. (c) Radial cuts through the modified potential for various geometries of approach: solid line, Ar atom over face of tetrahedron; dashed line, vertex; dotted line, edge.

Chapter 3: The Argon-Methane Complex

j	Γ	n	J = 0		J = 1		J = 2	
			p = +1	p = −1	p = +1	p = −1	p = +1	p = −1
0	A	0	−95.524		−95.333		−94.952	
1	F	0	−85.304		−85.331	−85.037	−85.134	−84.654
					−84.818		−84.250	
2	F	0	−66.375		−66.246	−63.896	−65.987	−64.331
					−63.839		−64.297	−63.368
							−63.236	
0	A	1	−62.333		−62.464		−62.107	
2	E	0	−62.215	−62.215	−68.734	−68.734	−68.385	−68.385
					−62.257	−62.257	−65.418	−65.418
					−61.609	−61.609	−62.087	−62.087
							−62.019	−62.019
							−60.985	−60.985
1	F	1	−47.581		−50.848	−50.847	−50.496	−50.493
					−47.400		−47.037	
0	A	2	−40.011		−39.857		−39.549	
2	F	1	−37.420		−37.290	−34.704	−38.716	−38.715
					−34.655		−37.025	−34.402
							−34.260	
3	F	0	−26.934	−30.702	−29.976	−30.695	−30.905	−30.955
					−27.067	−29.790	−29.529	−29.154
					−26.568	*	−26.858	−26.440
							−26.030	−23.251
							−23.251	*
3	A	0	−26.450		−30.741	−30.701	−30.961	−30.907
					−26.240		−29.790	−29.722
							*	
2	E	1	−26.105	−26.105	−32.043	−32.043	−31.717	−31.717
					−26.797	−26.767	−30.714	−30.714
					−25.836	−25.836	−26.964	−26.964
							−26.582	−26.582
							−25.337	−25.337

Table 3.III Close-coupling calculations of energy levels of Ar–CH$_4$ using the BKPS potential. All energies are given in cm^{-1}, relative to the dissociation threshold. Levels marked with * were not found, and must lie above −22 cm^{-1}.

*Chapter 3: The Argon-Methane Complex*
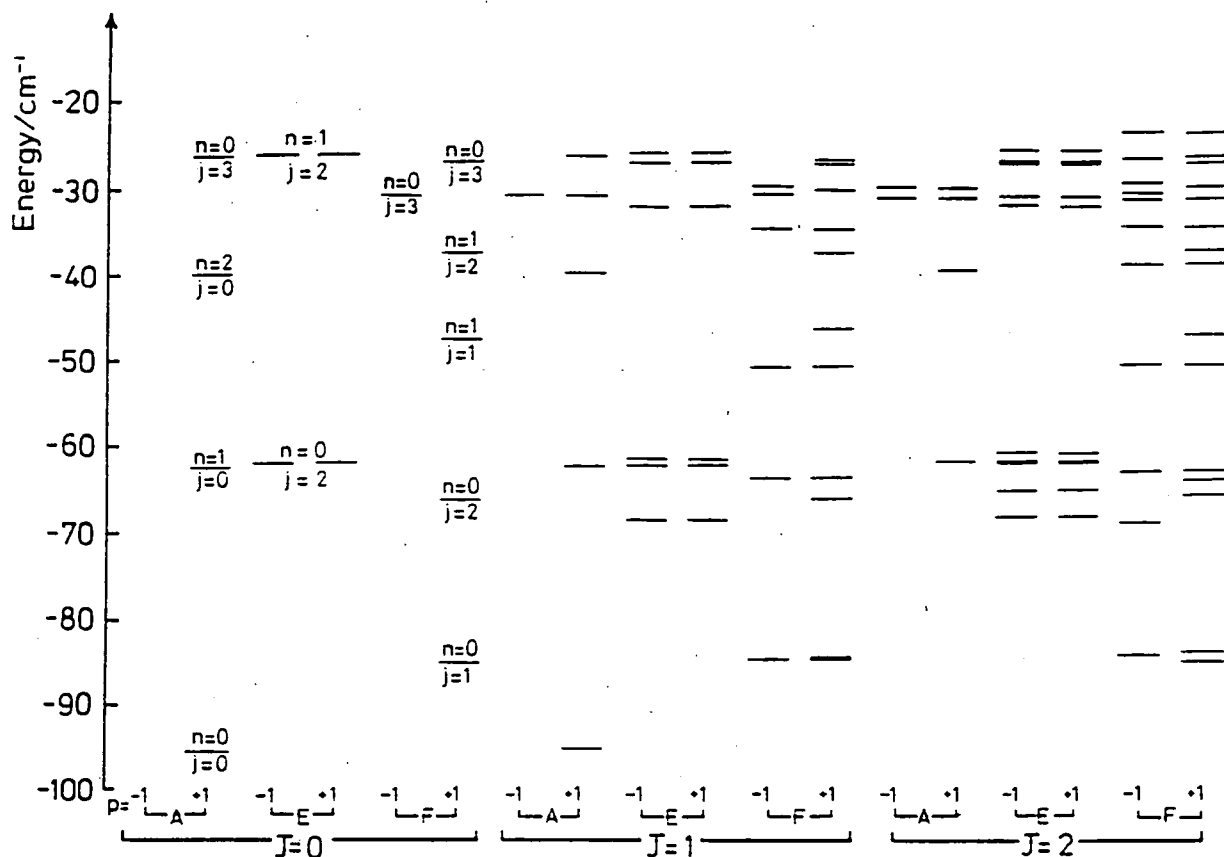
Fig. 3.iii Close-coupling calculations for energy levels of Ar–CH$_4$ on the BKPS potential.

parity $\varepsilon(-1)^j$, so contributes to only one of the two sets of equations. In fact, the A levels arising from $j = 0$, 3 and 4, and the A_1 level arising from $j = 6$, enter the equations for $+$ parity; the lowest A channel in the equations for $-$ parity arises from the $j = 6$ A_2 level. The states are well described by a j quantum number, and the pattern of levels is fairly close to that expected for a free internal rotor, $E_j = bj(j+1)$. The Ar–CH$_4$ stretching frequency is about 33 cm^{-1} for the BKPS potential, so that the excited stretching levels are interspersed with the excited internal rotor levels. The intermolecular stretching quantum number is denoted n.

The F levels for $J = 0$ follow much the same pattern. The $j = 1$ F_1, $j = 2$ F_2 and $j = 3$ F_1 levels all enter in the equations for $+$ parity, and the lowest $-$ parity

Chapter 3: The Argon-Methane Complex

level for $J = 0$ arises from $j = 3$ F_2. The E levels are slightly different, because in this case *both* monomer parities exist for each $j\tau$ level: the consequence is that levels of the complex occur at identical energies for both total parities.

For $J > 0$, there are several L channels arising from each $j\tau$ level. In general, there are $2\mathcal{J} + 1$ such channels, where $\mathcal{J}$ is the smaller of j and J. For $j\tau$ levels with $\varepsilon(-1)^j = +1$, there are $\mathcal{J} + 1$ channels with $p = +1$ and $\mathcal{J}$ with $p = -1$. Conversely, for $j\tau$ levels with $\varepsilon(-1)^j = -1$, there are $\mathcal{J}$ channels with $p = +1$ and $\mathcal{J} + 1$ with $p = -1$. Although the potential anisotropy mixes and shifts the levels, the *number* of levels that arise for each $j\tau Jp$ is simply explained by these considerations.

The splittings between the different states for each $j\tau Jn$ combination are best explained in terms of body-fixed quantum numbers $j\tau JKn$, where the body-fixed projection quantum number K can take values from $-\mathcal{J}$ to $+\mathcal{J}$. If Coriolis couplings are neglected, the body-fixed coupled equations are diagonal in K. For each K and symmetry type, the different $j\tau$ levels are coupled by the potential anisotropy. For $K > 0$, the levels arising from $+|K|$ and $-|K|$ do not have definite total parity. The appropriate parity-symmetrised functions are linear combinations of these functions,

$$[2(1 + \delta_{K0})]^{-\frac{1}{2}} \left[\Phi_{j\tau K}^{JM}(\alpha_R, \beta_R, \phi, \theta, \chi) + \Phi_{j\tau -K}^{JM}(\alpha_R, \beta_R, \phi, \theta, \chi) \right]. \tag{3.10}$$

For complexes of non-linear molecules, it is important to realise that the potential anisotropy may mix monomer levels of the same j but different τ; if these correspond to degenerate states of the monomer, a first-order shift may result even if there are no diagonal matrix elements in the basis set of monomer eigenfunctions. This is particularly important when the potential anisotropy breaks the monomer parity. Thus, for example, it would be usual to label the rotational levels of a monomer such as NH_3 with values of $|k|$ and parity. However, in a complex such as Ar–NH_3,[96] there are potential matrix elements (V_{10}, V_{30} etc.) that couple monomer levels of different parity, and (for a given non-zero K), cause equal and opposite shifts for states with positive and negative k. A similar effect occurs for complexes of tetrahedral molecules: for $K \neq 0$, the V_3 anisotropy couples states of the same j but different monomer parity. Since V_3 is always likely to be larger than the monomer splittings between such states, it causes first-order splittings for states with $K > 0$ whenever this occurs.

When Coriolis coupling is reintroduced, it couples states of the same total parity with $\Delta|K| = \pm 1$. The effect is thus to split any remaining degeneracy of

the even and odd parity states of the same $|K|$. Such splittings are largest for $|K| = 1$, and are usually such that the even parity $|K| = 1$ state moves away from the corresponding $K = 0$ state.

With this background, the splittings of the $J = 1$ states in Fig. 3.iii are readily understood. For each $J = 0$ state, there is a corresponding $J = 1$, $K = 0$ state of the same parity label p (i.e. opposite total parity). To a first approximation (neglecting Coriolis couplings), the splitting between these two states is just $2B$, where B is the rotational constant of the complex. In addition, for $j > 0$, there is a pair of $|K| = 1$ states, one of each total parity. The separations between the different K states are determined principally by the potential anisotropy, and *not* by rotational constants; they will be discussed in more detail later. If the splitting between the $K = 0$ and $|K| = 1$ states is small, Coriolis coupling causes substantial mixing between the $K = 0$ level and the $|K| = 1$ level of the same symmetry. If this occurs, the splitting between the $J = 0$ and $J = 1$, $K = 0$ states is not simply related to a rotational constant.

3.3.2 Helicity decoupling calculations

The accuracy of the body-fixed description may be determined by comparing close-coupling calculations with helicity decoupling (coupled states) calculations. Helicity decoupling results for $J = 1$ and 2 states on the BKPS potential are given in Table 3.IV. The accuracy of the approximation varies greatly for level to level. For some levels, such as most A states and the $j = 2$, F_2 states, the splitting between states of different K is large compared to the rotational constant of the complex; the helicity decoupling approximation is then reasonably accurate, and well-defined K labels can be assigned to the close-coupled levels. For other levels, such as the $j = 1$, F_1 levels for $n = 0$, the levels of different K are nearly degenerate, and the helicity decoupling approximation breaks down.

3.3.3 Splittings between K states

The $V_3(R)$ anisotropy in the BKPS potential is positive at short range and negative at long range, and changes sign around 3.9 Å. This is very close to the average value of R for the $n = 0$ states of the Ar–CH$_4$ complex. The consequence of this is that $\Delta n = 0$ matrix elements of the $V_3(R)$ anisotropy are fairly small, while $\Delta n = \pm 1$ matrix elements are relatively large. The effect of this may be seen in some of the splittings in Fig. 3.iii : for example, the splitting between

j	Γ	n	$J = 1$		$J = 2$		
			$K = 0$	$K = \pm1$	$K = 0$	$K = \pm1$	$K = \pm2$
0	A	0	−95.333		−94.951		
1	F	0	−85.111	−85.037	−84.727	−84.654	
2	F	0	−66.184	−63.896	−65.803	−63.517	−64.180
0	A	1	−62.463		−62.102		
2	E	0		−68.719		−68.317	−65.384
			−62.026	−61.649	−61.491	−62.048	
1	F	1	−47.407	−50.844	−47.058	−50.485	
0	A	2	−39.844		−39.512		
2	F	1	−37.237	−34.681	−36.872	−34.320	−30.794
3	F	0	−30.513	−29.966	−30.135	−29.605	−30.794
			−26.760	−26.887	−26.413	−26.531	−23.272
3	A	0	−26.288	−30.701	−25.964	−30.322	−30.306
2	E	1		−32.031		−31.661	−30.692
			−25.934	−26.709	−25.593	−26.380	−26.981

Table 3.IV Helicity decoupling calculations of energy levels of Ar–CH$_4$ using the BKPS potential. Energies are given in cm^{-1}, relative to the dissociation threshold.

the two $p = +1$ states is much smaller for the $j = 1$, F_1, $n = 0$ state than for the corresponding $n = 1$ state: this is probably because the dominant potential coupling in both cases is to the $j = 2$, F_2, $n = 0$ state, which is located roughly half way between the two $j = 1$ states, but is coupled much more strongly to the $j = 1$, $n = 1$ state.

3.3.4 Effect of higher-order anisotropies

The T_3 angular function has no matrix elements diagonal in j in the free-rotor basis set for $K = 0$ states or for other K states for A symmetry, $j < 6$ or F symmetry, $j < 3$. However, the T_4 angular function *does* have diagonal matrix

elements for rotor functions with $j \geq 2$. It may thus be expected that the presence of a $V_4(R)$ anisotropy will have considerable effects on the spectrum. In order to investigate this effect, calculations were carried out on a modified potential, based on the BKPS potential, but including a $V_4(R)$ anisotropy defined by $\alpha_r^{(4)} = -0.06$ and $\alpha_a^{(4)} = -0.03$. The resulting $V_4(R)$ is included in figure 3.iia, and cuts through the potential for face, edge and vertex geometries are shown in figure 3.iic. Close-coupling calculations on the $J = 0$, 1 and 2 states for this potential are shown in figure 3.iv . It may be seen that the pattern of levels is indeed quite different for states with $j \geq 2$.
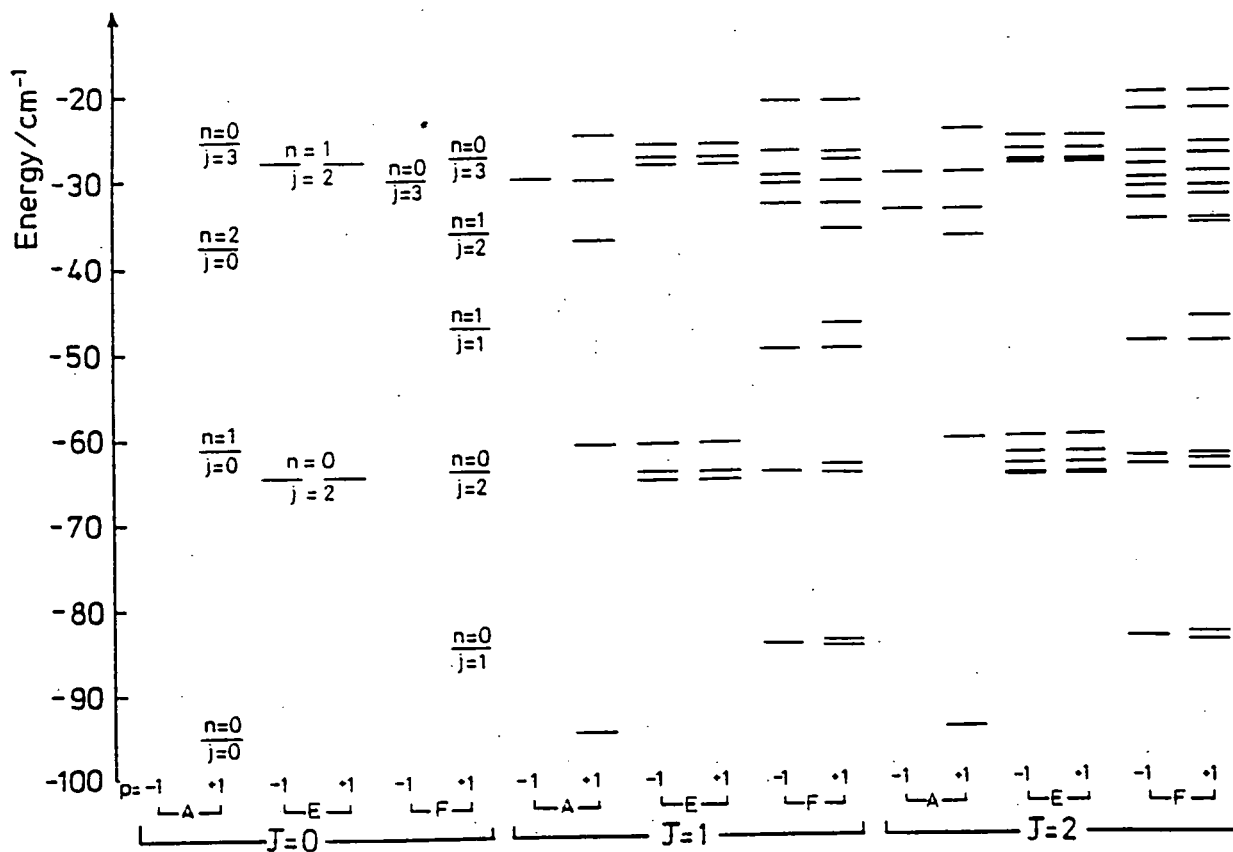
Fig. 3.iv Close-coupling calculations for energy levels of Ar–CH$_4$ on the modified potential.

As part of a paper published on this work[18] Hutson has constructed correlation diagrams for atom–tetrahedral molecule bending states by considering an

Chapter 3: The Argon-Methane Complex

effective bending Hamiltonian

$$H_{\text{bend}} = b\hat{j}^2 + V_3 T_3(\theta, \chi) + V_4 T_4(\theta, \chi). \qquad (3.11)$$

The Hamiltonian matrix is constructed in a body-fixed basis set, and diagonalised to produce bending energy levels. The Hamiltonian (3.11) excludes all rotational terms, including Coriolis coupling, so the K quantum number is conserved.

The correlation diagrams for increasing V_3, with V_4 fixed at zero, are shown in figure 3.v for A, F and E symmetries. The diagrams are an extended version of the correlation diagram given by Ohshima and Endo.[77] The levels at the centre of the diagrams are free-internal-rotor levels, labelled by j. As the anisotropy increases, each $j\tau$ level for A or F symmetry splits into $j + 1$ components, and each $j\tau$ level for E symmetry splits into $2j + 1$ components. The T_3 potential has matrix elements that couple monomer states of the same parity if $j + j'$ is odd, and of different parity if $j + j'$ is even. Accordingly, the splittings are first-order (linear in V_3) only if there are degenerate states of the same symmetry (A, E or F) but different parity. This occurs for all E states, as described above, for F states with $j \geq 3$, and for A states with $j \geq 6$. Other states show second-order splittings (quadratic in V_3). In addition, states with $K = 0$ show only second-order splittings, because the second 3-j symbol in Eq. (1.14) is zero if $K = 0$ and $j + \lambda + j'$ is odd.

The energy levels for relatively low anisotropies ($V_3 \leq 10b$) are thus characterised by quantum numbers j and K. The symmetry label A, E or F is also conserved, but in many cases the levels of the complex cannot be identified with a single sublevel of the monomer (such as F_1 or F_2). For higher anisotropies, near the sides of 3.v, the j quantum number is lost, and the energy level pattern becomes that of a near-rigid bender (two-dimensional harmonic oscillator). This may be seen more clearly in figure 3.vi a, which collects together the levels for A, E and F symmetry for $K \leq 2$. The lowest bending state, $v_b = 0$, has no vibrational angular momentum, and supports a ladder of levels with rotational angular momentum $|K|$ about the intermolecular axis: the rotational energy of these states is approximately bK^2. The first excited bending state, $v_b = 1$, has an intermolecular vibrational angular momentum $l = \pm 1$ about the intermolecular axis (this must not be confused with the vibrational angular momentum that can arise when the monomer is vibrationally excited). Each K level for $K \neq 0$ is then split into two by a Coriolis interaction: for states with arbitrary l and

(a)

(b)

(c)
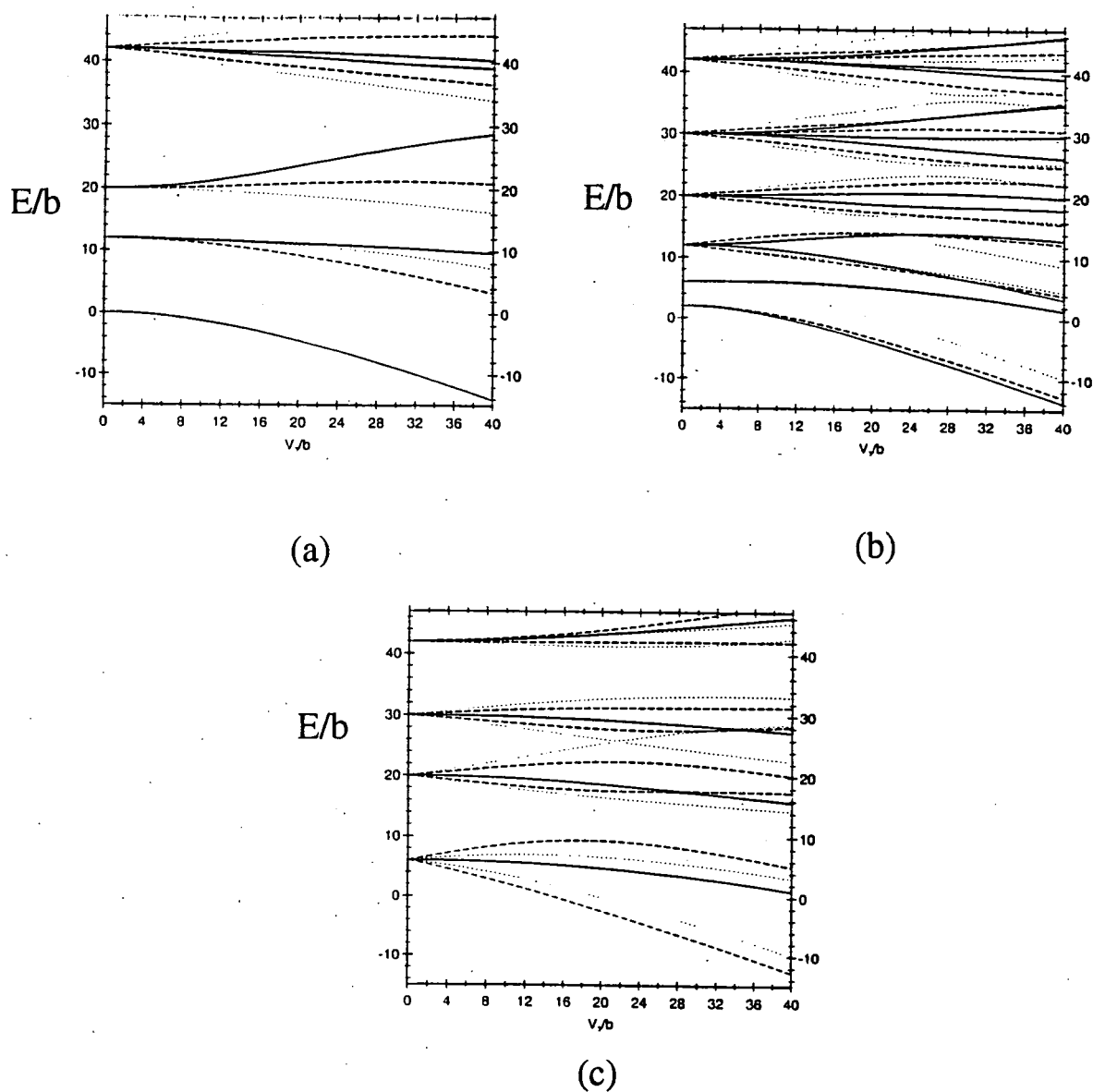
Fig. 3.v Correlation diagrams for energy levels of atom–tetrahedral molecule complexes, as a function of increasing V_3 anisotropy. (a) A states; (b) F states; (c) E states. Only levels with $K \leq 2$ are shown. Solid lines are $K = 0$ states; dashed lines are $K = 1$ states; dotted lines are $K = 2$ states.

K, the Coriolis term has magnitude $-2b\zeta Kl$,[97,98] where ζ is a Coriolis coupling constant. If ζ is close to 1, the rotational energy about the intermolecular axis is principally determined by a pseudo-rotational quantum number $|\overline{K}| = |K - l|$, and is approximately $b\overline{K}^2 - 2b(1 - \zeta)Kl$.

Chapter 3: The Argon-Methane Complex

In reality, any complex between an atom and a tetrahedral molecule will have at least a small V_4 anisotropy. The T_4 anisotropy has diagonal matrix elements for almost all levels with $j \geq 2$, even for $K = 0$. The energy levels are shown as a function V_3 in figure 3.vi b, for a small fixed V_4 anisotropy, $V_4 = b$. The pattern is considerably more complicated than that in figure 3.v around $V_3 = 0$, where the splittings are now dominated by V_4, but for large V_3 (roughly, $V_3 > 15b$) there is very little difference in the patterns.

In the Ar–CH_4 complex where $b = 5.241$ cm^{-1} the V_3 term from the BKPS potential, at the isotropic equilibrium bond length of 3.88 Å, is 7.1cm^{-1} and the V_4 term added in modification is -2.7 cm^{-1}. Thus we would expect a significant effect.
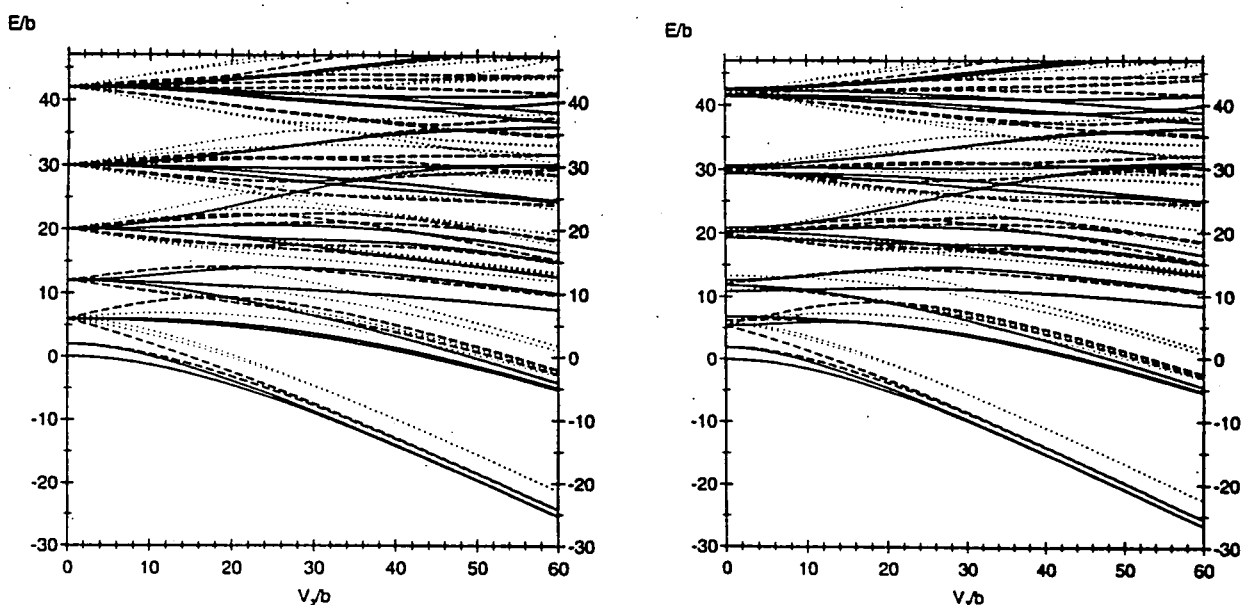

Fig. 3.vi (a) Correlation diagram for $K \leq 2$ energy levels of atom-tetrahedral molecule complexes, showing energy levels for all three symmetries as a function of increasing V_3 anisotropy for $V_4 = 0$. (b) Correlation diagram as for part (a), but with $V_4 = b$. Solid lines are $K = 0$ states; dashed lines are $K = 1$ states; dotted lines are $K = 2$ states.

3.4 VIBRATIONAL ANGULAR MOMENTUM

The excited states of spherical top molecules that are accessible in infrared spectroscopy involve degenerate vibrational states of F symmetry. These states have a vibrational angular momentum which gives rise to important structure in the monomer spectrum.

Chapter 3: The Argon-Methane Complex

In formal terms, there is no difficulty in including vibrational angular momentum in the coupled equations. The Hamiltonian of Eq.1.2 remains essentially valid, except that H_{mon} must include vibration-rotation coupling terms. In addition, the intermolecular potential is of lower symmetry, because the interaction energy depends on the angle between the intermolecular vector and the axis of the vibrational excitation. The resulting terms resolve the degeneracy between the different components of the degenerate vibration. However, the main qualitative effects may be expected to be due to the monomer vibrational angular momentum. Inclusion of the monomer vibrational angular momentum is beyond the scope of this thesis, and the reader is referred to the literature for more information.[18,63,88,99−101]

3.5 DISCUSSION AND RECENT DEVELOPMENTS

Both close-coupling and helicity decoupling calculations have been performed for Ar–CH$_4$ on two different interaction potentials. The first potential is that of Buck et al.,[75] and contains only a single anisotropic term, $T_3(\theta, \chi)$. The second potential is modified to include a small T_4 anisotropy, which is important because it causes first-order shifts for several states that are affected by T_3 only in second order.

The energy levels from the close-coupling calculations have been interpreted using a picture in which the CH$_4$ undergoes hindered rotation in the complex. The monomer rotational quantum number j is quantised along the intermolecular axis, with a body-fixed projection described by the nearly good quantum number K. To understand the bending levels in more detail, correlation diagrams connecting the free-rotor energy levels with near-rigid energy levels, as a function of the potential anisotropy which were constructed by Hutson[18] have been used.

Since this work was carried out the theory for the energy levels of the complex with the monomer in the triply degenerate vibrational state has been laid out in more detail by Randall et al.[88] who have used their model to interpret the spectrum of Ar–SiH$_4$ in the $\nu_3 = 1$ vibrational state of silane.[89]

For Ar–SiH$_4$ it was found that a model that separates the internal rotation from the end over end rotation of the complex and neglected the dependence of the potential upon R could adequately explain the spectrum. The rotational anisotropy in this system was found to be about 90cm^{-1} whilst the anisotropy

due to the vibration was of the order of $1 cm^{-1}$. In other words the triply degenerate vibration only slightly affects the energy levels on complexation. In the ν_3 vibrational state ζ for Ar–CH$_4$ is about five times the value for ζ in the Ar–SiH$_4$ complex and the potential anisotropy is smaller. We would therefore not expect assignment of the Ar–CH$_4$ spectrum to be so straightforward.

The infrared spectrum of Ar–CH$_4$ in the vicinity of the CH$_4$ ν_3 band has been measured recently using both molecular beam [86,87] and equilibrium gas cell[85] techniques. All three spectra remain as yet unassigned and the subject was debated vigorously at the recent Faraday Discussion[102] in Durham. Significant discrepancies exist between the three spectra observed and much work remains to understand this complex.

Chapter 3: The Argon-Methane Complex

Chapter 4: Wavefunctions from Coupled Channel Calculations. Application to Ar-HF.

4.1 INTRODUCTION

Having studied the Ar–HCCH and Ar–CH$_4$ complexes, work was then begun on the Ar–C$_2$H$_4$ system. The energy level pattern obtained, however proved very difficult to rationalise, and it was decided to implement a method to extract wavefunctions from coupled channel calculations to help with their interpretation. A way to approach the problem had already been outlined[103] and the details are given here.

The distinguishing feature of the coupled-channel bound-state method is that it does *not* use a basis set for the radial coordinate R, but instead solves the coupled differential equations by direct numerical propagation. This eliminates difficulties associated with basis set convergence for the highly anharmonic R coordinate. In addition, the matrices that must be handled are no larger than $N \times N$, where N is the number of *angular* functions in the basis set. The coupled-channel method is capable of producing eigenvalues to very high precision, and has become the method of choice in fitting intermolecular potentials to high-resolution spectroscopic results.[104]

There are many numerical methods for propagating solutions of the coupled equations, most of which originated in molecular scattering theory. Methods based on propagating the log-derivative matrix[30] have become very popular for bound-state problems, because they are very stable even in the presence of deeply closed channels and offer good convergence with respect to the step size used.

One disadvantage of the log-derivative propagators has been that they do not provide explicit wavefunctions. To circumvent this, methods have been developed for calculating expectation values without requiring wavefunctions.[34] Nevertheless, wavefunctions are needed for calculating spectroscopic intensities and as a starting point for calculations of photodissociation processes and time-domain experiments. In addition, they are valuable in giving physical interpretations of the results of bound-state calculations. This chapter describes a method for obtaining wavefunctions from coupled-channel calculations that use log-derivative propagators. The method can be applied to any coupled-channel bound-state

Chapter 4: Wavefunctions from the Coupled Channel Method.

problem; we will demonstrate its capabilities by using it to calculate spectroscopic intensities for the Ar–HF complex.

4.2 THE LOG-DERIVATIVE PROPAGATOR

The coupled equations may be expressed in matrix notation,

$$\frac{d^2\psi}{dR^2} = [\mathbf{W}(R) - E\boldsymbol{I}]\psi(R), \tag{4.1}$$

where $\mathbf{W}(R)$ is an $N \times N$ matrix with elements $W_{ij}(R)$, $\boldsymbol{I}$ is the $N \times N$ unit matrix, and $\psi(R)$ is a column vector with components $\psi_{jn}(R)$.

In bound-state applications, the objective is to find the eigenvalues E_n and corresponding eigenfunctions $\psi_n(R)$ of the coupled equations, subject to the boundary conditions $\psi_{jn}(R) \rightarrow 0$ as $R \rightarrow 0$ or ∞ for all channels j. If the boundary conditions are applied at only one end of the range, there are N linearly independent solution vectors $\psi(R)$ that satisfy Eq. (4.1) for any energy. It is convenient to assemble the N column vectors to form an $N \times N$ wavefunction matrix $\Psi(R)$. For an arbitrary energy E, a solution matrix can be generated starting at either end of the range. However, unless E is an eigenvalue E_n, it is not possible to find a solution that satisfies the boundary conditions at *both* ends of the range. Equivalently, if two solutions are started at the ends of the range and propagated to a common central point R_{mid} then it will be possible to match both the solution and its derivatives at R_{mid} only if E is an eigenvalue.

The log-derivative matrix was first introduced by Johnson[30] and further detail on the derivation, and improvement and extension has been provided by Secrest and Mrugała,[105,106] and Manolopoulos and coworkers.[31,107,108]

The log-derivative matrix $\boldsymbol{Y}(R)$ is defined by

$$\boldsymbol{Y}(R) = \Psi'(R)\Psi^{-1}(R), \tag{4.2}$$

where the prime indicates radial differentiation. This matrix becomes undefined whenever the determinant of the wavefunction vanishes and these singularities prevent standard numerical integration techniques.

Several different methods of propagating the log-derivative matrix have been developed, and a useful discussion setting them in a common framework has been

Chapter 4: Wavefunctions from the Coupled Channel Method.

given by Manolopoulos.[108] The different methods may all be expressed in terms of a general imbedding propagator $\mathcal{Y}$ defined for an interval $[a, b]$ by[105]

$$\begin{bmatrix} \Psi'(a) \\ \Psi'(b) \end{bmatrix} = \begin{bmatrix} \mathcal{Y}_1(a, b) & \mathcal{Y}_2(a, b) \\ \mathcal{Y}_3(a, b) & \mathcal{Y}_4(a, b) \end{bmatrix} \begin{bmatrix} -\Psi(a) \\ \Psi(b) \end{bmatrix}, \tag{4.3}$$

where the quantities $\mathcal{Y}_n(a, b)$ are $N \times N$ matrices. A recursion relation for the log-derivative matrix can be obtained from (4.3),

$$Y(b) = \mathcal{Y}_4(a, b) - \mathcal{Y}_3(a, b)[Y(a) + \mathcal{Y}_1(a, b)]^{-1}\mathcal{Y}_2(a, b). \tag{4.4}$$

The integration range is partitioned into a series of small intervals or sectors, the propagator matrix $\mathcal{Y}$ is constructed for each sector and the log derivative matrix is propagated by recursive application of (4.4)

Numerical approximations to the log-derivative propagation matrices $\mathcal{Y}_n$ are obtained by choosing a reference potential $W^0(R)$, for which the propagator can be obtained exactly, and a quadrature method that is used in an integral equation scheme to handle the remainder of the potential. If a modified Simpson's rule is used for the quadrature, the resulting half-sector propagators are[108]

$$\mathcal{Y}_1(a, c) = \mathcal{Y}_1^0(a, c) + \frac{h}{3}W^1(a);$$

$$\mathcal{Y}_2(a, c) = \mathcal{Y}_2^0(a, c);$$

$$\mathcal{Y}_3(a, c) = \mathcal{Y}_3^0(a, c);$$

$$\mathcal{Y}_4(a, c) = \mathcal{Y}_4^0(a, c) + \frac{2h}{3}\widetilde{W}^1(c);$$

$$\mathcal{Y}_1(c, b) = \mathcal{Y}_1^0(c, b) + \frac{2h}{3}\widetilde{W}^1(c); \tag{4.5}$$

$$\mathcal{Y}_2(c, b) = \mathcal{Y}_2^0(c, b);$$

$$\mathcal{Y}_3(c, b) = \mathcal{Y}_3^0(c, b);$$

$$\mathcal{Y}_4(c, b) = \mathcal{Y}_4^0(c, b) + \frac{h}{3}W^1(b),$$

where $h = c - a = b - c$. The zeroth-order propagator blocks $\mathcal{Y}_n^0$ solve Eq. (4.3) exactly for $W^0(R)$, and

$$W^1(R) = W(R) - W^0(R)$$

$$\widetilde{W}^1(c) = \frac{6}{h^2}\left[I - \frac{h^2}{6}W^1(c)\right]^{-1} - \frac{6}{h^2}I. \tag{4.6}$$

Chapter 4: Wavefunctions from the Coupled Channel Method.

The choice $W^0(R) = EI$ corresponds to Johnson's original log-derivative propagator.[30] In this work, we have used the diabatic modified log-derivative propagator of Manolopoulos.[31] Here $W^0(R)$ in each segment is chosen to be the diagonal part of $W(c)$. The zeroth-order half-sector propagators are then diagonal matrices, with different diagonal elements in each channel j given by

$$
\begin{aligned}
\mathcal{Y}_1^0(a,c) = \mathcal{Y}_4^0(a,c) = \mathcal{Y}_1^0(c,b) = \mathcal{Y}_4^0(c,b) &= \begin{cases} |k_j| \coth |k_j| h, & k_j^2 \geq 0; \\ |k_j| \cot |k_j| h, & k_j^2 \leq 0; \end{cases} \\
\mathcal{Y}_2^0(a,c) = \mathcal{Y}_3^0(a,c) = \mathcal{Y}_2^0(c,b) = \mathcal{Y}_3^0(c,b) &= \begin{cases} |k_j| \operatorname{csch} |k_j| h, & k_j^2 \geq 0; \\ |k_j| \csc |k_j| h, & k_j^2 \leq 0; \end{cases}
\end{aligned} \tag{4.7}
$$

where $k_j^2 = W_{jj}(c) - E$ for the channel concerned.

In the log-derivative bound-state method, the log-derivative matrix is propagated outwards from a point at short range, $R_{\min}$, and inwards from a point at long range, $R_{\max}$, to a common matching point $R_{\mid}$. The trial energy E is an eigenvalue if there exists a wavefunction vector for which both the values and their derivatives match at $R_{\mid}$. Since the columns of Ψ are linearly independent, any wavefunction vector can be expressed as a linear combination of them. If the vector is $\psi(R_{\mid})$, the matching condition is $[\psi^+]'(R_{\mid}) = [\psi^-]'(R_{\mid})$, where the superscripts $+$ and $-$ refer to solutions obtained from the outwards and inwards propagations. The inwards and outwards derivatives may be written in terms of the inwards and outwards log-derivative matrices using the definition (4.2), so that the matching condition may be written

$$
Y^+(R_{\mid})\psi(R_{\mid}) = Y^-(R_{\mid})\psi(R_{\mid}) \tag{4.8}
$$

or

$$
Y_{\text{match}}\psi(R_{\mid}) = 0, \tag{4.9}
$$

where $Y_{\text{match}} = Y^+(R_{\mid}) - Y^-(R_{\mid})$.

Thus at an energy eigenvalue of the coupled equations, the matching matrix has (at least) one eigenvalue that is zero, and consequently has zero determinant. The usual strategy[23] used to find bound state energies from log-derivative coupled-channel calculations is to carry out calculations for a series of trial energies, and to search for energies at which the determinant is zero using standard algorithms such as the secant method.[109] An alternative approach, which has been found to be numerically more convenient because it is unaffected by poles in other eigenvalues, is to search for energies at which the smallest eigenvalue of the matching matrix is zero.[110]

Chapter 4: Wavefunctions from the Coupled Channel Method.

4.3 CALCULATION OF THE WAVEFUNCTION

Once an energy eigenvalue has been located, the matching condition

$$Y_{\text{match}}\psi(R_{\text{mid}}) = 0 \qquad (4.10)$$

shows that $\psi(R_{\text{mid}})$ is an eigenvector of the log-derivative matching matrix Y_{match} with eigenvalue zero.[103] Then, once an energy eigenvalue has been located, Eq. (4.10) provides the wavefunction at R_{mid}. It is then necessary to use the log-derivative propagation equations to determine $\psi(R)$ over the rest of the propagation range. The sector $[a, b]$ is divided into two half-sectors $[a, c]$ and $[c, b]$, with different expressions for the half-sector propagators $\mathcal{Y}_n$ in the two halves.

To obtain a propagation equation for the wavefunction, we begin with the first part of equation (4.3),

$$\Psi'(a) = -\mathcal{Y}_1(a, b)\Psi(a) + \mathcal{Y}_2(a, b)\Psi(b). \qquad (4.11)$$

Multiplying from the right by $\Psi(a)^{-1}$ and using the definition (4.2) gives after some rearrangement

$$\Psi(a) = [Y(a) + \mathcal{Y}_1(a, b)]^{-1}\mathcal{Y}_2(a, b)\Psi(b). \qquad (4.12)$$

The quantity $[Y(a) + \mathcal{Y}_1(a, b)]^{-1}\mathcal{Y}_2(a, b)$ for each half-sector is an $N \times N$ matrix that is already calculated in propagating the log-derivative matrix. Thus all that is needed to generate the wavefunction across the propagation range is to save the matrices during the propagation at the last energy, and read them back in reverse order to generate the wavefunction from $\psi(R_{\text{mid}})$ after convergence on the energy is achieved.

The method is completely general and can be applied to coupled channel problems of many different types. It has been implemented within the general purpose BOUND computer program[27] as an optional extra after an energy level has been converged. The final propagation loop is then repeated at the converged energy to save the necessary matrices and then back-substitution of the wavefunction from the midpoint is carried out. The resulting wavefunction is saved as a value in each angular channel function at a grid of R values. It is unnormalised but a normalisation factor is trivially calculated during the back-substitution and provided at the start of the storage file along with other parameters labelling the wavefunction.

Chapter 4: Wavefunctions from the Coupled Channel Method.

4.4 APPLICATION TO AR-HF.

In order to explore the capabilities of this new method the Ar-HF system was chosen as a test case that has been extensively studied and is well understood (Ref. 104 and references therein). The most recent potential available is the H6(4,3,2) potential of Hutson[104] which includes a dependence upon the vibrational state of the HF monomer. This potential was obtained by fitting to results from high resolution microwave, far infrared and infrared spectroscopy and reproduced all the spectroscopic data for levels of Ar–HF correlating with HF $v = 0, 1$ and 2 and DF $v = 0$ and 1 available at the time. It has since been tested by new experimental data[111-113] including spectra involving the Ar–HF $v = 3$ state.[114] This potential is believed to be very accurate and we anticipate any error arising in our calculations from this source to be only a few percent.

We have carried out both helicity decoupling and close-coupling calculations on Ar–HF, using the H6(4,3,2) potential. Separate calculations were carried out for levels correlating with HF in its $v = 0$, 1 and 3 states, including all basis functions involving HF rotor levels up to $j = 8$ in each case. The coupled equations were propagated over the range between $R_{\min} = 2.5$ Å and $R_{\max} = 9.0$ Å.

To produce plots of wavefunctions for energy levels of interest we use the helicity decoupling results which are calculated in the body-fixed representation. In body-fixed co-ordinates the basis functions for an atom-diatom system, assuming a particular monomer vibrational state, are

$$\Phi_{j\tau K}^{JM}(\alpha_R, \beta_R, \phi, \theta, \chi) = \left(\frac{2J+1}{4\pi}\right)^{\frac{1}{2}} \mathcal{D}_{MK}^{J*}(\alpha_R, \beta_R, 0) Y_{jK}(\theta, \phi). \qquad (4.13)$$

The wavefunction then simplifies from the general case (1.11) to;

$$\chi_\alpha^{JM}(R, \theta, \phi, \alpha, \beta) = R^{-1} \sum_{jK} \left(\frac{2J+1}{4\pi}\right)^{1/2} D_{MK}^{J*}(\alpha, \beta, 0) Y_{jK}(\theta, \phi) \psi_{jK}^{J\alpha}(R). \quad (4.14)$$

In the helicity decoupling approximation, off-diagonal Coriolis terms are neglected, so that the coupled equations become diagonal in K. The wavefunction is then

$$\chi_{K\alpha}^{JM}(R, \theta, \phi, \alpha, \beta) = R^{-1} \sum_j \left(\frac{2J+1}{4\pi}\right)^{1/2} D_{MK}^{J*}(\alpha, \beta, 0) Y_{jK}(\theta, \phi) \psi_{jK}^{J\alpha}(R). \quad (4.15)$$

Chapter 4: Wavefunctions from the Coupled Channel Method.

$D_{MK}^J(\alpha, \beta, 0)$ is a rotation matrix for the rotation of the whole complex into the space-fixed frame and factorises out of this expression. Plots of the internal wavefunction are thus produced from the expression

$$\frac{1}{\sqrt{N}} \sum_j \left(\frac{2J+1}{4\pi}\right)^{1/2} Y_{jK}(\theta, \phi) \psi_{jK}^{J\alpha}(R), \qquad (4.16)$$

where the factor of R^{-1} has been dropped as it would cancel with the R^2 in the volume element during the calculation of probabilities and N is a normalisation factor. Wavefunctions, obtained from the helicity decoupling calculations for the $v = 1$ state, are shown in Fig.4.i, as functions of the intermolecular distance R and bending angle θ, measured with respect to the HF centre of mass. The states can be described in terms of labels $(vbKn)$, where b is a bending quantum number that correlates in the isotropic limit with the diatom rotational quantum number j, K is the projection of j onto the intermolecular axis, and n is the quantum number for the Van der Waals stretch. As expected, the Van der Waals ground-state (1000) wavefunction is concentrated around the potential minimum at $\theta = 0$ (the linear Ar–H-F geometry), but shows wide-amplitude bending motion, with substantial amplitude out to beyond $\theta = 90°$. The Π bend excited state (1110) is concentrated around $\theta = 60°$, while the Σ bend excited state (1100) is concentrated around $\theta = 0$ and $180°$, with rather greater amplitude at $\theta = 180°$.

The helicity decoupled wavefunctions were also used to calculate expectation values of $\langle P_2(\cos\theta) \rangle$ and $\langle 1/R^2 \rangle$. The form of the basis set assisted in simplifying the calculation as the rotation matrices which depend on α, β only, factorise out and integrate to one. The values were in excellent agreement with expectation values calculated by the finite difference method of Hutson[34] for the same propagation conditions. A plot of $\ln(\langle 1/R^2 \rangle - 0.081117)$ vs $\ln H$, H being the stepsize, Fig. 4.ii, has a gradient of 2.8 ± 0.6 indicating that the convergence of the expectation value is proportional to H^3.

We have also carried out space-fixed close-coupling calculations of wavefunctions for the lowest 5 Van der Waals vibrational levels of Ar–HF for total angular momenta up to $J = 20$, and used them to calculate intensities for infrared bands in the HF fundamental and second overtone ($v = 3 \leftarrow 0$) regions, assuming a jet temperature of 10 K. Frequencies were calculated using experimental HF monomer frequencies of 3961.4229 cm^{-1} for $v = 1 \leftarrow 0$[115] and 11372.807 cm^{-1} for $v = 3 \leftarrow 0$.[116]

*Chapter 4: Wavefunctions from the Coupled Channel Method.*
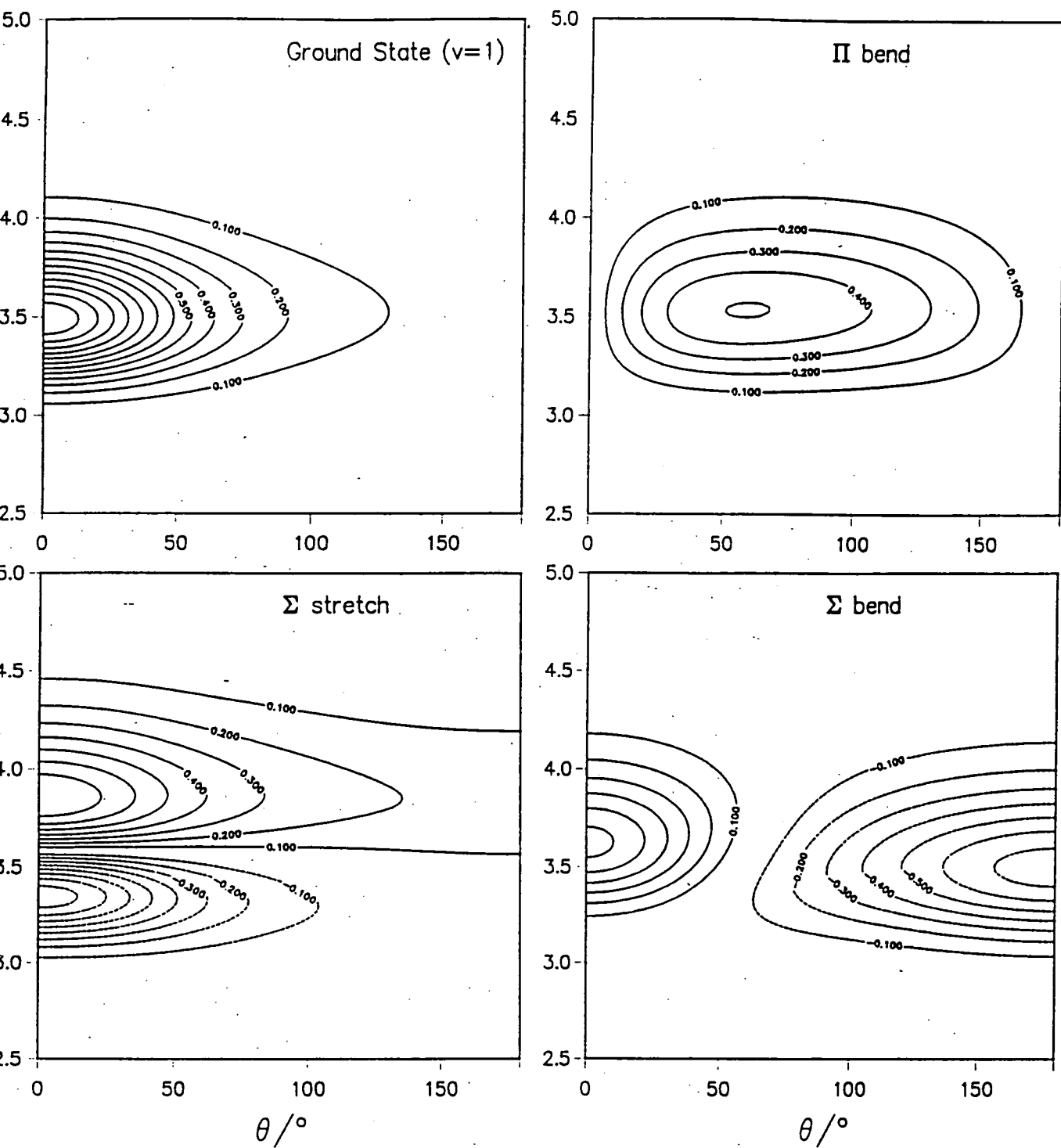
Fig. 4.i Contour plots of the wavefunctions for $v = 1$ states of Ar–HF.

*Chapter 4: Wavefunctions from the Coupled Channel Method.*
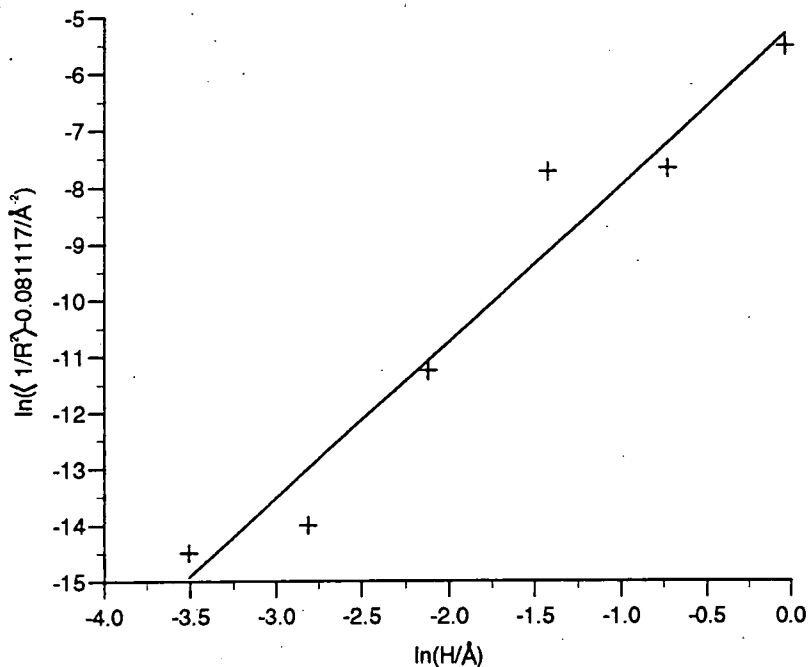
Fig. 4.ii Plot indicating the dependence of the convergence of $\langle 1/R^2 \rangle$ on the Stepsize H.

The space-fixed angular basis set for an atom-diatom system is

$$\varphi_{jL}^{JM}(\hat{R},\hat{r}) = \sum_{m_j m_L} \langle jLm_jm_L|JM\rangle\, Y_{Lm_L}(\beta_R,\alpha_R)Y_{jm_j}(\alpha_r,\beta_r). \qquad (4.17)$$

As these functions form a complete angular basis set it is convenient to expand the components of the dipole moment function in terms of them,[15,29,117]

$$\mu_M(\hat{R},\hat{r}) = \sum_{jL} \mu_{jL}^{SF}(R,r)\varphi_{jL}^{1M}(\hat{R},\hat{r}), \qquad (4.18)$$

where SF denotes space-fixed, $J = 1$ as μ must transform as a vector with respect to rotations of the space-fixed axes and $(j + L)$ is odd as the dipole moment function has odd parity.

The symmetries of dipole moment contributions that can occur in atom-diatom Van der Waals molecules are given in table 4.I.[15]

From the Wigner-Eckart theorem,[15] the matrix elements of these expansion

Chapter 4: Wavefunctions from the Coupled Channel Method.

Origin	j	L	J
Direct dipole moment of diatom	1	0	1
Charge-induced dipole	0	1	1
Dipole-induced dipole	1	2	1
Quadrupole-induced dipole	2	3	1

Table 4.I Symmetries of dipole moment contributions in atom–diatom Van der Waals molecules.

functions between space-fixed basis functions are

$$(j_i L_i J_i M_i | \varphi_{jL}^{1M} | j_f L_f J_f M_f)$$

$$= (-)^{j_i+L_i+J_i+M_i} \begin{pmatrix} J_i & 1 & J_f \\ -M_i & M & M_f \end{pmatrix}$$

$$\times [3(2J_i+1)(2J_f+1)(2j_i+1)(2j_f+1)(2L_i+1)(2L_f+1)]^{\frac{1}{2}}$$

$$\times \begin{pmatrix} j_i & j & j_f \\ 0 & 0 & 0 \end{pmatrix} \begin{pmatrix} L_i & L & L_f \\ 0 & 0 & 0 \end{pmatrix} \begin{Bmatrix} J_i & J_f & 1 \\ j_i & j_f & j \\ L_i & L_f & L \end{Bmatrix},$$

$$(4.19)$$

where $(j_i L_i J_i M_i | \varphi_{jL}^{1M} | j_f L_f J_f M_f)$ indicates the integral over *all* angular variables and the right-hand side contains three Wigner 3-j and one 9-j symbols. All terms dependent on projection quantum numbers M, M_i and M_f may be factorised out of the RHS of equation (4.19). We require the sum of squares over *all* such components, and, using the orthogonality properties of Wigner 3-j symbols[118] the sum over the squares of the 3-j symbols containing M evaluates to 1. It is therefore sufficient to evaluate reduced rotation matrix elements defined by

$$(i | \varphi_{jL}^1 | f) = (-)^{j_i+L_i+J_i}$$

$$\times [3(2J_i+1)(2J_f+1)(2j_i+1)(2j_f+1)(2L_i+1)(2L_f+1)]^{\frac{1}{2}}$$

$$\times \begin{pmatrix} j_i & 1 & j_f \\ 0 & 0 & 0 \end{pmatrix} \begin{pmatrix} L_i & 0 & L_f \\ 0 & 0 & 0 \end{pmatrix} \begin{Bmatrix} J_i & J_f & 1 \\ j_i & j_f & 1 \\ l_i & l_f & 0 \end{Bmatrix},$$

$$(4.20)$$

where i and f are shorthand for $j_i L_i J_i$ and $j_f L_f J_f$ respectively.

Two different methods were used to evaluate the transition dipole for the complex. The first assumes that the only contribution to the transition dipole

Chapter 4: Wavefunctions from the Coupled Channel Method.

originates from the transition dipole of the HF monomer. Thus,

$$\int \Phi_{j_i v_i L_i}^{J_i M_i *} \mu_M \Phi_{j_f v_f L_f}^{J_f M_f} d\tau = \langle v_i | \mu_{10}(R, r) | v_f \rangle (i | \varphi_{10}^1(\hat{R}, \hat{r}) | f), \qquad (4.21)$$

where $M = M_f - M_i$, the v_i and v_f denote the vibrational wavefunction and Φ_{jvL}^{JM} the space-fixed basis functions.

A second approximation to the dipole moment was also made by including additional terms for the dipole-induced dipole and quadrupole-induced dipole terms.

$$\int \Phi_{j_i v_i L_i}^{J_i M_i *} \mu_M \Phi_{j_f v_f L_f}^{J_f M_f} d\tau$$
$$= \langle v_i | \mu_{10} | v_f \rangle (i | \varphi_{10}^1 | f) + \langle v_i | \mu_{12} | v_f \rangle (i | \varphi_{12}^1 | f) + \langle v_i | \mu_{23} | v_f \rangle (i | \varphi_{23}^1 | f).$$
$$(4.22)$$

Poll and Hunt[119] give an expression for the multipolar induction contribution to the dipole,

$$\mu_{jL}(r, R) = \alpha \sqrt{j + 1} \frac{\langle v J | Q_j | v' J' \rangle}{R^{j+2}}, \qquad (4.23)$$

where α is the polarisability of the atom and $\langle v J | Q_\lambda | v' J' \rangle$ is the vibrational matrix element of the multipole moment $Q_\lambda(r)$ of the diatomic molecule. Thus

$$\mu_{12} = \frac{\sqrt{2}\alpha \langle v J | \mu_{\mathrm{HF}}(r) | v' J' \rangle}{R^3}$$
$$\mu_{23} = \frac{\sqrt{3}\alpha \langle v J | \Theta_{\mathrm{HF}}(r) | v' J' \rangle}{R^4} \qquad (4.24)$$

are the expressions for the dipole-induced dipole and quadrupole-induced dipole terms in atomic units, with Θ_{HF} denoting the quadrupole moment of the molecule.[120] Substituting these expression in equation (4.22) and factorising out the HF monomer transition dipole leaves,

$$\int \Phi_{j_i v_i L_i}^{J_i M_i *} \mu_M \Phi_{j_f v_f L_f}^{J_f M_f} d\tau = \langle v_i | \mu_{\mathrm{HF}}(r) | v_f \rangle \left\{ (i | \varphi_{10}^1 | f) + (i | \frac{\sqrt{2}}{R^3} \alpha \varphi_{12}^1 | f) \right.$$
$$\left. + (i | \frac{\sqrt{3}}{R^4} \alpha \varphi_{23}^1 | f) \left[\frac{\langle v_i | \Theta_{\mathrm{HF}}(r) | v_f \rangle}{\langle v_i | \mu_{\mathrm{HF}}(r) | v_f \rangle} \right] \right\}. \qquad (4.25)$$

By expanding the expression $\mu_{\mathrm{HF}}(r)$ as a Taylor series about $r = r_e$ we get,

$$\langle v_i | \mu_{\mathrm{HF}}(r) | v_f \rangle = \langle v_i | \mu(r_e) + \frac{d\mu}{dr} \Big|_{r_e} (r - r_e) + \frac{1}{2} \frac{d^2\mu}{dr^2} \Big|_{r_e} (r - r_e)^2 + \dots | v_f \rangle. \quad (4.26)$$

Chapter 4: Wavefunctions from the Coupled Channel Method.

By assuming the HF monomer behaves as a harmonic oscillator and neglecting the j dependence of the matrix elements $\langle v_i | \mu_{\text{HF}}(r) | v_f \rangle$ it is possible to use the expressions for harmonic oscillator matrix elements provided by Wilson, Decius and Cross[121] for a $v = 1 \leftarrow 0$ transition,

$$\langle 0 | (r - r_e) | 1 \rangle = \left(\frac{h}{8\pi^2 \nu} \right)^{1/2}, \tag{4.27}$$

where m is the reduced mass of the oscillator.

Making a similar expansion for Θ and assuming that terms above the linear in the Taylor expansion are negligible, we obtain the approximation;

$$\left[\frac{\langle v_i | \Theta_{\text{HF}}(r) | v_f \rangle}{\langle v_i | \mu_{\text{HF}}(r) | v_f \rangle} \right] = \left[\frac{\frac{d\Theta}{dr} |_{r_e}}{\frac{d\mu}{dr} |_{r_e}} \right]. \tag{4.28}$$

Liu and Dykstra[122] give values for the dipole and quadrupole moments for HF at three r values close to the equilibrium distance obtained from coupled cluster calculations. Assuming the moments vary linearly with r we calculate $\frac{d\mu}{dr}(r_e) = -1.53 \ \text{D\AA}^{-1}$ and $\frac{d\Theta}{dr}(r_e) = 4.1 \ \text{D}$ which are used in equation 4.28 in the intensity calculation. The Ar polarisability, $\alpha = 1.64626 \ \text{\AA}^3$, was taken from ab initio calculations by Reinsch and Meyer.[123] In this approximation the complete equation for the intensity becomes,

$$\int \chi_{v_i}^{J_i M_i \alpha_i *} \mu_M \chi_{v_f}^{J_f M_f \alpha_f} d\tau = \sum_{jL} \int \left\{ \langle 0 | \mu_{\text{HF}}(r) | 1 \rangle \left\{ (i | \varphi_{10}^1 | f) + \sqrt{2} \alpha (i | \frac{\varphi_{12}^1}{R^3} | f) \right. \right.$$
$$\left. \left. + \sqrt{3} (i | \frac{\varphi_{23}^1}{R^4} | f) \alpha \left[-\frac{4.1}{1.53} \text{\AA} \right] \right\} \right\} \psi_{j_i v_i M_i}^{J_i \alpha_i} \psi_{j_f v_i M_f}^{J_f \alpha_f} dR. \tag{4.29}$$

The results for the HF fundamental and its combination bands are shown in Figs.4.iii-4.vii. The fundamental bands were scaled so that the intensity in the R(5) line matched that of the experimental results for each dipole approximation. The same scaling factor (for each model of the dipole moment) was then applied to all the combination bands.

It may be seen in the figures that the calculated and experimental intensity distributions within each band agree very well, including the perturbation around $J = 7$ in the Π bend, which results from a heterogeneous perturbation involving the $n = 2$ stretching state. The relative intensities of the different bands, on the other hand, disagree by factors of up to 2 or 3: the Σ stretch is significantly more

Chapter 4: Wavefunctions from the Coupled Channel Method.
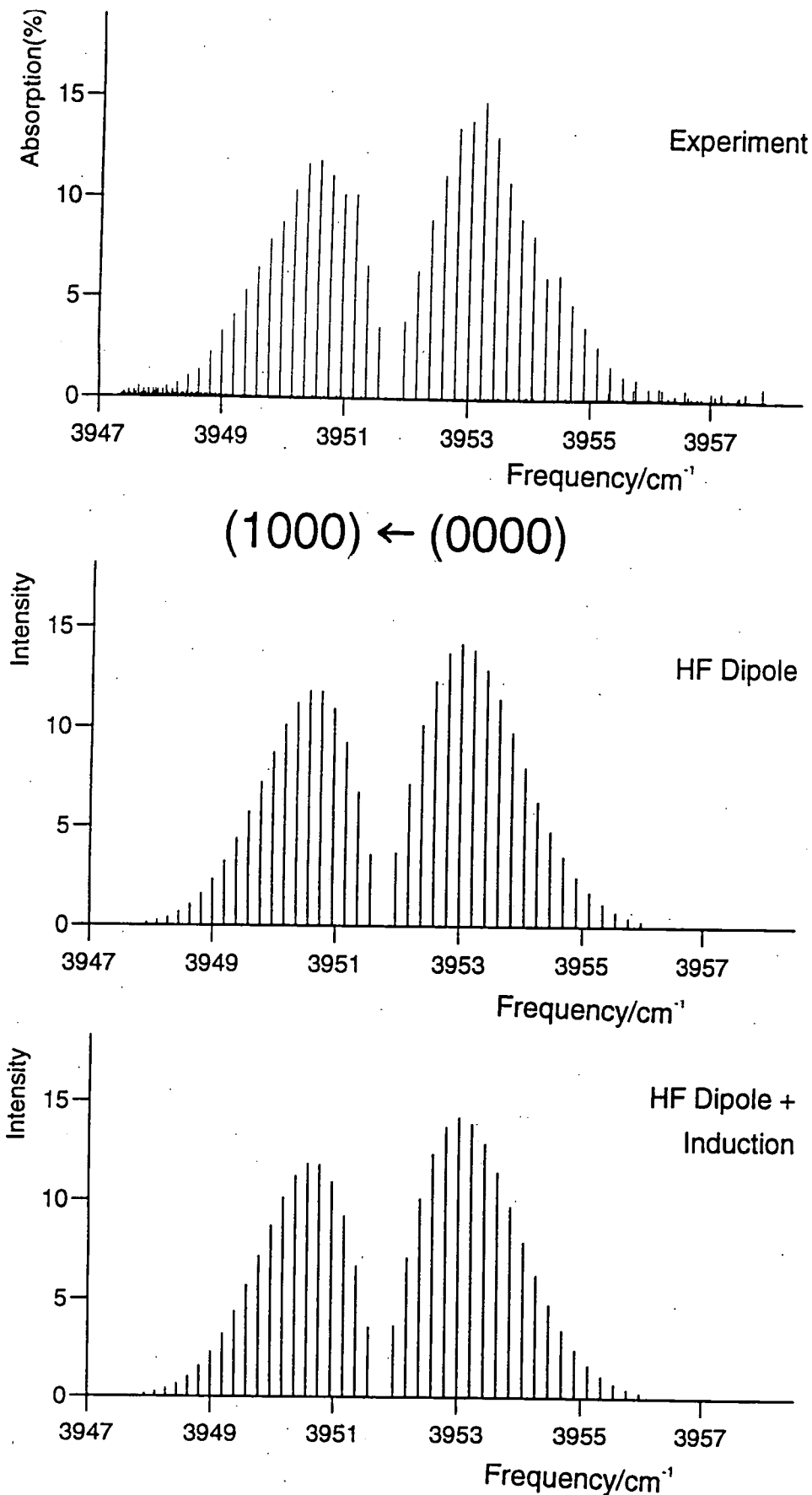
Fig. 4.iii Comparison of experimental and calculated spectra for the 1000 ← 0000 band of Ar-HF. The calculated intensities are scaled to reproduce the experimental peak intensity.

Chapter 4: Wavefunctions from the Coupled Channel Method.
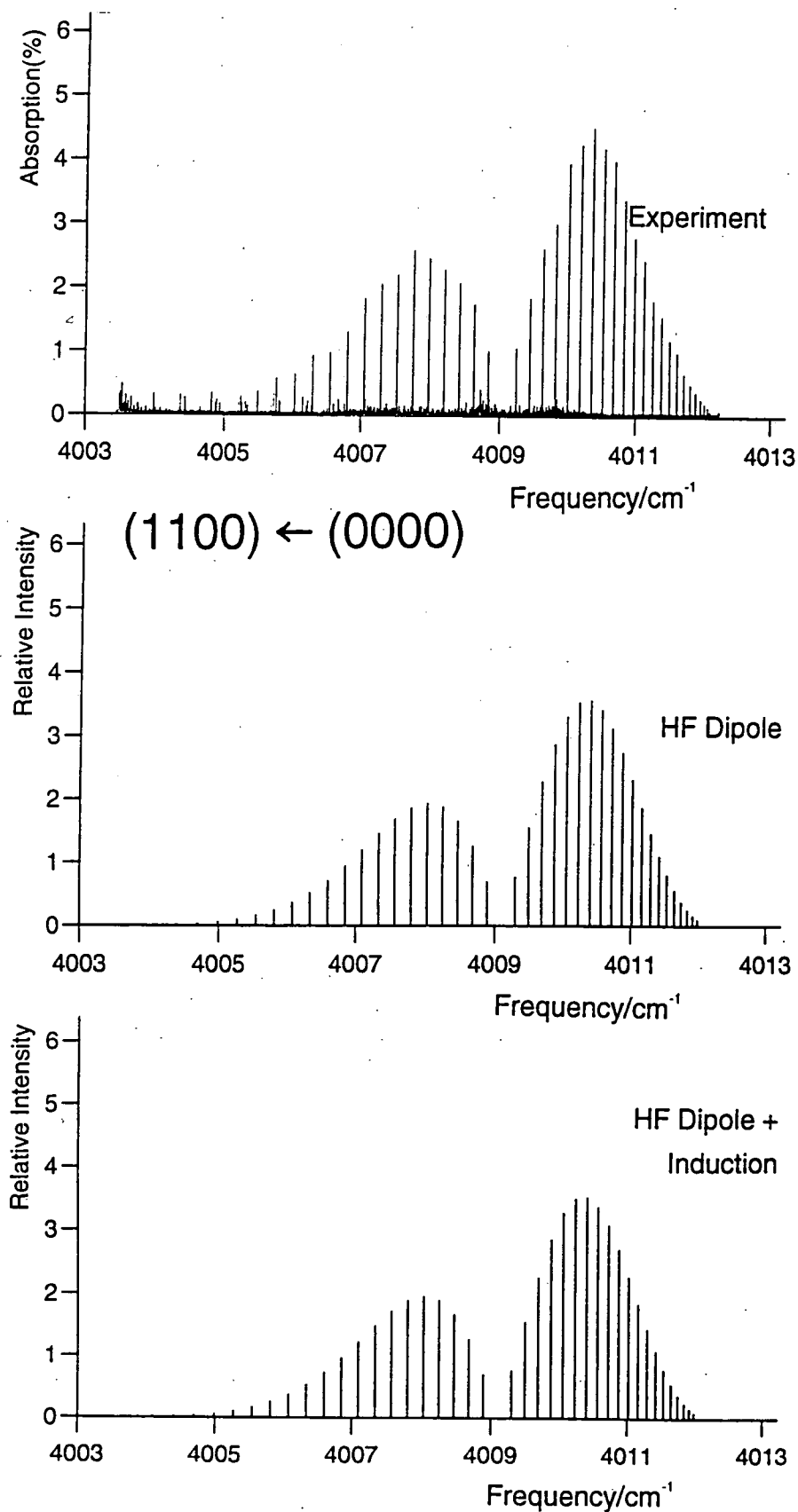
Fig. 4.iv Comparison of experimental and calculated spectra for the 1100 ← 0000 band of Ar-HF. The calculated intensities are scaled (with a single overall scaling factor for all bands) to reproduce the experimental peak intensity for the 1000 ← 0000 band.

Chapter 4: Wavefunctions from the Coupled Channel Method.
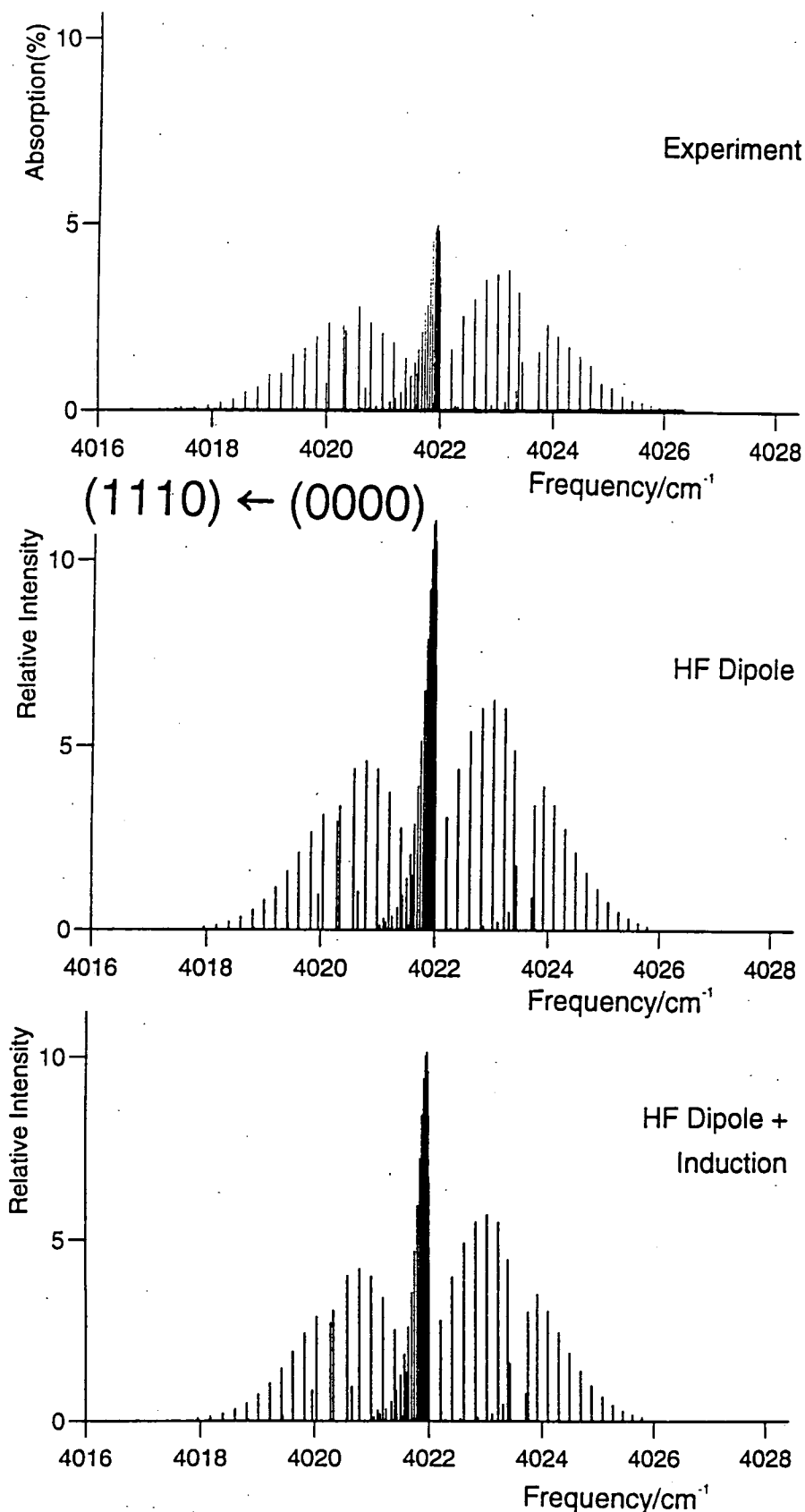
Fig. 4.v Comparison of experimental and calculated spectra for the 1110 ←
0000 band of Ar-HF. The calculated intensities are scaled (with a single overall
scaling factor for all bands) to reproduce the experimental peak intensity for the
1000 ← 0000 band.

Chapter 4: Wavefunctions from the Coupled Channel Method.
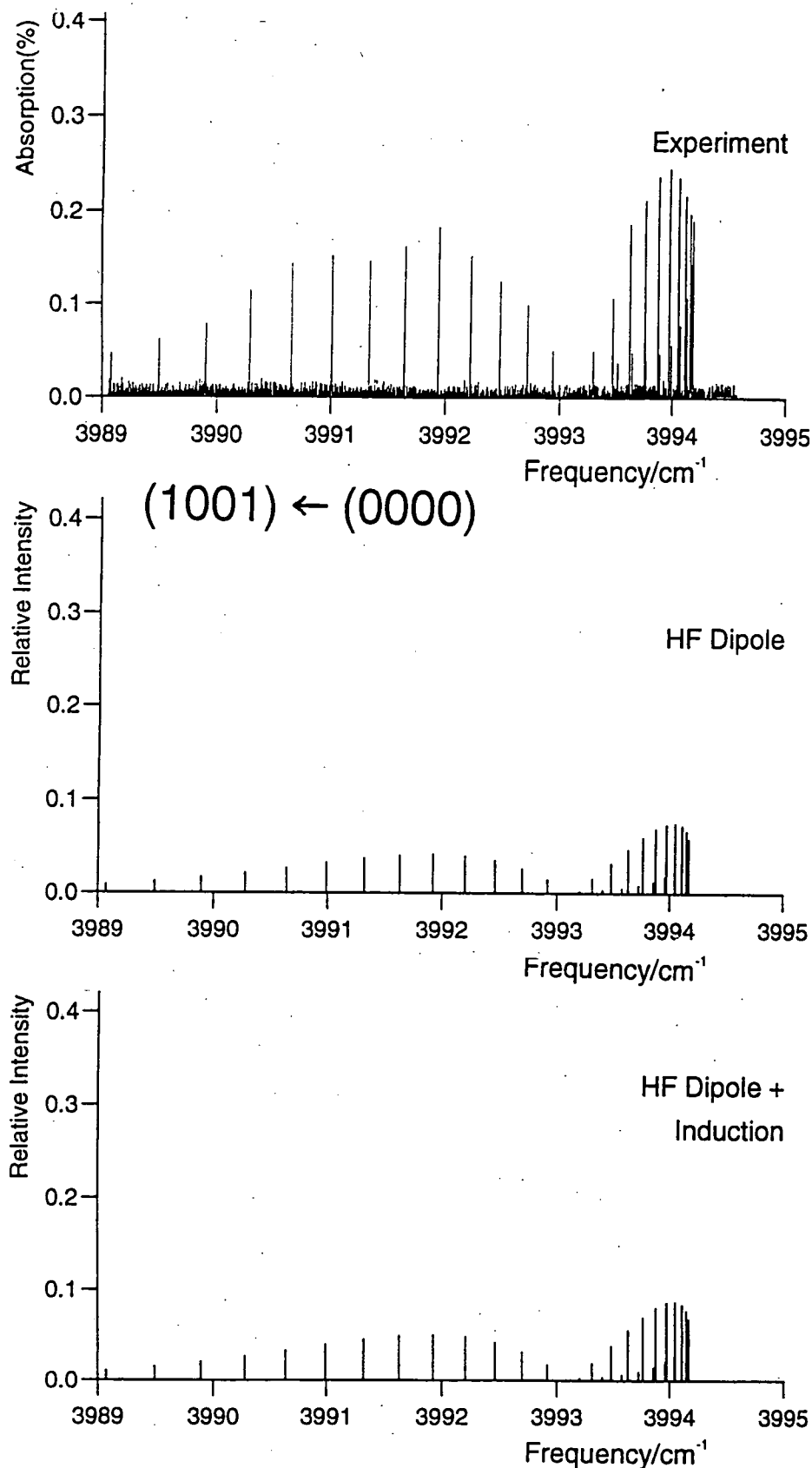
Fig. 4.vi Comparison of experimental and calculated spectra for the 1001 ←
0000 band of Ar-HF. The calculated intensities are scaled (with a single overall
scaling factor for all bands) to reproduce the experimental peak intensity for the
1000 ← 0000 band.

*Chapter 4: Wavefunctions from the Coupled Channel Method.*

intense experimentally than in the calculations, while the reverse is observed for the II bend. The discrepancies are far too large to be attributed to uncertainties in the intermolecular potential, and must be attributed to deficiencies in the model that we have used for the transition dipole. The dipole-induced dipole and quadrupole-induced dipole terms alter the intensities by up to 35%; the changes to the relative intensities are in the right direction, but are not nearly large enough to remove the discrepancy between the experimental and calculated intensities.

There is an interesting anomaly in the experimental results: the Van der Waals stretching combination band has 1.67% of the intensity of the fundamental for $v = 1 \leftarrow 0$,[124] but could not be observed for $v = 3 \leftarrow 0$,[114] suggesting that in the latter case its intensity was less than 1% of that of the 3000 $\leftarrow$ 0000 band.

For the $v = 3 \leftarrow 0$ bands, not enough is known about the dependence of the HF quadrupole on the HF bond length to allow the quadrupole-induced dipole term to be included. The calculations were therefore carried out using only the transition dipole of the HF monomer. The intensities of the Σ and II bending combination bands (relative to the 3000 $\leftarrow$ 0000 band) are similar to those for $v = 1 \leftarrow 0$ (though the perturbation due to the $n = 2$ state does not occur for the 3110 $\leftarrow$ 0000 band). However, the stretching combination band, 3001 $\leftarrow$ 0000, is substantially less intense: its peak intensity is only 0.1% of that of the 3000 $\leftarrow$ 0000 band. In the same approximation, the peak intensity of the 1001 $\leftarrow$ 0000 band is 0.5% of that of the 1000 $\leftarrow$ 0000 band. In addition, the band shape is quite different, as shown in Fig.4.viii: the peak intensity is in the R branch for the 1001 $\leftarrow$ 0000 band, but in the P branch for the 3001 $\leftarrow$ 0000 band.

The reduced relative intensity of the Van der Waals stretch for $v = 3$ agrees with experiment,[114] but is at first sight surprising. The explanation for it lies in fact that, for $v = 3$, the Σ bend and Σ stretch levels lie 26 cm^{-1} apart, whereas for $v = 1$ they are only 13.4 cm^{-1} apart. As a consequence, the bend and stretch levels are much more strongly mixed for $v = 1$, and the 1001 $\leftarrow$ 0000 band borrows considerable intensity from the much stronger 1100 $\leftarrow$ 0000 band. The different degree of mixing can be seen in the wavefunctions for the Van der Waals stretch states, which are shown in Fig.4.ix: the 1001 state has considerable amplitude around $\theta = 180°$, due to mixing with the 1100 state, whereas the 3001 state has much less amplitude in this region.

Chapter 4: Wavefunctions from the Coupled Channel Method.
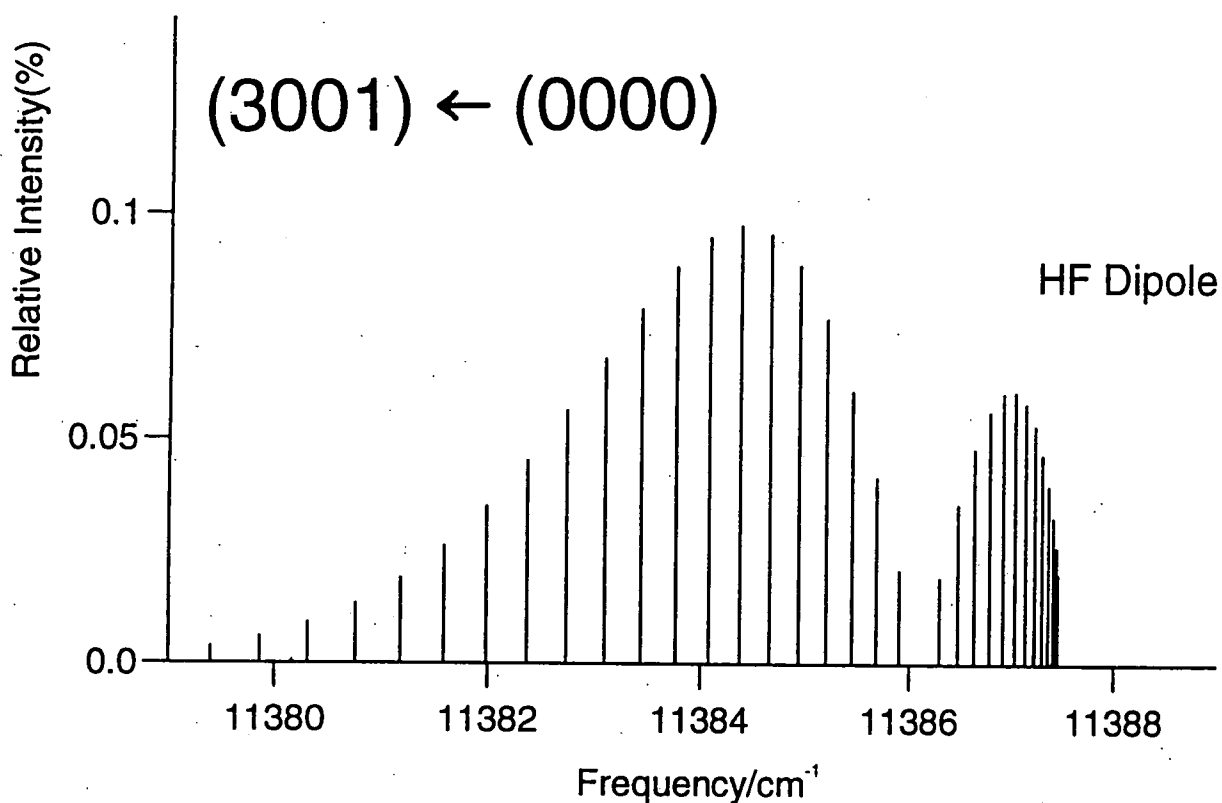
Fig. 4.vii Calculated spectrum of the 3001 ← 0000 bands of Ar-HF. The calculated intensities are given as a fraction of the calculated peak intensity for the 3000 ← 0000 band . Note that this is *not* the same scaling as in Figs. 4.iii-4.vi.

Chapter 4: Wavefunctions from the Coupled Channel Method.
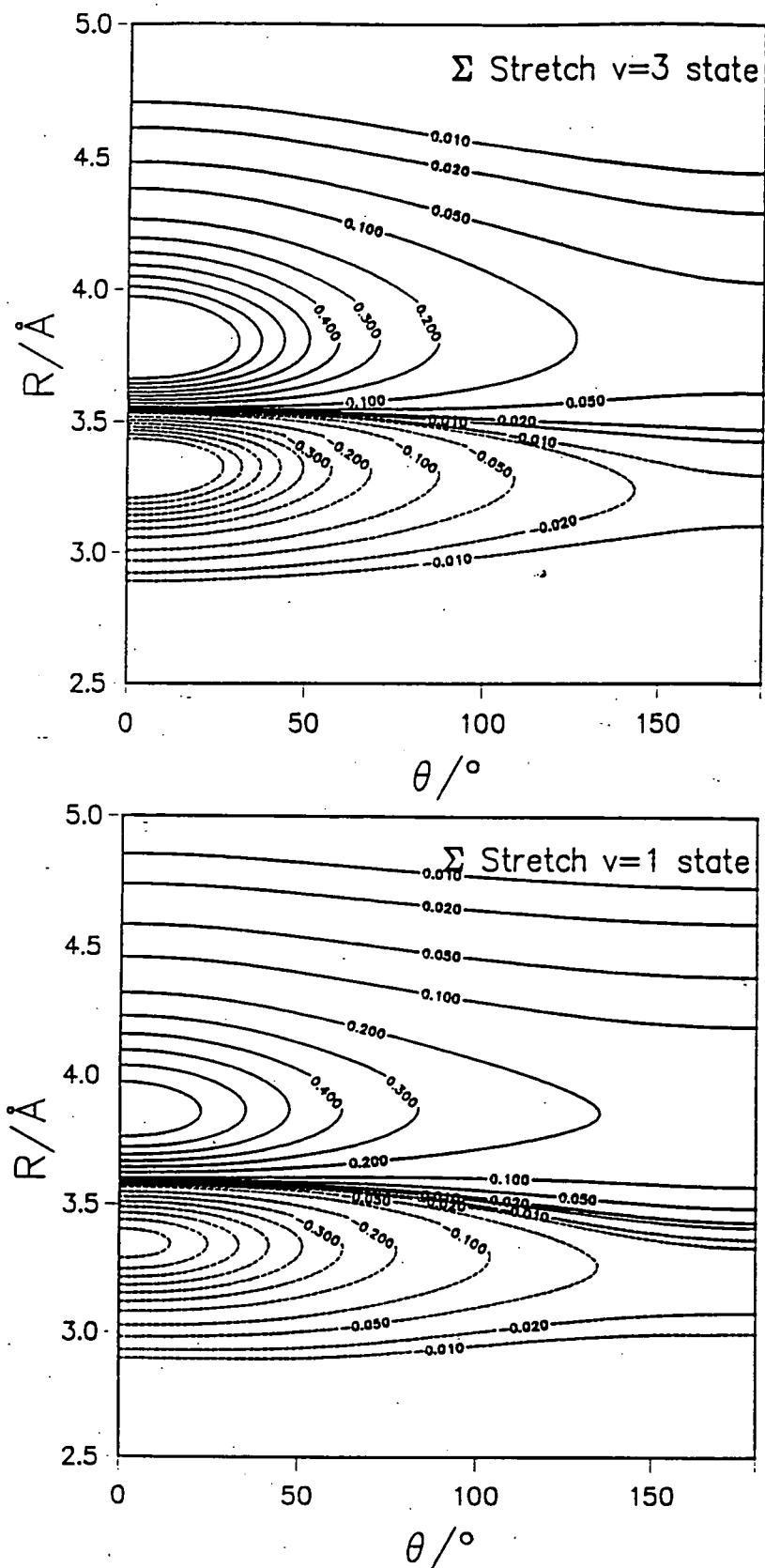
Fig. 4.viii Contour plots of the wavefunctions for the Van der Waals stretching states of Ar-HF for $v = 1$ and 3, from helicity decoupling calculations.

Chapter 4: Wavefunctions from the Coupled Channel Method.

It thus appears that it is the stretching combination band for $v = 1$, $1001 \leftarrow 0000$, which has an anomalously high intensity. This was first pointed out by Lovejoy and Nesbitt,[124] who carried out intensity calculations using simple product wavefunctions. They obtained a calculated intensity a factor of 30 smaller than experiment. Our more elaborate calculations give a substantially larger intensity, but are still a factor of more than 2 too low. This can probably be attributed to additional terms in the dipole moment function that we have neglected. In particular, overlap effects at short range may cause a substantial enhancement of the total transition dipole for the complex, and it is possible that these are responsible for the remainder of the anomalously high intensity of the $1001 \leftarrow 0000$ band.

4.5 CONCLUSIONS.

We have developed a method for calculating wavefunctions from bound-state calculations using the log-derivative coupled-channel method. The wavefunction at the central matching point is the eigenvector of the log-derivative matching matrix corresponding to eigenvalue zero. Once the wavefunction at this point has been determined, it is straightforward to propagate it over the remainder of the radial range, using information stored from the propagation of the log-derivative matrix. The method is completely general, and can be applied to coupled channel problems of many different types.

For demonstration purposes, we have applied the new method to calculating wavefunctions and spectroscopic intensities for infrared bands of the Ar–HF Van der Waals complex, using the H6(4,3,2) potential. The calculations give intensity distributions within bands in excellent agreement with experimental results. In addition, they explain the surprising difference between the observed intensities of the Van der Waals stretch combination bands for $v = 1$ and 3.

Chapter 4: Wavefunctions from the Coupled Channel Method.

Chapter 5: THE HELIUM–CARBON DIOXIDE SYSTEM

5.1 INTRODUCTION

The He–CO_2 system has attracted much attention from experimentalists[125−132] and theoreticians.[130,133−147] Apart from the recent work of Weida et al.[132] all data has been from either scattering or bulk gas experiments. Much of the theoretical work[130,139,140,142,144] has been directed towards understanding vibrational relaxation rates in this system to help explain the role of He in CO_2 lasers. Other rare gas–CO_2 systems are also of interest and have been studied in scattering,[148−153] bulk gas,[154] vibrational predissociation [155,156] and spectroscopic[157−161] experiments as well as theoretically.[133−136,138−140,143,162−169] A greater understanding of the He–CO_2 system should provide information on the trends in intermolecular properties with increasing rare gas size.

Two potential energy surfaces for He–CO_2 have been developed by fitting to experimental data,[127,131] and subsequent tests of these potentials[145,146] suggest that the work of Beneventi et al.[131] comes closest to the true potential. This potential is hereafter referred to as the Beneventi potential.

Very recently Weida et al.[132] have measured high resolution IR spectra of He–CO_2 in the region of the CO_2 ν_3 asymmetric stretch which is labelled ν_4 in the complex. Although it was possible to fit their data to a T-shaped asymmetric rotor Hamiltonian the fit was not particularly good and a large inertial defect was observed as would be expected from such a floppy molecule. Calculations on the Beneventi potential by the close coupling method implemented in BOUND[27] verified the flexible but localised T-shaped geometry for the ground vibrational state. The potential was found to predict even more non-rigid behaviour than was observed and was substantially too isotropic about the minimum. Some additional weak transitions centered about the origin of the ν_4 fundamental were attributed to a "hot band" excitation out of the first intermolecular bending level (ν_5) lying about 9 cm^{-1} above the ground state. However, despite using a 2D variational method with the Beneventi potential to calculate wavefunctions and intensities it was not possible to make a definite rotational assignment of the ν_5 hot band. A plot of the wavefunction for the ν_5 levels from the Beneventi potential showed that it was highly delocalised thwarting an attempt at a rigid rotor analysis.

An assignment of the observed ν_5 hot band transitions is highly desirable as they will yield information on the potential energy surface away from the minimum. An explanation is also sought for the failure to observe the $\nu_4 + \nu_5$ combination band which was predicted to be observable by the variational analysis using the Beneventi potential.

This chapter will address these questions by using a variation of the Beneventi potential, using the same functional form but modified to give better agreement with the ground state energy levels, with the new wavefunction capability of the BOUND[27] code to predict the spectrum.

5.2 POTENTIAL

The coordinate system for He–CO_2 is identical to that for Ar–acetylene presented in chapter 2. This system is illustrated in figure 5.i which also identifies the ν_4 and ν_5 vibrational modes.
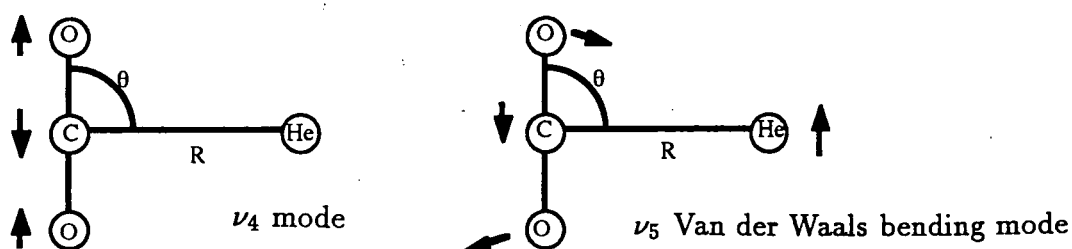
Fig. 5.i He–CO_2 ν_4 and ν_5 vibrational modes.

The Beneventi potential has an exponential-spline-Morse-Morse-spline-Van

Chapter 5: The Helium–Carbon Dioxide System

der Waals (ESMMSV) functional form. At each angle,

$$
\begin{aligned}
\dot{V}(R, \theta) &= \exp(A - \alpha R), & R &\le R_1, \\
&= \exp[a_1 + (R - R_1)(a_2 + (R - R_2)(a_3 + (R - R_1)a_4))], & R_1 &\le R \le R_2, \\
&= \epsilon'\{\exp[2\beta'(1 - R/R'_m)] - 2\exp[\beta'(1 - R/R'_m)]\}, & R_2 &\le R \le R_3, \\
&= \epsilon\{\exp[2\beta(1 - R/R_m)] - 2\exp[\beta(1 - R/R_m)]\}, & R_3 &\le R \le R_4, \\
&= b_1 + (R - R_4)\{b_2 + (R - R_5)[b_3 + (R - R_4)b_4]\} & R_4 &\le R \le R_5, \\
&= -C_6 R^{-6} - C_8 R^{-8} - C_{10} R^{-10}, & R_5 &< R < \infty,
\end{aligned}
\tag{5.1}
$$

Here the repulsive parameters A and α are expanded

$$
\begin{aligned}
A(\theta) &= A_0 + A_2 P_2(\cos\theta) + A_4 P_4(\cos\theta), \\
\alpha(\theta) &= \alpha_0 + \alpha_2 P_2(\cos\theta) + \alpha_4 P_4(\cos\theta),
\end{aligned}
\tag{5.2}
$$

and the long-range C_6 and C_8 similarly,

$$
\begin{aligned}
C_6(\theta) &= C_{6,0} + C_{6,2} P_2(\cos\theta), \\
C_8(\theta) &= C_{8,0} + C_{8,2} P_2(\cos\theta).
\end{aligned}
\tag{5.3}
$$

The angle-dependent minimum parameters are given by

$$
\begin{aligned}
\epsilon(\theta) &= \exp[\epsilon_0 + \epsilon_2 P_2(\cos\theta)], \\
R_m(\theta) &= R_{m0} + R_{m2} P_2(\cos\theta).
\end{aligned}
\tag{5.4}
$$

The parameters that define the Beneventi potential are given in table 5.I , and the formulae for joining points and spline parameters in table 5.II .

The Beneventi potential was originally fitted to total differential cross sections, differential energy loss spectra, low temperature second virial coefficients, diffusion and viscosity data by adjusting $\epsilon_0, \epsilon_2, R_{m0}, R_{m2}, \beta$ and β'. The work of Weida et al.[132] found this potential to be too isotropic about the potential minimum as is illustrated by a calculated bending frequency of 5.9 cm^{-1} compared to the experimental value of 9±2 cm^{-1}. In a rough, first step fit to the spectroscopic data from the ν_4 transition Hutson[170] has found that a value of $\epsilon_2 = -1.0$ ln(meV) which effectively increases the anisotropy improves the fit

Chapter 5: The Helium–Carbon Dioxide System

$\epsilon_0/\ln(\mathrm{meV})$	1.3083
$\epsilon_2/\ln(\mathrm{meV})$	−0.6358
$R_{m0}/\mathrm{\AA}$	3.68
$R_{m2}/\mathrm{\AA}$	1.07
β	6.0
β'	6.0
$A_0/\ln(\mathrm{meV})$	14.861
$A_2/\ln(\mathrm{meV})$	3.2667
$A_4/\ln(\mathrm{meV})$	0.8543
$\alpha_0/\mathrm{\AA}^{-1}$	3.7333
$\alpha_2/\mathrm{\AA}^{-1}$	0.12453
$\alpha_4/\mathrm{\AA}^{-1}$	0.41616
$C_{6,0}/\mathrm{meV\AA}^6$	9980
$C_{6,2}/\mathrm{meV\AA}^6$	2310
$C_{8,0}/\mathrm{meV\AA}^6$	46400
$C_{8,2}/\mathrm{meV\AA}^6$	48400

Table 5.I Potential Parameters for the Beneventi Potential.

$$R_1 = [A(\theta) - \ln(1000)]/\alpha(\theta) \qquad \text{or } V(R_1,\theta) = 1000\mathrm{meV}$$
$$R_2 = R'_m 1 - (1/\beta')\ln[1 + (5/\epsilon')^{1/2}] \quad \text{or } V(R_2,\theta) = 5\mathrm{meV}$$
$$R_3 = R_m(1 - \ln2/\beta) \qquad\qquad \text{or } V(R_3,\theta) = 0\mathrm{meV}$$
$$R_4 = R_m(1 + \ln2/\beta)$$
$$\alpha_1 = A(\theta) - \alpha(\theta)R_1$$
$$\alpha_2 = [\ln V(R_2,\theta) - a_1]/(R_2 - R_1)$$
$$\alpha_3 = -[V'(R_1,\theta)/V(R_1,\theta) - a_2]/(R_2 - R_1) = [\alpha(\theta) + a_2]/(R_2 - R_1)$$
$$\alpha_4 = \{[V'(R_2,\theta)/V(R_2,\theta) - a_2]/(R_2 - R_1) - a_3\}/(R_2 - R_1)$$
$$\epsilon' = \epsilon(\beta - \ln2)/(\beta' - \ln2)$$
$$R'_m = R_m(\epsilon'\beta')/(\epsilon\beta)$$
$$b_1 = V(R_4,\theta)$$
$$b_2 = [V(R_5,\theta) - b_1]/(R_5 - R_4)$$
$$b_3 = -[V'(R_4,\theta) - b_2]/(R_5 - R_4)$$
$$b_4 = \{[V'(R_5,\theta) - b_2]/(R_5 - R_4) - b_3\}/(R_5 - R_4)$$

Table 5.II Formulae for Joining Points and Spline Parameters of the Beneventi Potential.

of the data, and gives an improved bending frequency of 9.1 cm^{-1}. This is the version of the potential used in the work presented here; it will be referred to as the modified Beneventi potential and is illustrated in figure 5.ii. The validity of the modification is supported by further reference to the paper of Beneventi *et al.*[131] where the lack of sensitivity to the ratio ϵ_2/ϵ_0 in the data used is noted.

Chapter 5: The Helium–Carbon Dioxide System
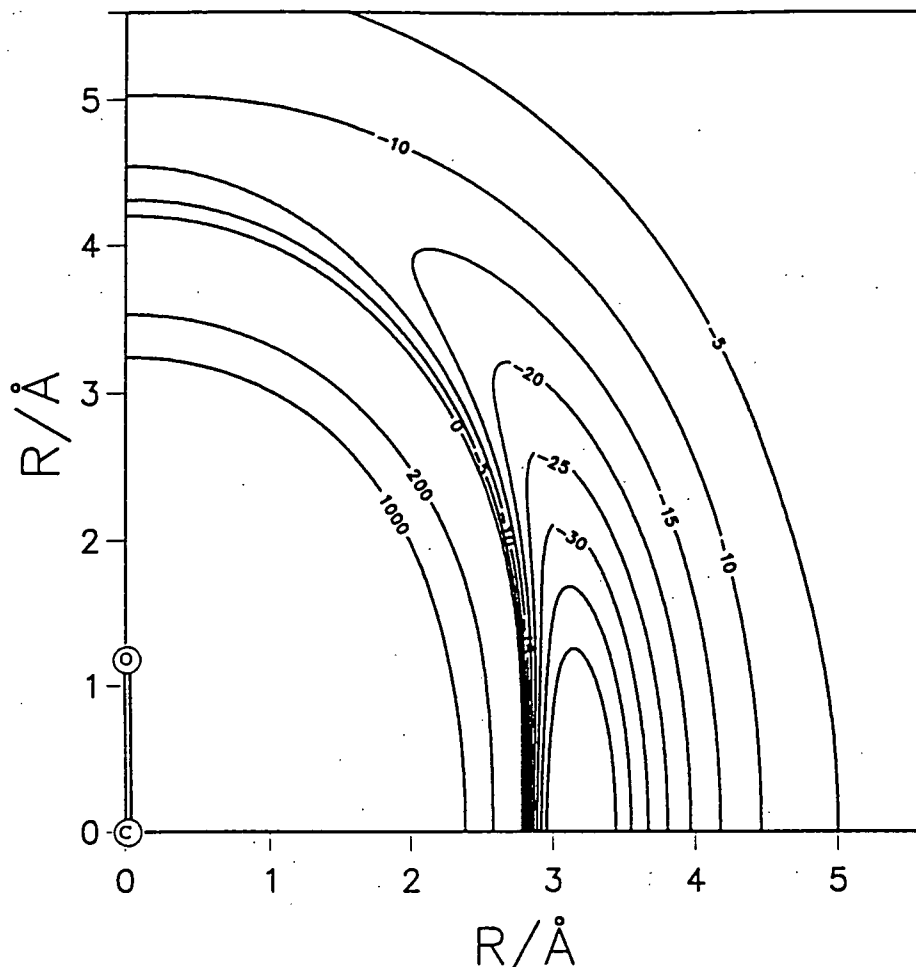
Fig. 5.ii Contour Plot of the Modified Beneventi Potential.
Contour Energies are given in cm^{-1}.

5.3 RESULTS AND DISCUSSION

The coupled equations for He–CO_2 are formulated in exactly the same way as for the argon–acetylene system and the reader is referred to equation (2.1) in chapter 2.

The coupled equations were solved using the log-derivative propagator of Manolopoulos. The monomer rotational constant for the ground state of CO_2,[171] $b'' = 0.390219cm^{-1}$, was used to calculate the monomer energy levels for values of j up to 16. The reduced mass of the complex was taken to be $\mu = 3.6687805u$ which corresponds to the $^4He^{12}C^{16}O_2$ isotopic species. The log-derivative matrix was propagated from $R_{min} = 2.0$ Å to $R_{max} = 10.0$ Å using a step size of 0.02 Å. The Legendre coefficients of the potential were evaluated using 34 point Gauss-Legendre quadrature and terms up to $P_{32}(\cos\theta)$ were included. The resulting energy levels are converged to approximately $10^{-4}cm^{-1}$.

As a consequence of nuclear spin statistics, only states with j even exist for

Chapter 5: The Helium–Carbon Dioxide System

CO_2 in its ground vibrational state exist.[172] Conversely, for the ν_3 asymmetric stretch only states with odd j exist. Calculations can be performed separately for basis sets of even and odd j functions, which are not mixed by the potential since it contains only even Legendre terms. In addition, as usual, the total parity $p' = (-1)^{j+L}$ is a good quantum number, so that the coupled equations for each total angular momentum J factorise into four uncoupled sets.

j parity p' J	even +1	even -1	odd +1	odd -1
0	-19.5762		-10.5000	
0	-6.0817		-2.9357	
0	-0.1438			
1	-9.4616	-18.9919	-18.7526	-18.9634
1		-9.7569	-4.4044	-9.9018
1		-5.3809		-4.9915
1		-1.2191		-1.9647
2	-18.0029	-17.3032	-18.0167	-17.3886
2	-17.1288	-8.0930	-8.8422	-7.7343
2	-8.9318	-2.2694	-7.6765	-2.9631
2	-4.0833		-4.3153	
2	-2.7098		-0.4180	
2	-0.4421			
3	-15.6160	-16.6671	-15.5578	-16.6730
3	-6.1212	-15.0465	-14.7383	-14.8657
3	-5.0126	-7.6700	-6.2412	-7.5469
3	-0.7417	-5.1018	-0.9785	-5.9347
3		-2.5136		-2.9807
3		-1.6949		
4	-14.9690	-13.4795	-14.9593	-13.4443
4	-12.4074	-11.6799	-12.5489	-12.0216
4	-11.6082	-3.8544	-6.0115	-4.2068
4	-6.0023	-3.0421	-3.5411	-1.5664
4	-3.6607		-1.6566	
4	-0.8825		-0.9750	

Table 5.III Vibration-Rotation Energy Levels from Close Coupling Calculations on the Modified Beneventi Potential. Energies are given in cm^{-1}.
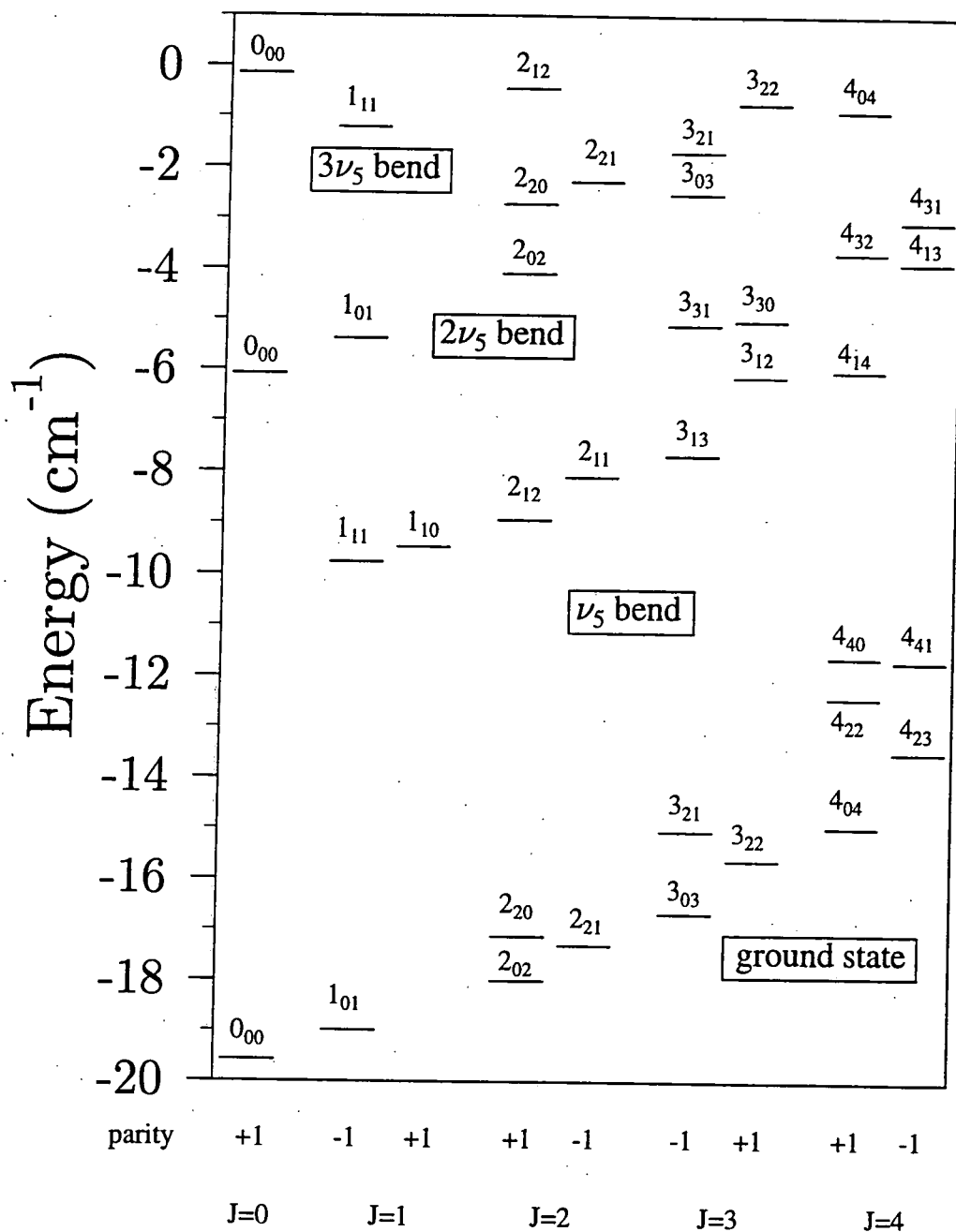
Fig. 5.iii Asymmetric Top Energy Levels for He–CO₂ in the CO₂ Ground Vibrational State from Close Coupling Calculations on the Modified Beneventi potential.

Calculations of energy levels and wavefunctions were carried out for all bound states using the modified potential. For $J > 9$ no bound states exist. For the $J = 0$ to 4 bound states the energy levels are presented in table 5.III and figures 5.iii and 5.iv. Figure 5.iii contains levels with j even only i.e. those corresponding

Chapter 5: The Helium–Carbon Dioxide System
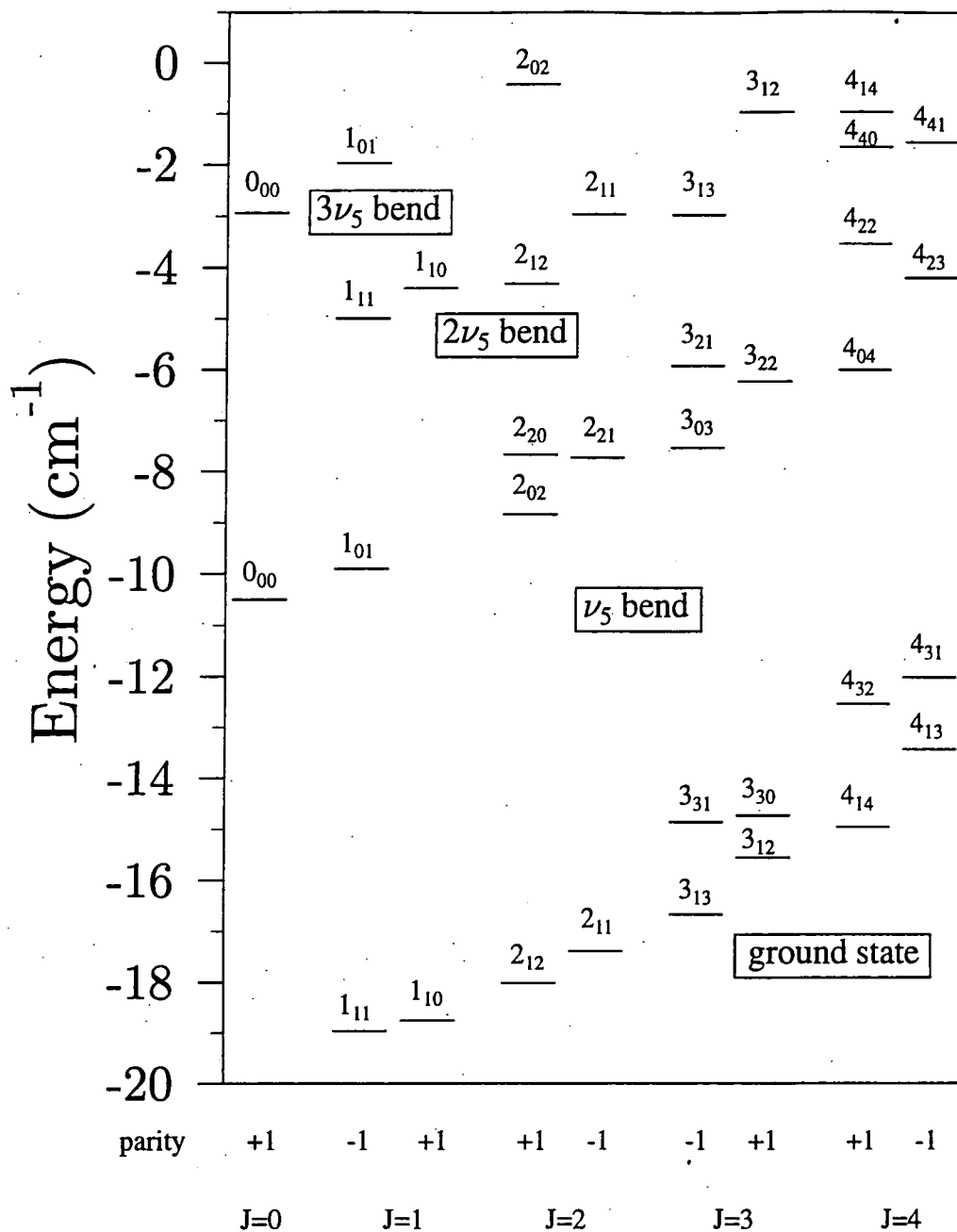
Fig. 5.iv Asymmetric Top Energy Levels for He–CO_2 in the CO_2 ν_3 Vibrational State from Close Coupling Calculations on the Modified Beneventi potential.

to the ground vibrational state on CO_2 . Figure 5.iv contains levels with j odd only which would correspond to the ν_3 asymmetric vibrational state of CO_2 . In using these j odd levels as upper state levels for the calculation of the spectra the assumption is made that the change in monomer vibrational state will not affect

Chapter 5: The Helium–Carbon Dioxide System

the intermolecular potential. The dependence of the intermolecular potential on the monomer vibrational states has been considered for complexes such as Ar–HF104 and Ar–HCl[173] and shifts in absolute well depth and rotational ground state frequencies were found to be of the order of 10% in Ar–HF and 2% in Ar–HCl . Whilst these are in no way transferable results they lend credibility to the assumption that neglecting the effect of the monomer vibrational state on the intermolecular potential is a reasonable approximation. The small blue shift of 0.095cm^{-1} in the ν_3 vibrational frequency for CO_2 upon complexation[132] corroborates this argument.

Following the work of Weida *et al.*[132] we note that asymmetric top quantum numbers K_A and K_C are restricted by

(1) The A axis of the complex is the internuclear vector, so for the Van der Waals ground state $(-1)^{K_A} = (-1)^j$. Thus the ground states with even j basis set must have even K_A and those from the odd j basis must have odd K_A . Conversely, for the first excited ν_5 bending state, states arising from the even j basis set must have odd K_A and *vice versa.*

(2) Asymmetric top functions for planar molecules have total parity $(-1)^{K_C}$, so that even parity states must have even K_C and odd parity states must have odd K_C.

(3) Because He–CO_2 is in the oblate limit for an asymmetric top, the highest energy levels of a given J will have the lowest values of K_C.

This allows us to assign the $J_{K_A K_C}$ asymmetric top levels as shown in figures 5.iii and 5.iv.

Assuming that the majority of the intensity in the complex spectrum arises from the CO_2 $\nu_3 = 1 \leftarrow 0$ transition dipole, which lies along the CO_2 axis, we apply the direct dipole only-model as outlined in section 4.4 of chapter 4. The intensities were calculated using a temperature of 4.6 K, taken from the experiment,[132] in the Boltzmann factor. The intensities were scaled so that the calculated intensity for the $2_{12} \leftarrow 3_{03}$ transition matched the given experimental value for this, the most intense, transition.

The absolute frequency of the calculated spectrum was fixed using the value of 2349.14326 cm^{-1} for the CO_2 ν_3 asymmetric stretch.[171]

Figure 5.v shows the entire calculated spectrum. Figure 5.vi shows calculated ground state levels together with the ground state levels assigned in the exper-

Chapter 5: The Helium–Carbon Dioxide System
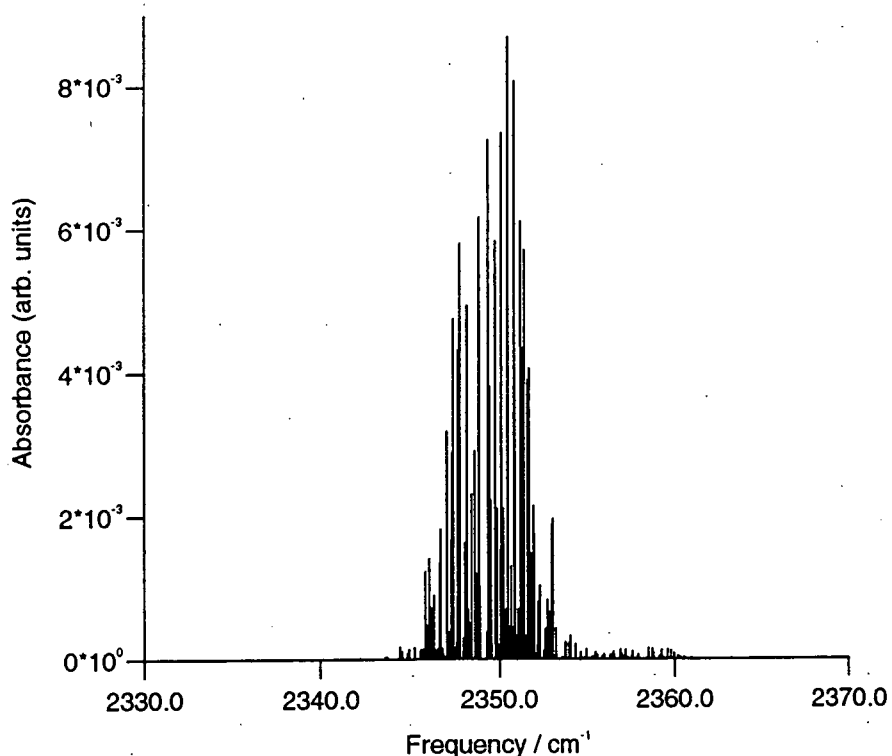
Fig. 5.v He–CO$_2$ Entire Calculated Spectrum

imental work for which, unfortunately, intensity information was not provided. Only the region in which transitions were observed is shown in the latter figure. The correlation between some of the more intense calculated lines and the correspondingly assigned observed transitions is indicated. A reasonably constant shift of about 0.1 cm^{-1} to the blue is seen. This is most probably due to the neglect of change in the potential in the vibrationally excited state, the observed blue shift of 0.095 cm^{-1} corroborates this and would indicate that the energy levels are shifted upward slightly in the excited state.

In figure 5.vii the segment of spectrum from 2346.6 to 2348.6 cm^{-1} presented in the experimental paper is reproduced together with the calculated spectrum. This confirms that some of the lines attributed to the hot band indeed arise from there but discrepancies exist, particularly in the region around 2348.4 cm^{-1} where 4 observed transitions lie close together. Two, the $4_{32} - 4_{41}$ and $5_{33} - 5_{42}$ transitions, are found in both calculated spectra, in the modified Beneventi potential spectrum they lie just below 2348.3 cm^{-1}. Neither of the lines attributed to the hot band appear in the calculation.

In figure 5.viii calculated and observed lines for the hot band alone are presented. Levels in the calculated spectrum are labelled with their upper and lower

Chapter 5: The Helium–Carbon Dioxide System
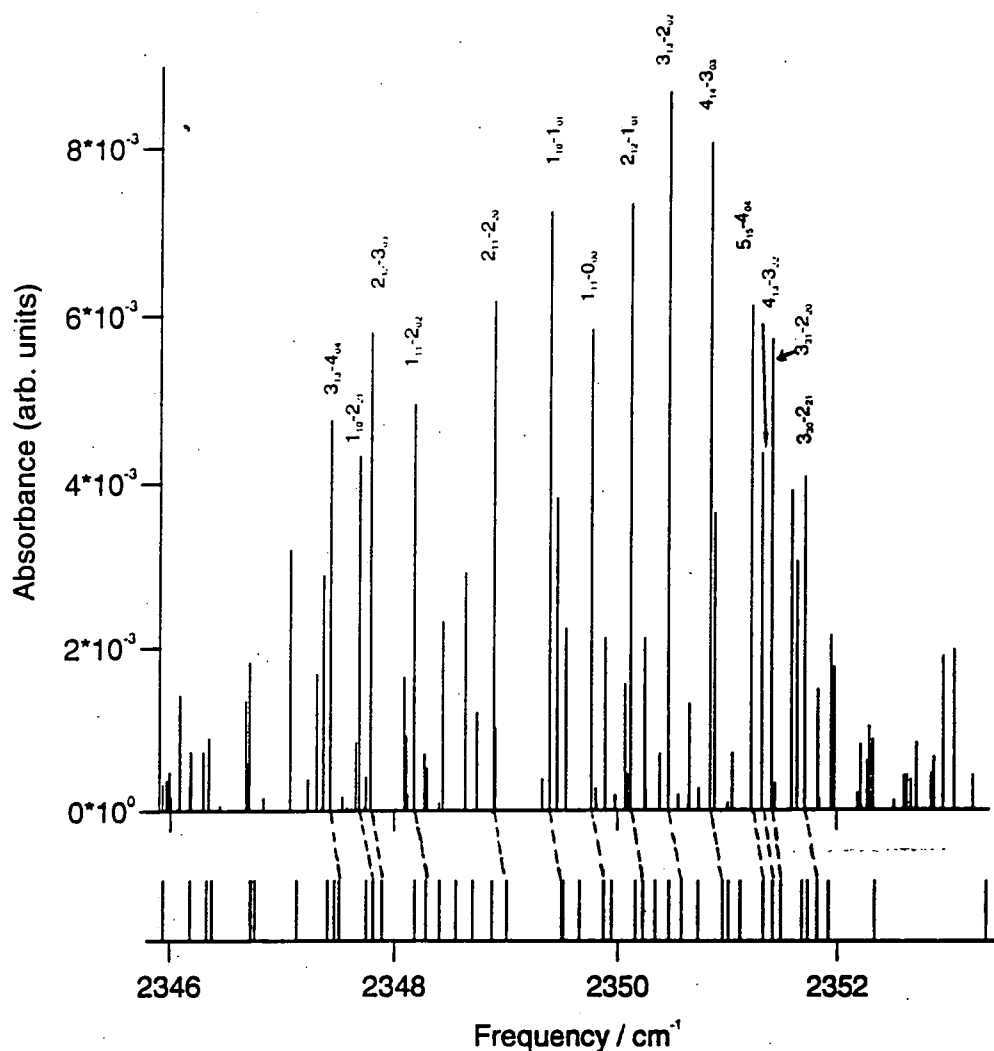
Fig. 5.vi He–CO₂ Transitions arising from ground state levels, calculated (above) and observed (below) lines. Dotted lines connect the more intense lines with the corresponding observed levels.

states and a tentative assignment of the observed levels is made. The intensities of the observed lines are measured to an accuracy of $\pm 2 \times 10^{-4}$ units and thus care must be taken not to overemphasise a comparison of intensities between the two graphs. One could endeavour to assign more lines but reliable assignments are impossible at this stage. Whilst the hot band transitions are still calculated to be less intense than observed there is an improvement on the 50% error reported from the Beneventi potential.[132]

The final calculated results presented in figure 5.ix are for the combination band $\nu_4 + \nu_5$. With the strongest transition having a relative absorbance of 1.5×10^{-4}, compared to the weakest hot band transition which was measured

Chapter 5: The Helium–Carbon Dioxide System
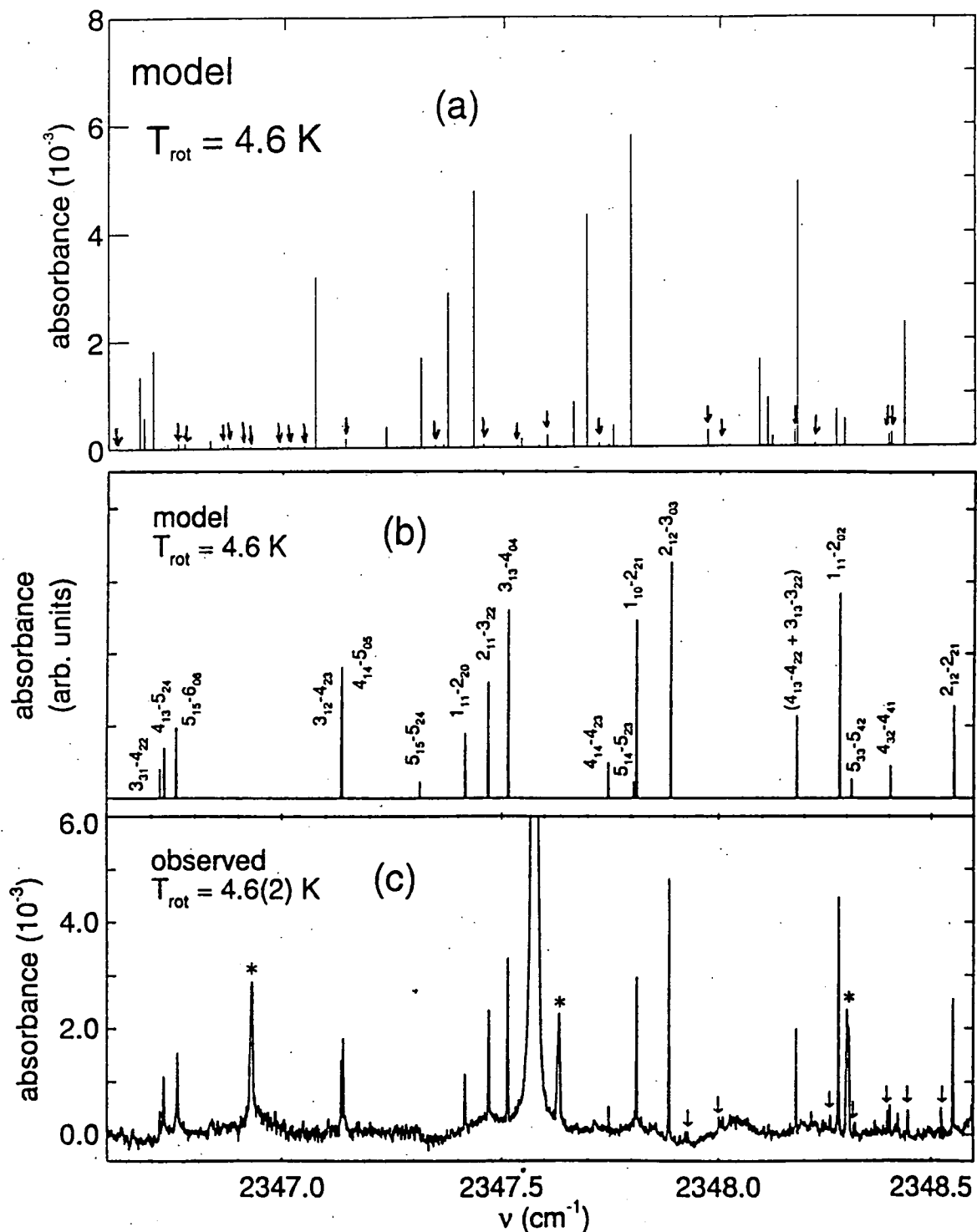
Fig. 5.vii He–CO$_2$ Comparison of experimental and calculated results in the region 2346.6 to 2348.6 cm^{-1}. (a) Close coupling calculation from the modified Beneventi potential. Arrows mark hot band transitions. (b) Variational calculation from the Beneventi potential. (c) Experimental results. Arrows mark transitions believed to arise from the hot band.(b) and (c) reproduced from ref. 132 with permission.

*Chapter 5: The Helium–Carbon Dioxide System*
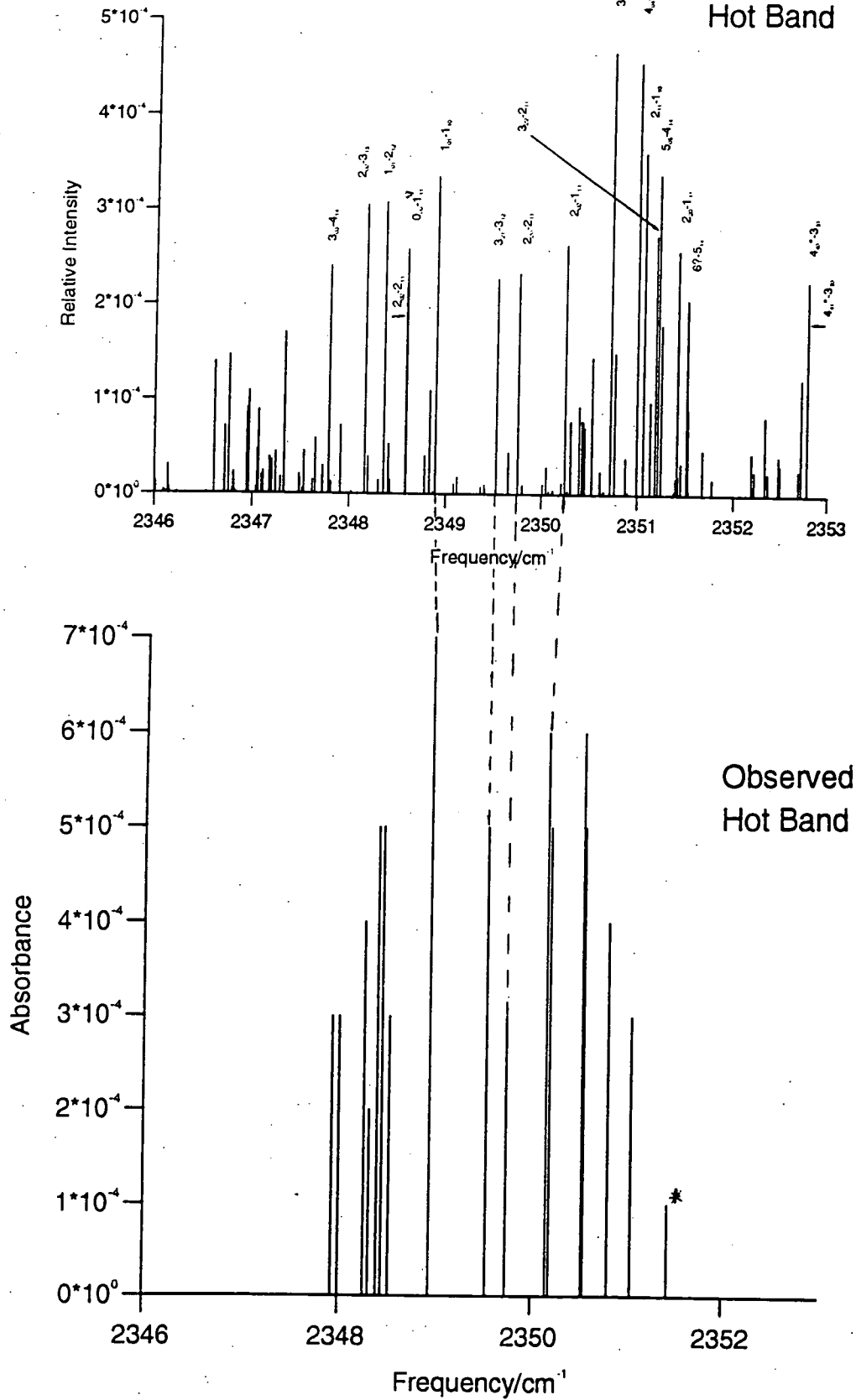
Fig. 5.viii He–CO$_2$ Calculated and observed hot band transitions in the region of all the observed hot band lines. Dotted lines indicate (very) tentative assignment.

* intensity undetermined

*Chapter 5: The Helium–Carbon Dioxide System*
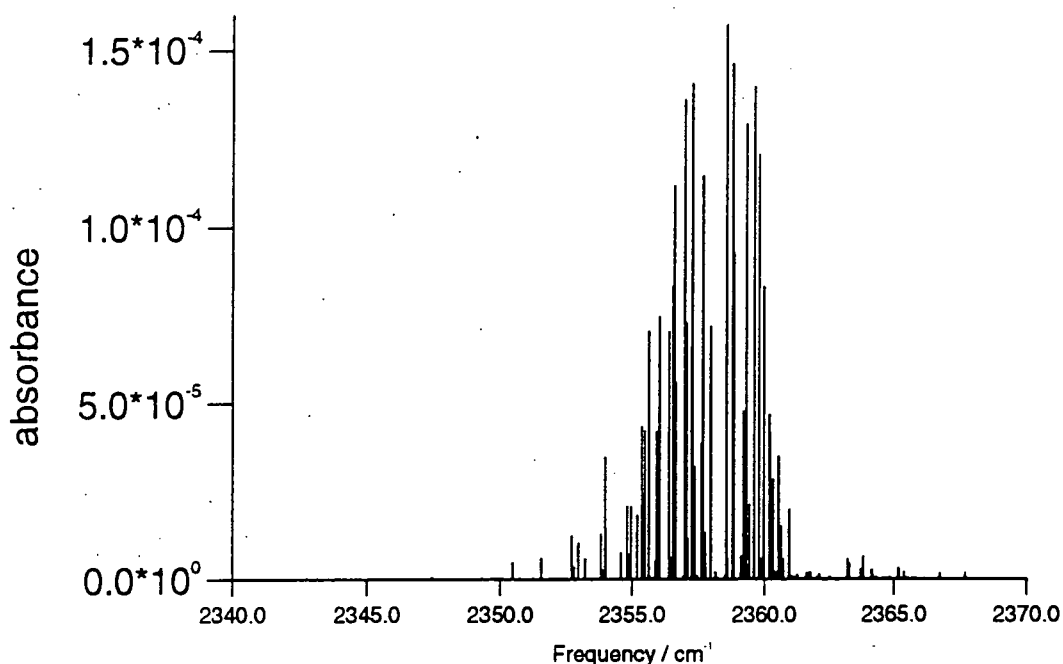
Fig. 5.ix He–CO$_2$ Calculated Combination Band Transitions.

with an absorbance of $2 \times 10^{-4} \pm 2 \times 10^{-4}$, the band will clearly be below the detection limit.

5.4 CONCLUSIONS AND FUTURE DIRECTIONS

Close-coupling calculations have been performed for He–CO$_2$ using a modified version of the Beneventi potential with increased anisotropy. This potential reproduces the ν_4 band experimental data reasonably, has confirmed that the ν_5 hot band will be observable but that the $\nu_4 + \nu_5$ combination band will not be at this level of experimental detection capability. A tentative assignment of some of the hot band transitions has been made.

An improved potential energy surface will be required to take this work any further. Fitting, including the new spectroscopic data,[132] would be one way of achieving this and the tentative assignment of the hot band levels will assist this process, especially for regions of the potential away from the minimum.

Chapter 5: The Helium–Carbon Dioxide System

Chapter 6: THE ARGON–ETHENE SYSTEM

6.1 INTRODUCTION

The Ar–C_2H_4 system is the least well studied Van der Waals complex considered in this thesis. Much early work on rare gas–C_2H_4 systems concentrated on the vibrational predissociation dynamics as a first step towards understanding such processes in larger molecules with many close-lying vibrational modes. Both experimental[174–177] and theoretical[59,178–180] work has focussed on these predissociation phenomena. However all the theoretical work has used a simple atom-atom pairwise additive potential form, for which the parameters could not be determined accurately. Danielson *et al.*[181] have measured differential cross sections for the He–C_2H_4 system as well as diffusion properties and second virial coefficients. They conclude the level of anisotropy in this system is similar to the He–C_2H_2 system. The Ne–C_2H_4 infrared spectrum in the region of the C_2H_4 ν_7 vibration has been the subject of theoretical attention[182,183] but again using a pairwise additive potential.

During the course of this work Block *et al.*[184] published the first infrared spectroscopic study of Ar–C_2H_4 in the region of the C_2H_4 ν_9 and ν_{11} bands. Their results will be discussed at the end of this chapter.

6.2 CO-ORDINATES AND POTENTIAL

The generalised Jacobi coordinates for an atom-nonlinear molecule system are illustrated for Ar–C_2H_4 in figure 6.i. It is worthwhile noting that an angle of $\chi = 90°$ places the argon atom above the plane of the molecule whilst that of $\chi = 0°$ places it in the plane of the molecule. Note that the monomer x, y and z axes used in the present work are different from those in refs. (179, 59).

The pairwise additive potential of Peet *et al.*[59] was chosen as the best available. This potential will hereafter be referred to as the Peet potential. The repulsive atom-atom potentials are represented by the functional form,

$$V(\text{Ar} - C_2H_4) = \sum_{i=1}^{2} [A_C^0 + A_C^2 P_2(\cos \alpha)] \exp(-\beta_{Ci} R_{Ci}) + \sum_{i=1}^{4} A_H \exp(-\beta_{Hi} R_{Hi}).$$

$$(6.1)$$

Here α is the angle between the monomer fixed x axis and R and thus
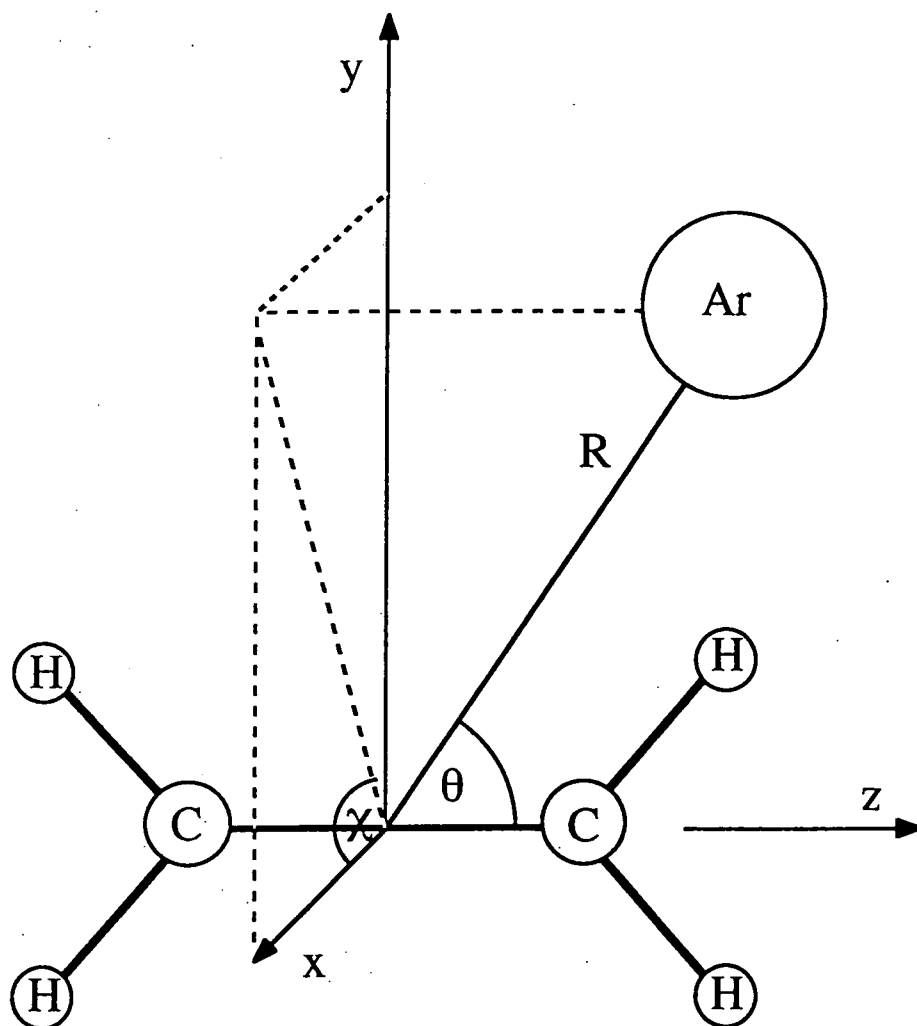
Fig. 6.i Coordinate System for Ar–C_2H_4 .

$$P_2(\cos\alpha) = \frac{1}{2}(3\sin^2\theta\cos^2\chi - 1).$$ (6.2)

The attractive parts take a similar form,

$$V(\text{Ar} - C_2H_4) = -\sum_{i=1}^{2}[C_C^0 + C_C^2 P_2(\cos\alpha)]/R_{Ci}^6 - \sum_{i=1}^{4} C_H/R_{Hi}^6.$$ (6.3)

The parameters used by the Peet potential are given in table 6.I . It is noted here that the units for the repulsive A coefficients given in the original paper were in fact hartrees not eV as written.

Chapter 6: The Argon–Ethene System

A_C^0/E_h	588
A_C^2/E_h	424
A_H/E_h	34.15
β_C/a_0^{-1}	2.132
β_H/a_0^{-1}	1.959
C_C^0/au	64.1
C_C^2/au	3.0
C_H/au	18.6

Table 6.I Parameters for the Peet Potential.

The potential has a global minimum in the T-shaped geometry when χ is around 56° at R about 3.8Å with a well depth of about 230 cm^{-1}. Contour plots of the potential in various planes are shown in figure 6.ii.

A plot of the well depth as a function of θ is shown in figure 6.iiia where R and χ have been varied to find the potential minimum for each θ. This gives the barrier to rotation in θ out of the global minimum as about 65 cm^{-1}. The function of χ at $\theta = 90°$ varying R only is shown in figure 6.iiib and the barrier to rotation in χ out of the global minimum towards the planar geometry is seen to be about 18cm^{-1} and towards the out of plane geometry about 44 cm^{-1}.

6.3 RESULTS AND DISCUSSION

The atom-molecule coupled equations as given in equation (1.7) were solved using the quasiadiabatic modified log-derivative propagator of Manolopoulos. The monomer rotational constants for the ground state of C_2H_4,[185] $B_x = 0.82810$ cm^{-1}, $B_y = 1.00097$ cm^{-1}, $B_z = 4.86550$ cm^{-1}, were used to calculate the basis functions for values of j up to 24. To reduce the total number of basis functions it was found that the maximum energy of included functions could be limited to 800 cm^{-1} whilst maintaining satisfactory convergence. The reduced mass of the complex was taken to be $\mu = 16.475030$u which corresponds to the ^{40}Ar ^{12}C$_2$ ^{1}H$_4$ isotopic species. The log-derivative matrix was propagated from $R_{\text{min}} = 2.9$ Å to $R_{\text{max}} = 8.0$ Å using a step size of 0.02 Å. The potential was expanded in renormalised spherical harmonics as in equation (1.4). Terms in λ up to 24 and μ up to 10 were included. Because of symmetry restrictions, only coefficients with even λ and μ are required. These coefficients were projected out using 32-point Gauss-Legendre quadrature in θ and 16-point equally spaced quadrature in χ. The resulting energy levels are converged to approximately 10^{-5} cm^{-1}.

Chapter 6: The Argon–Ethene System
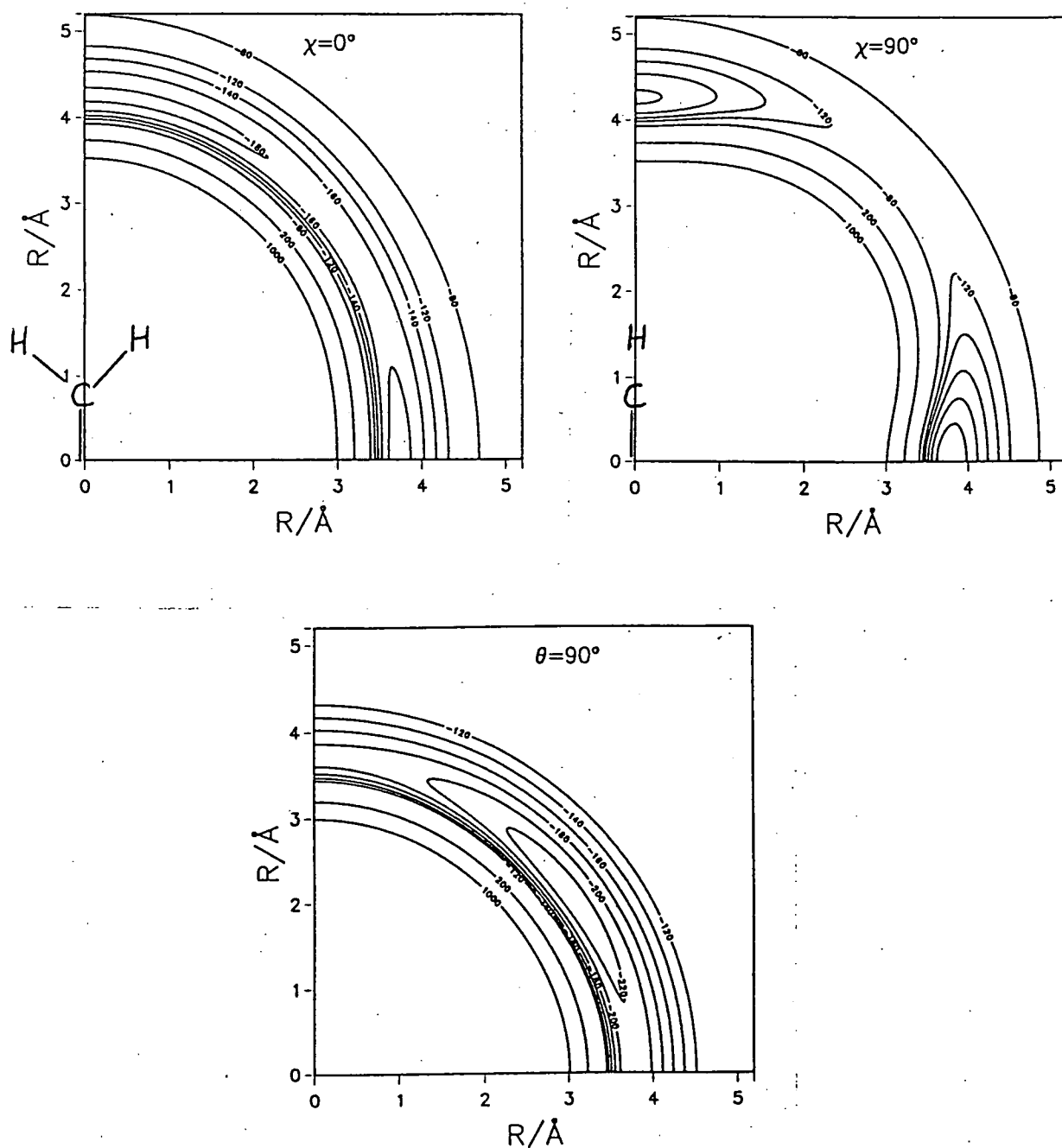
Fig. 6.ii Plots of the Peet Potential. (a) In the molecule plane. (b) Perpendicular to the molecule plane along molecule axis. (c) Perpendicular to molecule plane and molecule axis.

For an atom-asymmetric top complex in the body-fixed representation the

Chapter 6: The Argon–Ethene System

(a)

(b)
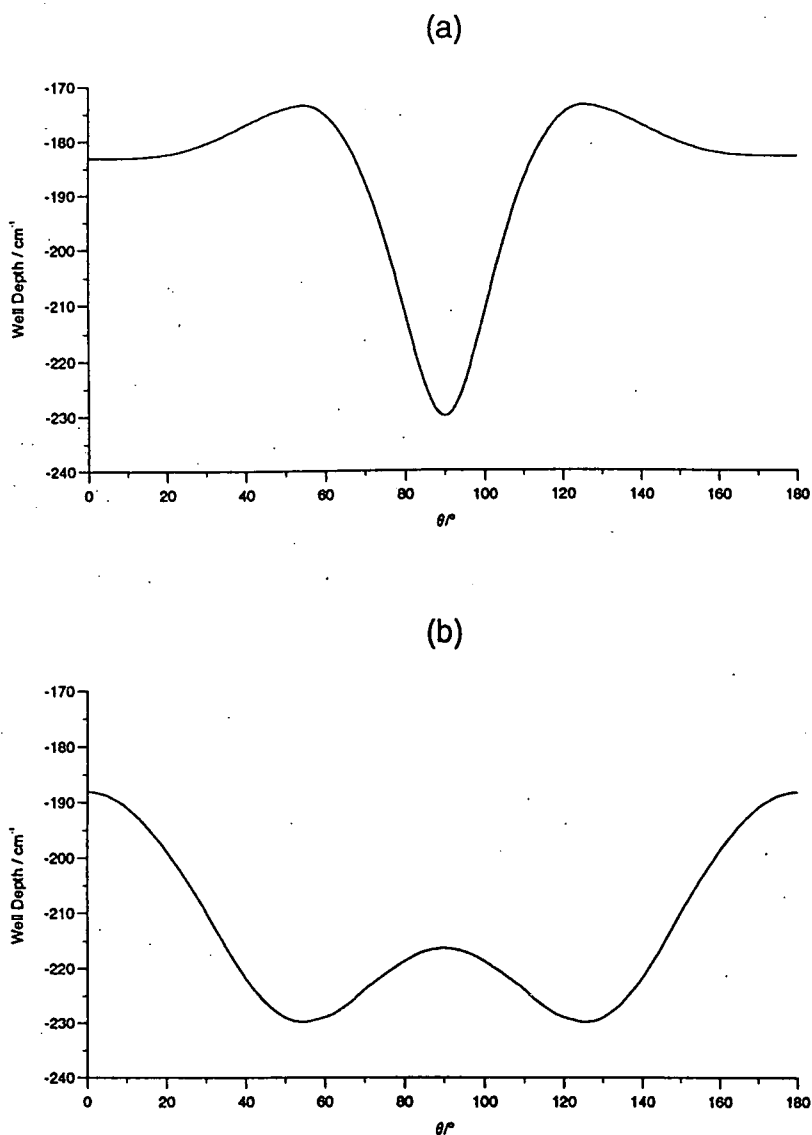
Fig. 6.iii Well depth as a function of angle. (a) Function of θ where R and χ have been varied to find the deepest point in the well at each angle. (b) Function of χ at $\theta = 90°$ where R only has been varied.

total wavefunction of a state α is expanded,

$$\chi_\alpha^{JM} = R^{-1} \sum_{j\tau K} \left(\frac{2J+1}{4\pi}\right)^{\frac{1}{2}} D_{MK}^J(\alpha_R \beta_R 0)\phi_{K\tau}^j(\phi, \theta, \chi)\psi_{j\tau K}^{J\alpha}. \qquad (6.4)$$

The monomer rotation functions $\phi_{K\tau}^j$ used in the angular basis set are linear combinations of normalised rotation matrices,

$$\phi_{K\tau}^j(\phi, \theta, \chi) = \left(\frac{2j+1}{8\pi^2}\right)^{\frac{1}{2}} \sum_{k=-j}^{j} B_{\tau k}^j D_{Kk}^{j*}(\phi, \theta, \chi). \qquad (6.5)$$

Chapter 6: The Argon–Ethene System

The symmetries of the monomer functions are such that, $B_{\tau k}^{j} = \epsilon B_{\tau -k}^{j}$ and thus equation (6.5) can be expanded,

$$\sum_{k=-j}^{j} B_{\tau k}^{j} D_{Kk}^{j*} = B_{\tau 0}^{j} D_{K0}^{j*} + \sum_{k=1}^{j} \left\{ B_{\tau k}^{j} D_{Kk}^{j*} + \epsilon B_{\tau k}^{j} D_{K-k}^{j*} \right\}, \qquad (6.6)$$

Considering the equation (1.14) it is clear that the implication of the first 3-j symbol $\begin{pmatrix} j & \lambda & j' \\ -k & \mu & k' \end{pmatrix}$ is that if only even μ terms are present then functions with k even are not coupled to those with k odd. In addition consideration of the reflection properties of the monomer eigenfunctions in the xy plane[20] leads to the conclusion that if only terms with $(\lambda + \mu)$ even are present functions with $\epsilon(-1)^{j}$ even are not coupled to those with $\epsilon(-1)^{j}$ odd. Calculations can thus be performed separately for each combination of $(-)^{k}$ and $\epsilon(-1)^{j}$ symmetry. In addition, as usual, the total parity is a good quantum number, so that the coupled equations for each total angular momentum J factorise into eight uncoupled sets. Calculations of energy levels and wavefunctions were carried out for all bound states below an energy of -130 cm^{-1} for $J = 0$ and 1. The energy levels are presented in table 6.II and figure 6.iv. The 4 possible symmetry cases are labelled by the ethylene point group, D_{2h}, representations,[179] and the symmetry restrictions for each case are laid out in table 6.III. The full character table of D_{2h} contains 8 irreducible representations. Each of the representations given here will be split into gerade and ungerade representations by the inversion operator.

Symmetry Operator	Symmetry Restriction	A	B$_2$	B$_3$	B$_1$
σ_{xy}	$\epsilon(-)^{j}$	$+1$	$+1$	-1	-1
C_2^z	$(-1)^{k}$	$+1$	-1	$+1$	-1

Table 6.III Symmetry Case labels for Ar–C$_2$H$_4$.

It was not possible from the level energies alone to make even an assignment of which were bending and which stretching states. Thus it was decided to plot wavefunctions for the $J = 0$ levels. In order to do this it was necessary to switch to the diabatic modified log-derivative propagator of Manolopoulos which has poorer convergence properties with respect to the step size than the quasiadiabatic propagator in this complex. However for the purpose of plotting the wavefunction the convergence with the same integration parameters as used previously

Chapter 6: The Argon-Ethene System

	J	=	0					
	A		B$_2$		B$_3$		B$_1$	
p'	-1	$+1$	-1	$+1$	-1	$+1$	-1	$+1$
		-170.52		-164.39	-155.40	-140.60	-167.08	-138.94
		-145.97		-134.28		-137.59	-133.19	
		-139.21						
		-135.51						

	J	=	1					
	A		B$_2$		B$_3$		B$_1$	
p'	$+1$	-1	$+1$	-1	$+1$	-1	$+1$	-1
	-154.41	-170.38	-166.05	-166.05	-169.50	-169.50	-166.95	-163.41
	-138.74	-154.41	-138.09	-164.24	-155.27	-144.96	-163.40	-138.81
		-145.83	-133.57	-138.09	-144.95	-140.48	-135.33	-135.32
		-139.14	-132.14	-134.22	-135.30	-137.49	-133.06	-130.69
		-138.70		-133.51		-135.30	-130.66	
		-135.39	-132.14					

Table 6.II Close-coupling calculations of energy levels of Ar–C$_2$H$_4$ using the Peet potential. All energies are given in cm^{-1}, relative to the dissociation threshold. All levels below -130 cm^{-1} are included.

was found to be more than satisfactory. The helicity decoupling approximation was also made, neglecting the off-diagonal Coriolis matrix elements of equation (1.16) and thus allowing each K state to be considered individually. For $J = 0$ helicity decoupling calculations are equivalent to close-coupling calculations and so for these states no approximation is made.

Using the properties of rotation matrices, and considering only states with $K = 0$, equation (6.5) may be rewritten,

$$\phi_{0\tau}^{j} = (-)^{j} \left(\frac{2j+1}{8\pi^2}\right)^{\frac{1}{2}} \sum_{k=-j}^{j} B_{\tau k}^{j} C_{jk}(\pi - \theta, \chi), \qquad (6.7)$$

where the functions C_{jk} are renormalised spherical harmonics. Expanding the sum,

$$\phi_{0\tau}^{j} = (-)^{j} \left(\frac{2j+1}{8\pi^2}\right)^{\frac{1}{2}} \left\{ B_{\tau 0}^{j} C_{j0}(\pi - \theta, \chi) \right.$$
$$\left. + \sum_{k=1}^{j} B_{\tau k}^{j} \left[C_{jk}(\pi - \theta, \chi) + \epsilon C_{j-k}(\pi - \theta, \chi) \right] \right\}. \qquad (6.8)$$

Chapter 6: The Argon–Ethene System
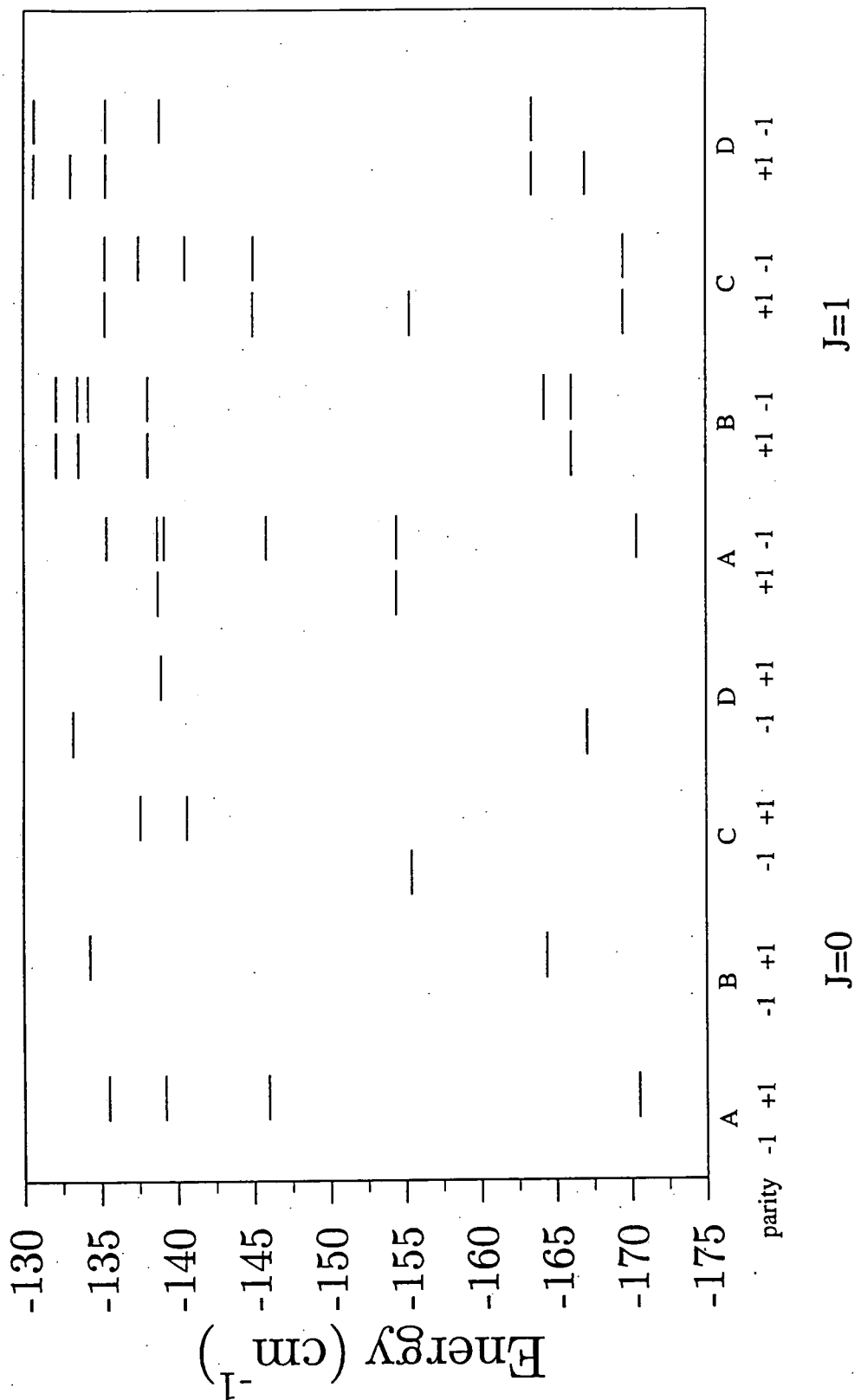
Fig. 6.iv Energy Levels for Ar–C$_2$H$_4$ from the Peet Potential. All Energy Levels up to –130 cm^{-1} Inclusive.

Using the properties of the functions C_{jk} this may be written,

$$
\phi_{0\tau}^j = (-)^j \left(\frac{2j+1}{8\pi^2}\right)^{\frac{1}{2}} \left\{ B_{\tau 0}^j P_j^0(\pi-\theta,\chi) \right.
$$
$$
\left. + \sum_{k=1}^{j} (-)^k \left[\frac{(j-k)}{(j+k)}\right]^{\frac{1}{2}} P_j^k(\pi-\theta,\chi) B_{\tau k}^j \left\{ e^{ik\chi} + \epsilon(-)^k e^{-ik\chi} \right\} \right\}.
$$

(6.9)

If $\epsilon(-)^k$ is even then

$$
\left\{ e^{ik\chi} + \epsilon(-)^k e^{-ik\chi} \right\} = 2\cos(k\chi).
$$

Similarly $\epsilon(-)^k$ odd gives

$$
\left\{ e^{ik\chi} + \epsilon(-)^k e^{-ik\chi} \right\} = 2i\sin(k\chi).
$$

For a given channel labelled j, τ, K the terms in the sum are either all sine or all cosine terms. For helicity decoupled calculations with $K = 0$ some additional symmetry restrictions apply, generated by the second 3-j symbol of equation (1.14), $\begin{pmatrix} j & \lambda & j' \\ -K & 0 & K \end{pmatrix}$. Because the bottom row contains entirely zeroes the sum of the top row must be even. As λ is even in Ar–C_2H_4 this implies that the basis functions contributing to a particular state of the complex must all have either even j or odd j. When combined with the $\epsilon(-)^j$ symmetry this implies that ϵ must be conserved for a given level. The upshot of this is that for a given level the expression (6.9) for $\phi_{0\tau}^j$ will be made up entirely of either sine or cosine terms. Substitution of the expression (6.9) in equation (6.4) allows evaluation of the wavefunction as detailed in chapter 4.

Plots of the wavefunctions as a function of θ and χ at intermolecular distance $R = 3.8$ Å, close to the equilibrium separation, for the lowest energy level in each symmetry category are shown in figure 6.v . All these states lie well below the energy barrier to rotation in θ but above the barrier to rotation in χ; this is reflected in their localisation about $\theta = 90°$ but delocalisation in the χ coordinate. The ground state shown in figure 6.v(a) has no nodes and correlates in the free rotor limit with the $j = 0$ level of the C_2H_4 monomer. Figure 6.vi shows this ground state as a function of R and θ for various cuts in χ. Although the amplitude of this wavefunction is largest at the potential minimum, it samples all of the χ coordinate. Steric hindrance by the H atoms is observed as a reduction of the spread in θ on approaching the planar geometry. The $j = 1$ free-rotor level would give rise to three states for $k = 0, \pm 1$. These states would have symmetry

Chapter 6: The Argon–Ethene System

properties analogous to those of atomic p orbitals; the $k = 0$ state has a nodal plane at $\theta = 90°$ and the combinations of the two $k = \pm 1$ states give rise to states with nodal planes at $\chi = 0°$ and $\chi = 90°$. The symmetry character of the latter two states is clearly seen in 6.v(b) and (c); the $k = 0$ state is expected to lie at a much higher energy as a nodal plane at $\theta = 90°$ will force the wavefunction away from the $\theta = 90°$ minimum into higher energy regions. The final state 6.v(d) has two nodal planes and must therefore correlate to a $j = 2$ free rotor state.
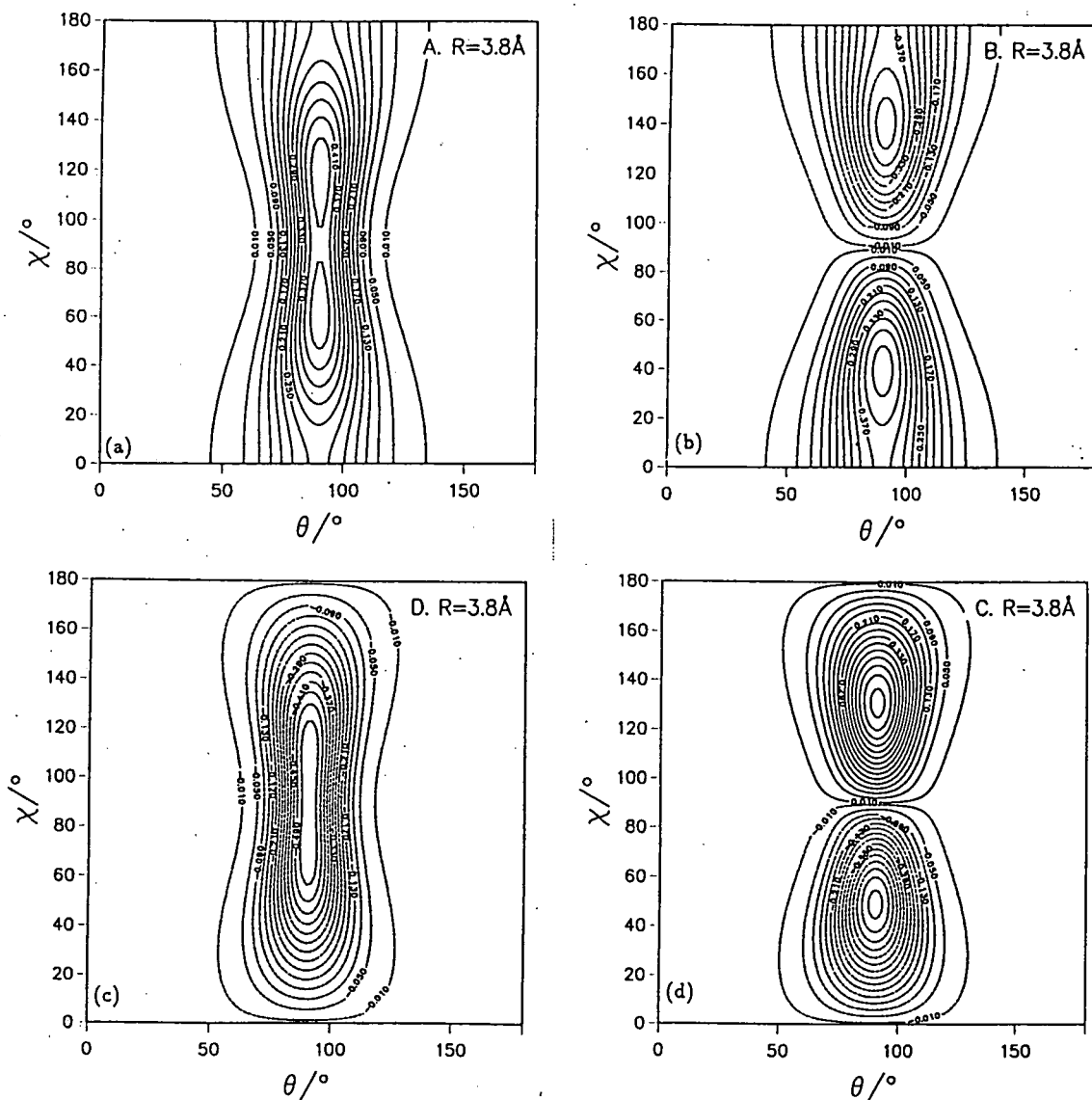
Fig. 6.v Lowest Energy Level of Ar–C_2H_4 in each Symmetry Category as a Function of θ and χ. (a) Ground State (Symmetry A), (b) Symmetry B_2, (c)Symmetry B_1, (d)Symmetry B_3.

The lowest state with significant amplitude away from the $\theta = 90°$ well is the level at -139.21 cm^{-1} with symmetry A, $p' = +1$; this is illustrated in figure 6.vii. It is interesting to note that this state is largely localised around the end-on

Chapter 6: The Argon–Ethene System
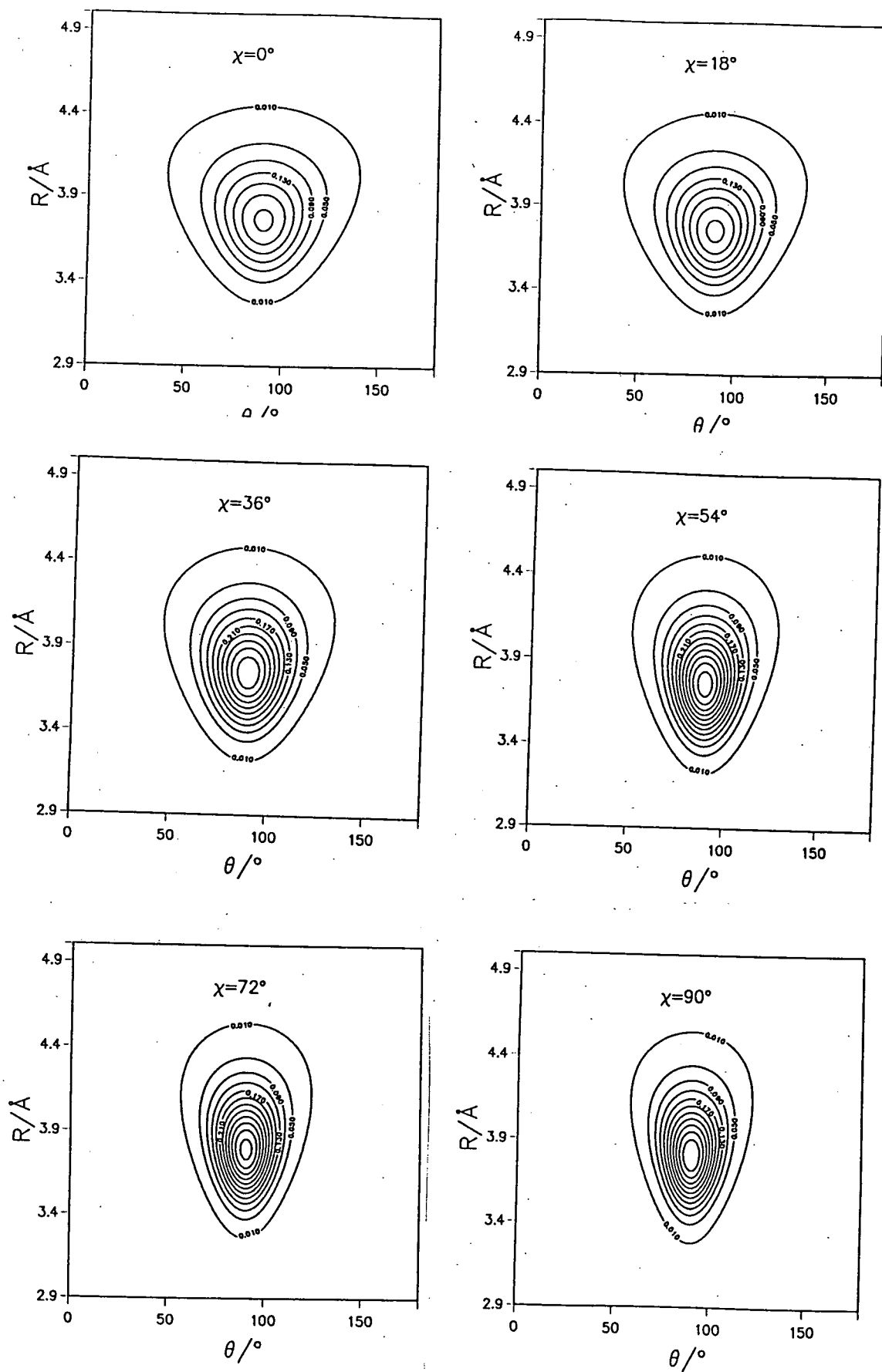
Fig. 6.vi Ground State as a Function of R and θ for various cuts in χ.

Chapter 6: The Argon–Ethene System

geometry, despite the fact that the barrier to rotation out of this position is less than 10 cm^{-1}.
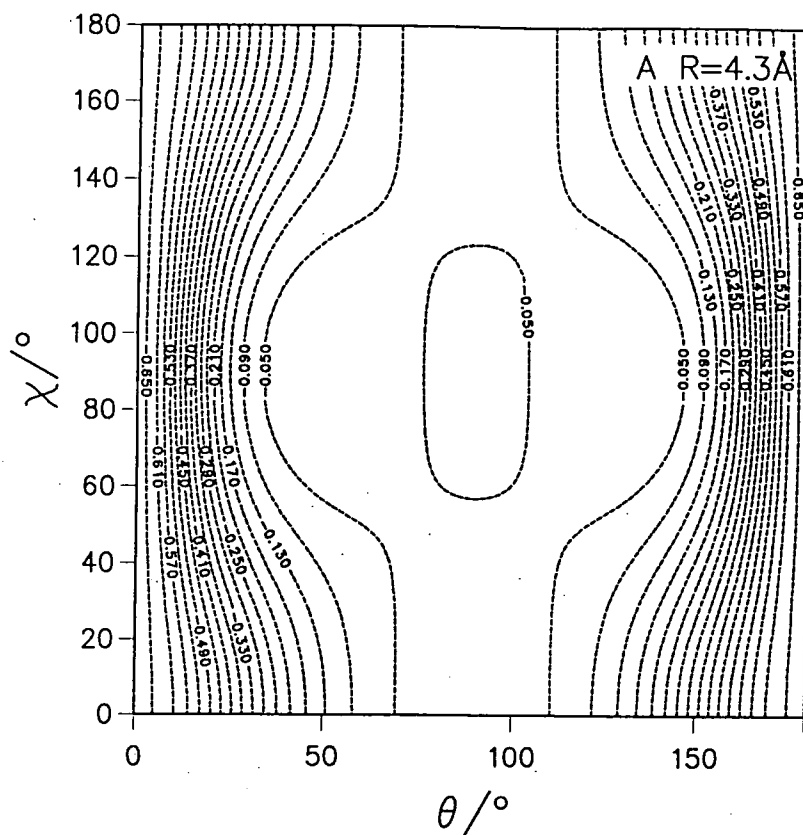
Fig. 6.vii Plots of the lowest state to significantly sample the well away from $\theta = 90°$.

6.4 SUBSEQUENT WORK

In a recent paper Block *et al.*[184] reported high resolution infrared spectra for the Ar–C_2H_4 complex in the region of the C_2H_4 monomer ν_9 and ν_{11} bands. A rigid-rotor analysis yielded rotational constants which imply an equilibrium geometry with $\chi = 75°$ and $R = 3.98$ Å. However such a structure would give C-type bands which were not observed. The bands observed suggest that in the ground state the complex is undergoing a wide-amplitude motion about the planar structure.

All the transitions observed appeared as doublets, which was rationalised in terms of a C_2H_4 internal rotation. Since steric effects make in-plane rotation unlikely, the rotation responsible for the splitting was believed to be that about the C_2H_4 C-C double bond. This conclusion was confirmed by the observed effect

of nuclear spin statistics on the intensities. By fitting to a simple one-dimensional $V_2 \cos(2\theta)$ potential the barrier to this internal rotation was found to be 76 cm^{-1}. Block *et al.* also report ab initio calculations which found the global minimum in the potential energy surface to be at $\chi = 80°$ and a separation of 3.89 Å with a dissociation energy D_e of 174 cm^{-1}. The barrier height for rotation through the plane was calculated to be only 0.08 cm^{-1}.

Ab initio calculations were also reported for geometries in which the C_2H_4 monomer was rotated about the C-C double bond, with R held at 3.89 Å and $\theta = 90°$. These calculations overestimated the empirical 76 cm^{-1} barrier to rotation in this dimension considerably and were scaled to reproduce this barrier, so that calculation of the bending wavefunction in this coordinate could be undertaken. Calculations were also reported for the one-dimensional in-plane rotation, giving qualitative agreement with the shape of the Peet potential in this coordinate.

6.5 CONCLUSIONS

We have calculated energy levels and wavefunctions from a simple pairwise additive potential for Ar–C_2H_4. The results suggest that the molecule is free to rotate about the C-C double bond but is much more strongly hindered in the rotation in the plane of the molecule. Recent experimental results[184] suggest that our potential is not flat enough in the region about the global minimum, underestimates the equilibrium separation a little and that the barrier to rotation about the C-C double bond is too small by nearly a factor of two. Before additional effort is expended in trying to further rationalise the energy level pattern or the wavefunctions, it will be necessary to develop a potential that reproduces these basic features and reproduces the experimental spectrum.

Chapter 7: CONCLUSIONS AND FUTURE DIRECTIONS

This thesis has studied Van der Waals complexes for a series of three hydrocarbons, acetylene, methane and ethylene, interacting with argon. Both Ar–HCCH and Ar–CH$_4$ complexes have been found to be best described in terms of a hindered rotor model where the correlation between monomer and complex energy levels is clearly discernible. For Ar–C$_2$H$_4$ the complex is nearly free to rotate about the C–C bond but is much more strongly hindered in the in-plane rotation, making a free internal rotor assignment difficult.

For Ar–HCCH a more recent potential fit to new experimental data[41] has superseded the one developed in chapter 2 and little more progress in the study of this complex can be made until further experimental data becomes available.

For Ar–CH$_4$ three groups have measured the infrared spectrum,[85–87] but no assignment has been achieved. The theory for the energy levels of the complex with the monomer in the triply degenerate vibrational state has been laid out[88] and one direction for future work would be to attempt to predict spectra using various different potentials to try and aid assignment of the experimental data.

In Ar–C$_2$H$_4$ new spectroscopic data have recently been measured[184] and basic features of the potential, that are not reproduced by the model surface used here, are exposed. There is thus considerable scope for improving this potential. The Ar–hydrocarbon complex that would be of most interest to study next would be Ar–C$_2$H$_6$, to complete the series of Ar–C$_2$H$_n$ and hopefully draw some conclusions about the trends between the single, double and triple bonded complexes. It would also be interesting to study the influence of the Ar atom on the C$_2$H$_6$ internal rotation.

The other major achievement of this thesis is to provide a method of extracting wavefunctions from coupled channel calculations using the log-derivative propagator. The lack of wavefunctions from such methods has often been cited as one of their major shortcomings and the usefulness of such wavefunctions has been illustrated by providing new insights into both Ar–HF and He–CO$_2$ systems.

Chapter 8: REFERENCES

1   R. P. Feynman, "What do *you* care what other people think?", Unwin Hyman (1989).

2   D. J. Nesbitt, Chem. Rev. **88**, 843 (1988).

3   J. M. Hutson, Ann. Rev. Phys. Chem. **41**, 123 (1990).

4   Atom-Molecule Collision Theory, Ed. R. B. Bernstein, Plenum Press (1979).

5   Atomic and Molecular Beam Methods, Ed. G. Scoles, Oxford University Press (1988).

6   T. E. Gough, R. E. Miller and G. Scoles, J. Chem. Phys. **69**, 1588 (1978).

7   T. R. Dyke, B. J. Howard and W. Klemperer, J. Chem. Phys. **56**, 2442 (1972).

8   A. C. Legon, Ann. Rev. Phys. Chem. **34**, 275 (1983).

9   A. D. Buckingham, P. W. Fowler and J. M. Hutson, Chem. Rev. **88**, 963 (1988).

10 P. Hobza and R. Zahradnik, Chem. Rev. **88**, 871 (1988).

11 M. Rigby, E. B. Smith, W. A. Wakeham and G. C. Maitland, The Forces Between Molecules, Clarendon Press (1986).

12 R. Moszynski, B. Jeriorski, P. E. S. Wormer and A. van der Avoird, Chem. Phys. Lett. **221**, 161 (1994).

13 G. Chałasiński and M. M. Szczęśniak, Chem. Rev., in press.

14 D. J. Nesbitt, M. S. Child and D. C. Clary, J. Chem. Phys. **90**, 4855 (1989).

15 J. M. Hutson, Adv. Mol. Vibrat. Coll. Dyn. **1A**, 1 (1991).

16 J. M. Hutson in Dynamics of Polyatomic Van der Waals Molecules ed. N. Halberstadt and K. C. Janda, Plenum, New York (1990).

17 J. M. Hutson, J. Chem. Phys. **92**, 157 (1990).

18 A. E. Thornley and J. M. Hutson, J. Chem. Phys. **100**, 2505 (1994).

19 H. W. Kroto, Molecular Rotation Spectra, Wiley, (1975).

20 S. Green, J. Chem. Phys. **64**, 3463 (1976).

21 D. M. Brink and G. R. Satchler, *Angular Momentum*: 2nd ed., Clarendon Press, Oxford (1968).

22 S. Bratoz and M. L. Martin, J. Chem. Phys. **42**, 1051 (1965).

23 B. R. Johnson, J. Chem. Phys. **69**, 4678 (1978).

24 R. J. LeRoy and J. S. Carley, Adv. Chem. Phys. **42**, 353 (1980).

25 Z. Bačić and J. C. Light, Ann. Rev. Phys. Chem. **40**, 469 (1989).

26 W. Yang and A. C. Peet, Chem. Phys. Lett. **153**, 98 (1988).

27 J. M. Hutson, BOUND computer code, version 5, distributed by Collaborative Computational Project No. 6 of the UK Science and Engineering Research Council: 1993. The BOUND program is available by anonymous ftp from Internet address krypton.dur.ac.uk.

28 R. G. Gordon, J. Chem. Phys. **51**, 14 (1969).

29 A. M. Dunker and R. G. Gordon, J. Chem. Phys. **64**, 4984 (1976).

30 B. R. Johnson, J. Comp. Phys. **13**, 445 (1973).

31 D. E. Manolopoulos, J. Chem. Phys. **85**, 6425 (1986).

32 G. Danby, J. Phys. B **16**, 3393 (1983).

33 B. R. Johnson, J. Chem. Phys. **67**, 4086 (1977).

34 J. M. Hutson, Chem. Phys. Lett. **151**, 565 (1988).

35 R. L. DeLeon and J. S. Muenter, J. Chem. Phys. **72**, 6020 (1980).

36 Y. Ohshima, M. Iida and Y. Endo, Chem. Phys. Lett. **161**, 202 (1989).

37 T. A. Hu, D. G. Pritchard, L. S. Sun, J. S. Muenter and B. J. Howard, J. Mol. Spectrosc. **153**, 486 (1992).

38 M. Takami, Y. Ohshima, S. Yamamoto and Y. Matsumoto, Faraday Discuss. Chem. Soc. **86**, 1 (1988).

39 J. K. G. Watson in "Vibrational Spectra and Structure" (J. Durig, Ed.) Vol.6 pp 1-89 Elsevier, Amsterdam, 1977.

40 A. E. Thornley and J. M. Hutson, Chem. Phys. Lett. **198**, 1 (1992).

41 R. J. Bemish, P. A. Block, L. G. Pederson, W. Yang and R. E. Miller, J. Chem. Phys. **99**, 8585 (1993).

42 Y. Ohshima, Y. Matsumoto and M. Takami, J. Chem. Phys. **99**, 8385 (1993).

43 M. Yang and R. O. Watts, J. Chem. Phys. **100**, 3582 (1994).

44 R. G. A. Bone, J. Phys. Chem. **98**, 3126 (1994).

45 L. J. Danielson, K. M. McLeod and M. Keil, J. Chem. Phys. **87**, 239 (1987).

46 L. J. Danielson, M. Keil, and P. J. Dunlop, J. Chem. Phys. **88**, 4218 (1988).

47 T. Slee, R. J. Le Roy and C. E. Chuaqui, Mol. Phys. **666**, 66 (1992).

48 U. Buck, I. Ettischers, S. Schlemmer, M. Yang, P. Vohralik and R. O. Watts, J. Chem. Phys. **99**, 3494 (1993).

49 W. G. Read and W. H. Flygare, J. Chem. Phys. **76**, 2238 (1982).

50 A. C. Legon, P. P. Aldrich and W. H. Flygare, J. Chem. Phys. **75**, 625 (1981).

51 G. T. Fraser,K. R. Leopold and W. Klemperer, J. Chem. Phys. **80**, 1423 (1984).

52 N. W. Howard and A. C. Legon, J. Chem. Phys. **85**, 6898 (1986).

53 K. I. Peterson and W. Klemperer, J. Chem. Phys. **81**, 3842 (1984).

54 J. S. Muenter, J. Chem. Phys. **90**, 4048 (1989).

55 N. W. Howard and A. C. Legon, J. Chem. Phys. **88**, 6793 (1988).

Chapter 8: References

56   G. T. Fraser, R. D. Suenram, F. J. Lovas, A. S. Pine, J. T. Hougen, W. J. Lafferty and J. S. Muenter, J. Chem. Phys. **89**, 6028 (1988).

57   Y. Ohshima, Y. Matsumoto, M. Takami amd K. Kuchitsu, Chem. Phys. Lett. **147**, 1 (1988).

58   C. E. Dykstra, J. Am. Chem. Soc. **112**, 7540 (1990).

59   A. C. Peet, D. C. Clary and J. M. Hutson, J. Chem. Soc., Faraday Trans. II **83**, 1719 (1987).

60   J. M. Hutson, BOUND computer code, version 3 (1986), distributed by Collaborative Computational Project no 6. of the Science and Engineering Research Council (UK).

61   G. Herzberg, Molecular Spectra and Molecular Structure v2. Infrared and Raman Spectra of Polyatomic Molecules, Van Nostrand, 1945.

62   A. E. Ernesti and J. M. Hutson, Chem. Phys. Lett. **222**, 257 (1994).

63   J. T. Hougen, in International Review of Science, Physical Chemistry Series 2, Vol. 3: Spectroscopy, ed. D. A. Ramsay (Butterworth, London, 1976).

64   T. R. Phillips and D. Secrest. J. Chem. Phys. **92**, 3410 (1990).

65   U. Buck, K. H. Kohl, A. Kohlhase, M. Faubel and U. Staemeler, Mol. Phys. **55**, 1255 (1985).

66   T. Phillips and D. Secrest, J. Chem. Phys. **91**, 2840 (1989).

67   M. J. O'Loughlin, B. P. Reid and R. K. Sparks, J. Chem. Phys. **83**, 5647 (1985).

68   G. Liuti, E. Luzzatti, F. Pirani and G. G. Volpi, Chem. Phys. Lett. **135**, 387 (1987).

69   G. Liuti, F. Pirani, U. Buck and B. Schmidt, Chem. Phys. **126**, 11 (1988).

70   U. Buck, A. Kohlhase, D. Secrest, T. Phillips, G. Scoles and F. Grein, Mol. Phys. **55**, 1233 (1985).

71   A. Schiffman, W. B. Chapman, J. Nibler, D. J. Nesbitt and J. M. Hutson, J. Chem. Phys. **98**, 9513 (1993).

72   T. G. Heil and D. Secrest, J. Chem. Phys. **69**, 219 (1978).

73   L. N. Smith and D. Secrest, J. Chem. Phys. **74**, 3889 (1981).

74   U. Buck, J. Schleusener, D. J. Malik and D. Secrest, J. Chem. Phys. **74**, 1707 (1981).

75   U. Buck, A. Kohlhase, T. Phillips and D. Secrest, Chem. Phys. Lett. **98**, 199 (1983).

76   M. M. Szczęśniak, G. Chałasiński and S. M. Cybulski, J. Chem. Phys. **96**, 463 (1992).

77   Y. Ohshima and Y. Endo, J. Chem. Phys. **93**, 6256 (1990).

78   A. C. Legon and A. L. Wallwork, *J. Chem. Soc. Chem. Commun.* 588 (1989).

Chapter 8: References

79 A. C. Legon, B. P. Roberts and A. L. Wallwork, Chem. Phys. Lett. **173**, 107 (1990).

80 M.-C. Duval and B. Soep, Chem. Phys. Lett. **141**, 225 1987).

81 N. Fuke, T. Saito, S. Nonose and K. Kaya, J. Chem. Phys. **86**, 4745 (1987).

82 I. Wallace and W. H. Breckenridge, J. Chem. Phys. **97**, 2318 (1992).

83 A. Ramirez-Solis and S. Castillo, J. Chem. Phys. **98**, 8065 (1993).

84 L. Dore, R. C. Cohen, C. A. Schmuttenmaer, K. L. Busarow, M. J. Elrod, J. G. Loeser and R. J. Saykally, J. Chem. Phys. **100**, 863 (1994).

85 A. R. W. McKellar, Faraday Discuss. Chem. Soc. **97**, 000 (1994)

86 C. M. Lovejoy and D. J. Nesbitt, unpublished work.

87 P. A. Block and R. E. Miller, unpublished work.

88 R. W. Randall, J. B. Ibbotson and B. J. Howard, J. Chem. Phys. **100**, 7042 (1994).

89 R. W. Randall, J. B. Ibbotson and B. J. Howard, J. Chem. Phys. **100**, 7052 (1994).

90 L. N. Smith, D. J. Malik and D. Secrest, J. Chem. Phys. **71**, 4502 (1979).

91 P. R. Bunker, *Molecular Symmetry and Spectroscopy*, Academic Press, New York (1979).

92 G. Tarrago, M. Dang-Nhu, G. Poussigue, G. Guelachvili and C. Amiot, J. Mol. Spectrosc. **57**, 246 (1975).

93 T. Oka, J. Mol. Spectrosc. **48**, 503 (1973).

94 M. L. Polak, Ph.D Dissertation, University of California at Berkeley, (1990).

95 J. M. Hutson, BOUND computer code, version 4 (1991), distributed by Collaborative Computational Project no. 6 of the Science and Engineering Research Council (UK).

96 E. Zwart, H. Linnarz, W. L. Meerts, G. T. Fraser, D. D. Nelson and W. Klemperer, J. Chem. Phys. **95**, 793 (1991).

97 M. Johnston and D. M. Dennison, Phys. Rev. **48**, 868 (1935).

98 W. Gordy and R. L. Cook, *Molecular Microwave Spectra*, Wiley, New York (1970).

99 K. T. Hecht, J. Mol. Spectrosc. **5**, 355 (1960).

100 J. M. Brown and B. J. Howard, Mol. Phys. **31**, 1517 (1976).

101 A. G. Robiette, D. L. Gray and F. W. Birss, Mol. Phys. **32**, 1591 (1976).

102 Faraday Discuss. Chem. Soc. **000**, 97, (1994)

103 D. E. Manolopoulos, private communication.

104 J. M. Hutson, J. Chem. Phys. **96**, 6752 (1992).

105 F. Mrugała and D. Secrest, J. Chem. Phys. **78**, 5954 (1983).

106 F. Mrugała and D. Secrest, J. Chem. Phys. **79**, 5960 (1983).

Chapter 8: References

[107] D. E. Manolopoulos, M. J. Jamieson and A. D. Pradhan, J. Comp. Phys. **105**, 169 (1993).

[108] D. E. Manolopoulos, Ph. D. Thesis, Cambridge University (1988).

[109] W. H. Press, B. P. Flannery, S. A. Teukolsky and W. T. Vetterling, *Numerical Recipes*, 2nd ed., Cambridge University Press (1992).

[110] J. M. Hutson, Comp. Phys. Commun. **84**, 1 (1994).

[111] S. Green and J. M. Hutson, J. Chem. Phys. **100**, 891 (1994).

[112] C. M. Lovejoy, J. M. Hutson and D. J. Nesbitt, J. Chem. Phys. **97**, 8009 (1992).

[113] A. S. Pine, J. Chem. Phys. **101**, 3444 (1994).

[114] H.-C. Chang, F.-M. Tao, W. Klemperer, C. Healey and J. M. Hutson, J. Chem. Phys. **98**, 2497 (1993).

[115] G. Guelachvili, Opt. Commun. **19**, 150 (1976).

[116] E. S. Fishburne and K. N. Rao, J. Mol. Spectrosc. **19**, 290 (1966).

[117] D. C. Clary and D. J. Nesbitt, J. Chem. Phys. **90**, 7000 (1989).

[118] R. N. Zare, Angular Momentum, Wiley (1988).

[119] J. D. Poll and J. L. Hunt, Can. J. Phys. **54**, 461 (1976).

[120] A. D. Buckingham, Adv. Chem. Phys. **12**, 107 (1967).

[121] E. B. Wilson, J. C. Decius and P. C. Cross, *Molecular Vibrations*, McGraw-Hill, New York (1955).

[122] S-Y. Liu and C. E. Dykstra, J. Phys. Chem. **90**, 3097 (1986).

[123] E. -A. Reinsch and W. Meyer, Phys. Rev. A **14**, 915 (1976).

[124] C. M. Lovejoy and D. J. Nesbitt, J. Chem. Phys. **91**, 2790 (1989).

[125] M. Keil, G. A. Parker and A. Kupperman, Chem. Phys. Lett. **59**, 443 (1978).

[126] G. A. Parker, M. Keil and A. Kupperman, J. Chem. Phys. **78**, 1145 (1983).

[127] M. Keil and G. A. Parker, J. Chem. Phys. **82**, 1947 (1985).

[128] U. Buck, H. Meyer, M. Tolle and R. Schinke, Chem. Phys. **104**, 345 (1986).

[129] L. J. Danielson, K. M. McLeod and M. Keil, J. Chem. Phys. **87**, 239 (1987).

[130] C. T. Wickham-Jones, C. J. S. M. Simpson and D. C. Clary, Chem. Phys. **117**, 9 (1987).

[131] L. Beneventi, P. Casavecchia, F. Vecchiocattivi. G. G. Volpi, U. Buck , Ch. Lauenstein and R. Schinke, J. Chem. Phys. **89**, 4671 (1988).

[132] M. J. Weida, J. M. Sperhac, D. J. Nesbitt and J. M. Hutson, in press.

[133] R. T. Pack, J. Chem. Phys. **61**, 2091 (1974).

[134] G. A. Parker, R. L. Snow and R. T. Pack, J. Chem. Phys. **64**, 1668 (1978).

[135] C. L. Stroud and L. M. Raff, J. Chem. Phys. **72**, 5479 (1980).

[136] G. Jolicard, G. Durand and X. Chapuisat, J. Chem. Phys. **74**, 2206 (1981).

[137] P. M. Agrawal and L. M. Raff, J. Chem. Phys. **75**, 2163 (1981).

[138] D. C. Clary, J. Chem. Phys. **75**, 209 (1981).

Chapter 8: References

[139] D. C. Clary, Chem. Phys. **65**, 247 (1982).

[140] G. D. Billing and D. C. Clary, Chem. Phys. Lett. **90**, 27 (1982).

[141] M. H. Alexander and D. C. Clary, Chem. Phys. Lett. **98**, 319 (1983).

[142] D. C. Clary, J. Chem. Phys. **78**, 4915 (1983).

[143] G. D. Billing and D. C. Clary, Chem. Phys. **80**, 213 (1983).

[144] A. J. Banks and D. C. Clary, J. Chem. Phys. **86**, 802 (1987).

[145] F. A. Gianturco, J. P. Toennies, M. Bernardi and M. Venanzi, J. Chem. Phys. **93**, 1641 (1990).

[146] C. K. Wong, E. E. Hanson and F. R. W. McCourt, Mol. Phys. **74**, 497 (1991).

[147] M. Keil, L. J. Rawluk and T. W. Dingle, J. Chem. Phys. **96**, 6621 (1992).

[148] G. Rotzoll and A. Lübbert, J. Chem. Phys. **71**, 2275 (1979).

[149] A. P. Kalinin, V. N. Khromov and V. B. Leonas, Mol. Phys. **47**, 811 (1982).

[150] S. B. Ryali, J. B. Fenn, C. E. Kolb and J. A. Silver, J. Chem. Phys. **76**, 5878 (1982).

[151] U. Buck, F. Huisken, D. Otten and R. Schinke, Chem. Phys. Lett. **101**, 126 (1983).

[152] U. Buck, D. Otten, R. Schinke and D. Poppe, J. Chem. Phys. **82**, 202 (1985).

[153] P. M. Dehmer, J. Chem. Phys. **83**, 24 (1985).

[154] C. Dreyfus, L. Berreby and E. Dayan, Chem. Phys. Lett. **79**, 476 (1981).

[155] E. J. Bohac, M. D. Marshall and R. E. Miller, J. Chem. Phys. **97**, 4890 (1992).

[156] E. J. Bohac, M. D. Marshall and R. E. Miller, J. Chem. Phys. **97**, 4901 (1992).

[157] J. M. Steed, T. A. Dixon and W. Klemperer, J. Chem. Phys. **70**, 4095 (1979).

[158] S. W. Sharpe, R. Sheeks, C. Wittig and R. A. Beaudet, Chem. Phys. Lett. **151**, 267 (1988).

[159] G. T. Fraser, A. S. Pine and R. D. Suenram, J. Chem. Phys. **88**, 6157 (1988).

[160] S. W. Sharpe, D. Reifschneider, C. Wittig and R. A. Beaudet, J. Chem. Phys. **94**, 233 (1991).

[161] M. Iida, Y. Ohshima and Y. Endo, J. Phys. Chem. **97**, 357 (1993).

[162] G. D. Billing, Chem. Phys. **91**, 327 (1984).

[163] G. D. Billing, Chem. Phys. Lett. **117**, 145 (1985).

[164] P. M. Agrawal and N. C. Agrawal, Chem. Phys. Lett. **117**, 451 (1985).

[165] A. M. Hough and B. J. Howard, J. Chem. Soc., Faraday Trans. II **83**, 173 (1987).

[166] A. M. Hough and B. J. Howard, J. Chem. Soc., Faraday Trans. II **83**, 191 (1987).

[167] N. Dutartre and C. Dreyfus, Chem. Phys. **121**, 371 (1988).

[168] T. R. Horn, R. B. Gerber and M. A. Ratner, J. Phys. Chem. **97**, 3151 (1993).

[169] A. Borysow and M. Moraldi, J. Chem. Phys. **99**, 8424 (1993).

[170] J. M. Hutson, unpublished work.

[171] G. Guelachvili, J. Mol. Spectrosc. **79**, 72 (1980).

Chapter 8: References

[172] G. Herzberg, Molecular Spectra and Molecular Structure: 2. Infrared and Raman Spectra of Polyatomic Molecules, Van Nostrand (1945).

[173] J. M. Hutson, J. Phys. Chem. **96**, 4237 (1992).

[174] R. C. L. Yuan and G. W. Flynn, J. Chem. Phys. **58**, 649 (1973).

[175] M. P. Casassa, D. M. Bomse and K. C. Janda, J. Chem. Phys. **74**, 5044 (1981).

[176] W.-L. Liu, K. Kolenbrander and J. M. Lisy, Chem. Phys. Lett. **112**, 585 (1984).

[177] C. M. Western, M. P. Casassa and K. C. Janda, J. Chem. Phys. **80**, 4781 (1984).

[178] D. C. Clary, Mol. Phys. **51**, 1299 (1984).

[179] J. M. Hutson, D. C. Clary and J. A. Beswick, J. Chem. Phys. **81**, 4474 (1984).

[180] S. R. Hair, J. A. Beswick and K. C. Janda, J. Chem. Phys. **89**, 3970 (1988).

[181] L. J. Danielson, M. Keil and P. J. Dunlop, J. Chem. Phys. **88**, 4218 (1988).

[182] A. R. Tiller, A. C. Peet and D. C. Clary, J. Chem. Phys. **91**, 1079 (1989).

[183] A. R. Tiller and D. C. Clary, Chem. Phys. **139**, 67 (1989).

[184] P. A. Block, L. G. Pedersen and R. E. Miller, J. Chem. Phys. **98**, 3754 (1993).

[185] R. B. Foster, G. W. Hills and W. J. Jones, Mol. Phys. **33**, 1589 (1977).

Chapter 8: References

Appendix A: Conferences, Courses and Seminars Attended

The following information is included in compliance with the requirements of the Board of Studies in Chemistry.

Conferences and Courses Attended

1. Annual conference of the High Resolution Spectroscopy Group with The Spectroscopy Group of the Institute of Physics, 'Novel Spectroscopic Techniques for High Resolution Spectroscopy.' Heriot Watt University, 18-20 December 1991.

2. European Meeting on Photons, Beams and Chemical Dynamics. University of Paris XI at Orsay, 8-10 July 1992.

3. Annual conference of the High Resolution Spectroscopy Group of the Royal Society of Chemistry, Exeter College, Oxford, 20th-22nd December 1992.

4. M.B.D.G. Spring Meeting. University of Birmingham, 22nd April 1993.

5. 4th Annual Informal Northern Universities Chemical Physics Meeting, 15th July 1993.

6. CCP6 Workshop: Fitting Molecular Potential Energy Surfaces, University of Durham, 18th-21st July 1993.

7. European Workshop on Quantum Chemistry in Molecular design, University of Oxford, 14th-15th October 1993.

8. European Conference on Unstable Species, Centre de Physique, Les Houches, 17th-20th January 1994. Poster Presented:'Wavefunctions from the log-derivative method for solving the coupled equations.'

9. The Royal Society of Chemistry, Faraday Division, Discussion No:97 Strycture and Dynamics of Van der Waals Complexes, University of Durham, 6th-8th April 1994. Poster Presented:'Wavefunctions for Van der Waals Complexes'

The following pages contain lists of the seminars in the chemistry department from 1991-1994. Those marked with an asterisk were attended.

1991

October   17   Dr. J.A. Salthouse, University of Manchester
Son et Lumiere – a demonstration lecture

October   31   Dr. R. Keeley, Metropolitan Police Forensic Science
Modern forensic science

November   6   Prof. B.F.G. Johnson[†], Edinburgh University
Cluster–surface analogies

November   7   Dr. A.R. Butler, St. Andrews University
Traditional Chinese herbal drugs: a different way of treating disease

November   13   Prof. D. Gani[†], St. Andrews University
The chemistry of PLP–dependent enzymes

November   20   Dr. R. More O'Ferrall[†], University College, Dublin
Some acid–catalysed rearrangements in organic chemistry

November   28   Prof. I.M. Ward, IRC in Polymer Science, University of Leeds
The SCI lecture: the science and technology of orientated polymers

December   4   Prof. R. Grigg[†], Leeds University
Palladium–catalysed cyclisation and ion–capture processes

December   5   Prof. A.L. Smith, ex Unilever
Soap, detergents and black puddings

December   11   Dr. W.D. Cooper[†], Shell Research
Colloid science: theory and practice

1992

January   22   Dr. K.D.M. Harris[†], St. Andrews University
Understanding the properties of solid inclusion compounds

January   29   Dr. A. Holmes[†], Cambridge University
Cycloaddition reactions in the service of the synthesis of piperidine and indolizidine natural products

Appendix A: Conferences, Courses and Seminars Attended

January	30	Dr. M. Anderson, Sittingbourne Research Centre, Shell Research Recent Advances in the Safe and Selective Chemical Control of Insect Pests
February	12	Prof. D.E. Fenton[†], Sheffield University Polynuclear complexes of molecular clefts as models for copper biosites
✳ February	13	Dr. J. Saunders, Glaxo Group Research Limited Molecular Modelling in Drug Discovery
February	19	Prof. E.J. Thomas[†], Manchester University Applications of organostannanes to organic synthesis
February	20	Prof. E.Vogel, University of Cologne *The Musgrave Lecture* Porphyrins: Molecules of Interdisciplinary Interest
February	25	Prof. J.F. Nixon, University of Sussex *The Tilden Lecture* Phosphaalkynes: new building blocks in inorganic and organometallic chemistry
February	26	Prof. M.L. Hitchman[†], Strathclyde University Chemical vapour deposition
✳ March	5	Dr. N.C. Billingham, University of Sussex Degradable Plastics – Myth or Magic?
March	11	Dr. S.E. Thomas[†], Imperial College Recent advances in organoiron chemistry
✳ March	12	Dr. R.A. Hann, ICI Imagedata Electronic Photography – An Image of the Future
✳ March	18	Dr. H. Maskill[†], Newcastle University Concerted or stepwise fragmentation in a deamination–type reaction
April	7	Prof. D.M. Knight, Philosophy Department, University of Durham Interpreting experiments: the beginning of electrochemistry
May	13	Dr. J–C Gehret, Ciba Geigy, Basel Some aspects of industrial agrochemical research

[†] Invited specially for the postgraduate training programme.

Appendix A: Conferences, Courses and Seminars Attended

October 15	Dr M. Glazer & Dr. S. Tarling, Oxford University & Birbeck College, London It Pays to be British! - The Chemist's Role as an Expert Witness in Patent Litigation
October 20	Dr. H. E. Bryndza, Du Pont Central Research Synthesis, Reactions and Thermochemistry of Metal (Alkyl) Cyanide Complexes and Their Impact on Olefin Hydrocyanation Catalysis
✳ October 22	Prof. A. Davies, University College London *The Ingold-Albert Lecture* The Behaviour of Hydrogen as a Pseudometal
✳ October 28	Dr. J. K . Cockcroft, University of Durham Recent Developments in Powder Diffraction
October 29	Dr. J. Emsley, Imperial College, London The Shocking History of Phosphorus
November 4	Dr. T. P. Kee, University of Leeds Synthesis and Co-ordination Chemistry of Silylated Phosphites
✳ November 5	Dr. C. J. Ludman, University of Durham Explosions, A Demonstration Lecture
November 11	Prof. D. Robins†, Glasgow University Pyrrolizidine Alkaloids : Biological Activity, Biosynthesis and Benefits
November 12	Prof. M. R. Truter, University College, London Luck and Logic in Host - Guest Chemistry
✳ November 18	Dr. R. Nix†, Queen Mary College, London Characterisation of Heterogeneous Catalysts
November 25	Prof. Y. Vallee. University of Caen Reactive Thiocarbonyl Compounds
November 25	Prof. L. D. Quin†, University of Massachusetts, Amherst Fragmentation of Phosphorous Heterocycles as a Route to Phosphoryl Species with Uncommon Bonding
November 26	Dr. D. Humber, Glaxo, Greenford AIDS - The Development of a Novel Series of Inhibitors of HIV
December 2	Prof. A. F. Hegarty, University College, Dublin Highly Reactive Enols Stabilised by Steric Protection
December 2	Dr. R. A. Aitken†, University of St. Andrews The Versatile Cycloaddition Chemistry of $Bu_3P.CS_2$
December 3	Prof. P. Edwards, Birmingham University The SCI Lecture - What is Metal?
December 9	Dr. A. N. Burgess†, ICI Runcorn The Structure of Perfluorinated Ionomer Membranes

Appendix A: Conferences, Courses and Seminars Attended

January 20	Dr. D. C. Clary†, University of Cambridge Energy Flow in Chemical Reactions
January 21	Prof. L. Hall, Cambridge NMR - Window to the Human Body
January 27	Dr. W. Kerr, University of Strathclyde Development of the Pauson-Khand Annulation Reaction : Organocobalt Mediated Synthesis of Natural and Unnatural Products
January 28	Prof. J. Mann, University of Reading Murder, Magic and Medicine
February 3	Prof. S. M. Roberts, University of Exeter Enzymes in Organic Synthesis
February 10	Dr. D. Gillies†, University of Surrey NMR and Molecular Motion in Solution
February 11	Prof. S. Knox, Bristol University *The Tilden Lecture* Organic Chemistry at Polynuclear Metal Centres
February 17	Dr. R. W. Kemmittt†, University of Leicester Oxatrimethylenemethane Metal Complexes
February 18	Dr. I. Fraser, ICI Wilton Reactive Processing of Composite Materials
February 22	Prof. D. M. Grant, University of Utah Single Crystals, Molecular Structure, and Chemical-Shift Anisotropy
February 24	Prof. C. J. M. Stirling†, University of Sheffield Chemistry on the Flat-Reactivity of Ordered Systems
March 10	Dr. P. K. Baker, University College of North Wales, Bangor 'Chemistry of Highly Versatile 7-Coordinate Complexes'
March 11	Dr. R. A. Y. Jones, University of East Anglia The Chemistry of Wine Making
March 17	Dr. R. J. K. Taylor†, University of East Anglia Adventures in Natural Product Synthesis
March 24	Prof. I. O. Sutherland†, University of Liverpool Chromogenic Reagents for Cations
May 13	Prof. J. A. Pople, Carnegie-Mellon University, Pittsburgh, USA *The Boys-Rahman Lecture* Applications of Molecular Orbital Theory
May 21	Prof. L. Weber, University of Bielefeld Metallo-phospha Alkenes as Synthons in Organometallic Chemistry
June 1	Prof. J. P. Konopelski, University of California, Santa Cruz Synthetic Adventures with Enantiomerically Pure Acetals
June 2	Prof. F. Ciardelli, University of Pisa Chiral Discrimination in the Stereospecific Polymerisation of Alpha Olefins
June 7	Prof. R. S. Stein, University of Massachusetts Scattering Studies of Crystalline and Liquid Crystalline Polymers

Appendix A: Conferences, Courses and Seminars Attended

June 16	Prof. A. K. Covington, University of Newcastle Use of Ion Selective Electrodes as Detectors in Ion Chromatography
June 17	Prof. O. F. Nielsen, H. C. Ørsted Institute, University of Copenhagen Low-Frequency IR - and Raman Studies of Hydrogen Bonded Liquids

† Invited specially for the graduate training programme.

Appendix A: Conferences, Courses and Seminars Attended

<u>1993</u>

September 13   Prof. Dr. A.D. Schlüter, Freie Universität Berlin, Germany
Synthesis and Characterisation of Molecular Rods and Ribbons

September 13   Dr. K.J. Wynne, Office of Naval Research, Washington, USA
Polymer Surface Design for Minimal Adhesion

September 14   Prof. J.M. DeSimone, University of North Carolina, Chapel Hill, USA
Homogeneous and Heterogeneous Polymerisations in Environmentally Responsible
Carbon Dioxide

September 28   Prof. H. Ila, North Eastern Hill University, India
Synthetic Strategies for Cyclopentanoids via Oxoketene Dithioacetals

October 4   Prof. F.J. Feher[†], University of California, Irvine, USA
Bridging the Gap between Surfaces and Solution with Sessilquioxanes

October 14   Dr. P. Hubberstey, University of Nottingham
Alkali Metals: Alchemist's Nightmare, Biochemist's Puzzle and Technologist's
Dream

October 20   Dr. P. Quayle[†], University of Manchester
Aspects of Aqueous ROMP Chemistry

October 21   Prof. R. Adams[†], University of South Carolina, USA
Chemistry of Metal Carbonyl Cluster Complexes : Development of Cluster Based
Alkyne Hydrogenation Catalysts

October 27   Dr. R.A.L. Jones[†], Cavendish Laboratory, Cambridge
Perambulating Polymers

November 10   Prof. M.N.R. Ashfold[†], University of Bristol
High Resolution Photofragment Translational Spectroscopy : A New Way to
Watch Photodissociation

November 17   Dr. A. Parker[†], Rutherford Appleton Laboratory, Didcot
Applications of Time Resolved Resonance Raman Spectroscopy to Chemical and
Biochemical Problems

November 24   Dr. P.G. Bruce[†], University of St. Andrews
Structure and Properties of Inorganic Solids and Polymers

November 25   Dr. R.P. Wayne, University of Oxford
The Origin and Evolution of the Atmosphere

December 1   Prof. M.A. McKervey[†], Queen's University, Belfast
Synthesis and Applications of Chemically Modified Calixarenes

December 8   Prof. O. Meth-Cohn[†], University of Sunderland
Friedel's Folly Revisited - A Super Way to Fused Pyridines

December 16   Prof. R.F. Hudson, University of Kent
Close Encounters of the Second Kind

Appendix A: Conferences, Courses and Seminars Attended

1994

January 26	Prof. J. Evans[†], University of Southampton Shining Light on Catalysts
February 2	Dr. A. Masters[†], University of Manchester Modelling Water Without Using Pair Potentials
February 9	Prof. D. Young[†], University of Sussex Chemical and Biological Studies on the Coenzyme Tetrahydrofolic Acid
February 16	Prof. K.H. Theopold, University of Delaware, USA Paramagnetic Chromium Alkyls : Synthesis and Reactivity
February 23	Prof. P.M. Maitlis[†], University of Sheffield Across the Border : From Homogeneous to Heterogeneous Catalysis
March 2	Dr. C. Hunter[†], University of Sheffield Noncovalent Interactions between Aromatic Molecules
March 9	Prof. F. Wilkinson, Loughborough University of Technology Nanosecond and Picosecond Laser Flash Photolysis
March 10	Prof. S.V. Ley, University of Cambridge New Methods for Organic Synthesis
March 25	Dr. J. Dilworth, University of Essex Technetium and Rhenium Compounds with Applications as Imaging Agents
April 28	Prof. R. J. Gillespie, McMaster University, Canada The Molecular Structure of some Metal Fluorides and Oxofluorides: Apparent Exceptions to the VSEPR Model.
May 12	Prof. D. A. Humphreys, McMaster University, Canada Bringing Knowledge to Life

[†] Invited specially for the graduate training programme.

Appendix A: Conferences, Courses and Seminars Attended